Experimental Investigation of Light Transport in Turbid Media

Dissertation
zur
Erlangung der naturwissenschaftlichen Doktorwürde
(Dr. sc. nat.)

vorgelegt der
Mathematisch-naturwissenschaftlichen Fakultät
der
Universität Zürich
von
Mirco Ackermann
von
Riniken (AG)

Promotionskommission
Prof. Dr. Christof Aegerter
Prof. Dr. Georg Maret
Prof. Dr. Andreas Schilling

Zürich, 2018

Introduction

In this thesis, I am going to write about my experiments in the area of wavefront shaping with turbid media. During my time as a PHD student, I started by trying to measure the transmission matrix of 1 mm thick samples of compressed TiO_2 powder, and then changed my project to develop a faster method of measuring the transmission matrix of thinner samples after we found out that our thicker samples do not show any Anderson localization, the main reason we were interested in measuring their transmission matrix in the first place. Experimentally, what brings these two projects together is that they both deal with measuring the phases of light in setups with low photon counts per phase measurement, once because of the limited amount of photons making their way all the way through the sample, and in the other case because of the fast scanning method.

I will start the thesis by introducing the physics behind scattering, and describe how a spatial light modulator (SLM) works and how it can be used to focus behind turbid media, and be used to measure a media's transmission matrix. Then I'll introduce a faster new scanning method to focus behind turbid media that should be able to bring the focusing time orders of magnitude below the current state of the art. Then, I'll turn to the thick TiO_2 samples and describe the problems faced measuring the transmission matrix of these samples, and finally, describe how we analyzed the time of flight data that we believed to be from localizing samples, and how a change in the way we analyzed, together with new measurements, showed that our samples do not localize.

Turbid Media and Laser Speckles

A turbid media is a media in which the path of waves such as

light waves is disturbed by a collection of small particles. These particles need to interact with the wave, for example, by having a refractive index different from their surrounding. If the particles are small relative to the wavelength, the scattering can be described by Rayleigh scattering, and the field of the scattered wave can be described by a wave originating at a point source defined by the particle position. If, on the other hand, the particle size is similar to the wavelength, then the more complex theory of Mie scattering needs to be used.

In this thesis, we will not care about the exact mechanism of the scattering processes themselves because I will only consider the effects of scattering in bulk material on a more macroscopic scale. It will be sufficient to view the scattering process as a random walk of photons which, on average, get scattered every mean free path length l, and loose all information of the original direction after the transport mean free path $l^* = 1/(1-g)$ where $g = \langle\cos(\theta)\rangle$ and θ is the scattering angle of many scattering events.

To simulate the spread of photons inside a scattering media, we can treat the photons as particles undergoing a random walk with step size l^*. It is also possible to solve the diffusion equation

$$\partial\Phi/\partial t = D\nabla^2\Phi - \gamma\Phi \tag{1}$$

where Φ is the photon density, γ describes the loss due to absorption and $D = l^* c_n/3$[1]. For an infinit scattering media with a point source $\Phi(x, y, z, t{=}0) = \delta(x)\delta(y)\delta(z)$ solving the diffusion equation will result in a Gaussian distribution that grows over time[2] given by

$$\Phi(r, t) = (4\pi Dt)^{3/2} \exp(-\frac{r^2}{4Dt} - \frac{t}{\tau_a}).$$

Formula 1 can be solved independently for the x-, the y-, and the z-coordinate. For a slab, the solution for the infinite sample can be adjusted by subtracting the intensity contributed by the paths that in the slab leave the sample along the z-axis. With these adjustments, it is possible to obtain a equation $I(t)$ that gives the intensity emitted by a slab of scattering media at a time t after it has been illuminated by a pulse on the other side. This will be used in the chapter *A Postmortem of Anderson Localization of Light in 3D* to analyze time of flight data from samples which we believed to be localizing.

For an understanding of speckles, we only care about the spatial distribution of the photons emitted by the slab. For a slab, the light intensity emitted closely follows a Gaussian with a width proportional to the sample thickness[2]. To simulate the speckles, we can simulate the light emitted by the sample by assuming that we are dealing with photons of random phase whose averaged intensity distribution follows a Gaussian distribution.

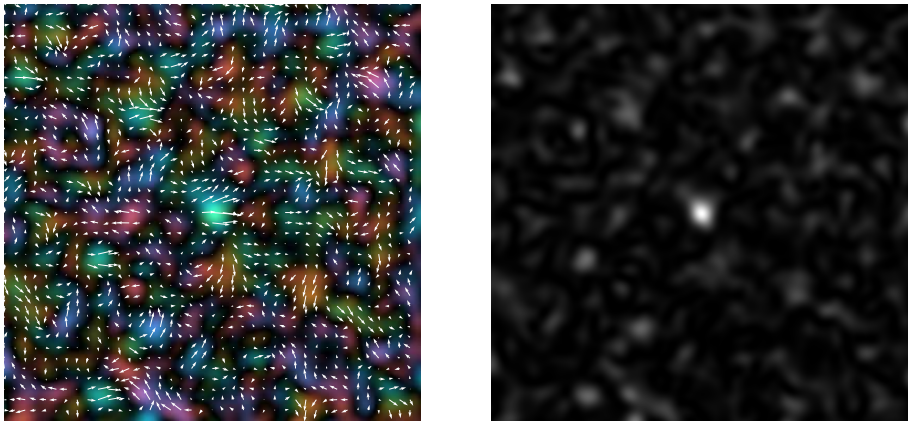

Figure 1: (left) Speckle amplitude. The brightness corresponds to the amplitude and the color corresponds to the phase, both also made visible through the vector field of white arrows. (right) The same speckles, but only the intensity is shown

With this simple model, we can create simulated speckles by creating a Gaussian intensity distribution with random phase and then calculate the far field of the sample in the Frauenhofer approximation by forming the Fourier transform. This gives the amplitude of our speckles. To get the intensity of the speckles, the absolute values of the far field needs to be squared. Later in this thesis, this method of speckle generation described above will be used to calculate an upper bound of the long term

```
def gaussian(x, mu, sig):
    return exp(-(x - mu)**2 / (2 * sig**2))

def speckle_amplitude(N, sig):
  # create normal distributed random numbers
  data = randn(N,N) + 1j*randn(N,N)
  # make their intensity spatially gaussian distributed
  y,x = meshgrid(linspace(-1,1,N), linspace(-1,1,N))
  data *= gaussian(abs(y+1j*x), 0, sig)
  # calculate frauenhofer diffraction
  return fft2(fftshift(data))
```

Listing 1: Code used to create a speckle pattern used in calculations and simulations

Focusing through Turbid Media

In the last section, I showed how when waves from a coherent source, such as from a laser, illuminate a turbid media, speckles appear behind the media. These speckles depend on the configuration of the scattering media. If the beam is moved to illuminate a different part of the sample, a completely different speckle pattern will appear.

To create a focus, lets start with a single beam illuminating a turbid sample. This will create a speckle pattern behind the sample. We can describe the phase and amplitude of our speckle pattern by phasors, arrows whose length is given by the amplitude and whose direction is given by the phase of the speckle pattern.
If we split the illuminating beam into two parts and illuminate only one half at a time, we get two new speckle patterns. Because we are in linear optics, the original speckle pattern can be calculated by summing the complex amplitudes of the two new speckle patterns. If we further split the illuminating beam into eight parts and look at the light at our target, we get phasors as shown by the black lines in figure 3.

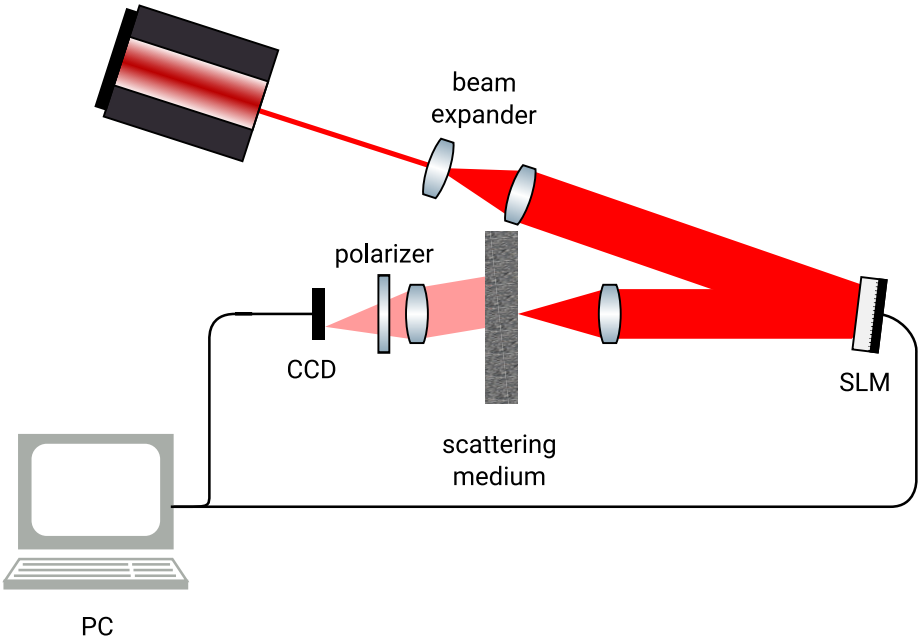

Figure 2: A simple setup to focus through a turbid medium. The light from a laser is expanded in a beam expander, which illuminates an SLM. The surface of the SLM is imaged onto the sample. After focusing, the phase of the light emerging from the sample is in phase. The phase of the light corresponds to a plane wave if a lens is placed in front of the CCD to measure the far field. If there was no lens between CCD and sample, the wave emerging from the sample after focusing would have the phase of a converging spherical wave.

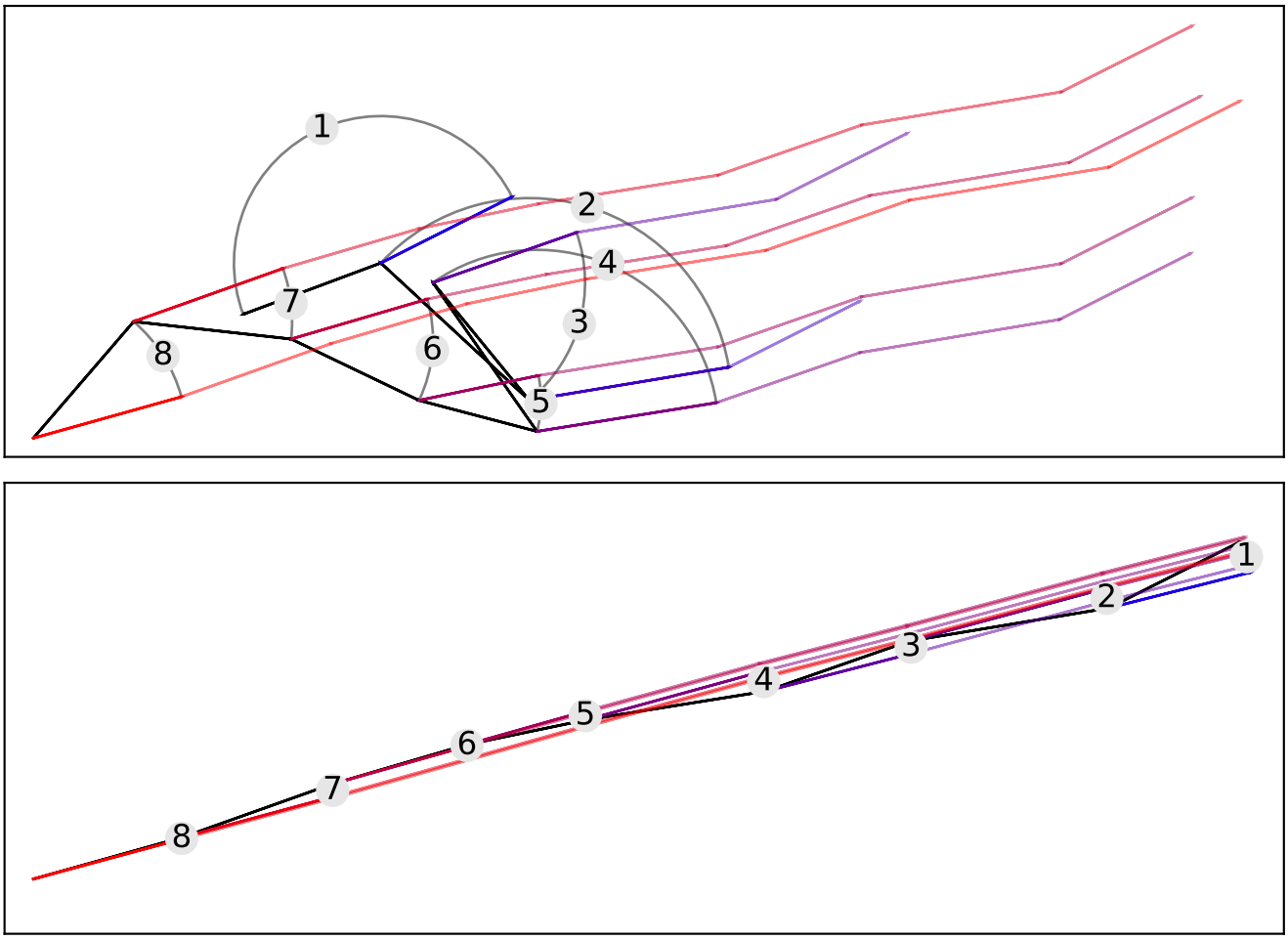

Figure 3: Phasors of light at the position of the focus as the intensity of the focus is optimized. The input beam is split into 8 parts. The phase of each of these (and through that also the phase of the phasor belonging to it) gets shifted, one after another, to maximize the summation of the phasors. This maximizes the intensity at the focus. The black lines correspond to the phasors of the unoptimized state, while the colored lines, from blue to red, show how the phasors change as the intensity increases during optimization.
At the top, the process is shown for light that has passed through a random media. At the bottom, the process is shown if it is applied to the optimized result from above. Notice that there is hardly any increase in intensity.

If we change the phase of one part of the illuminating beam by θ, using, for example, an SLM, then the phase of the corresponding speckle pattern will also change by θ. To create a focus, we can start by choosing a θ, so that at our desired point of focus, the complex amplitude of the speckle patterns created by the two parts of the beam, have the same angle. This will slightly increase the intensity at that position. If we split the incoming beam into more parts, and adjust the phase of each part individually, we can create a strong focus. In figure 3, such an optimization is shown for a beam split into eight parts.

Spatial Light Modulators (SLM)

A phase-only spatial light modulator (SLM) is a device containing many pixels arranged like those on a computer screen, each of which can create a phase shift between 0 and 2π. Using an SLM, it is possible to split a beam into many parts, and shift the phase of each part to optimize the intensity at some target as described in the last section. Additionally, by choosing a suitable pattern, optical elements such as lenses, prisms and gratings can be emulated. An SLM can also correct aberration and other defects in optical systems [3]. Focusing through a sample of scattering particles can be viewed as finding the necessary adjustments to the wavefront that will compensate the effects this particularly naughty optical element has. Finding a fast way to measure these necessary adjustments will be the main focus of this thesis.

There are two widely used methods to achieve spatial light modulation, those that use movable mirrors, and those that use liquid crystals. The SLM can either modulate the intensity (such as those commonly used in projectors) or the phase.

MEMS based SLM

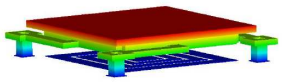

Figure 4: A single mirror of an MEMS-based SLM. The reflecting rectangular surface at the top can be moved vertically, which changes the optical path length of light reflected from this mirror, changing the phase of the reflected light by up to 2π [4].

An MEMS (Microelectromechanical systems) based SLM has many tiny adjustable mirrors (see figure 4 for a diagram of such a mirror). Each of these mirrors can create a phase shift of up to 2π by being moved up or down and thereby changing the length of the optical path of light being reflected [4, 5]. MEMS based SLM have the advantage that they can be driven at extremely high frame rates, with which it is possible to focus through living tissue[6].

Liquid Crystal based SLM

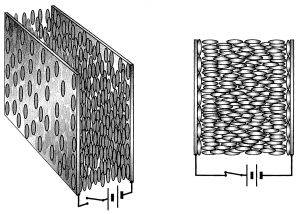

Figure 5: Nematic liquid crystal between two layers, without (left) and with a voltage applied (right) [7].

The second type of SLM is based on a liquid crystal layer which is either placed on top of a silicon wafer or on a glass surface, covered with a transparent layer (figure 5). In the liquid crystal on silicon (LCOS) configuration, the light is reflected on the silicon wafer, so it passes through the layer of the liquid crystal twice.

In equilibrium, molecules in the nematic liquid crystal will align parallel to the fine grooves set into the top and bottom surface.

Light traveling through this liquid crystal will have a higher index of refraction if it is polarized parallel rather than vertical to the molecules. By applying a voltage between the two surfaces, the molecules can be rotated away from the direction of the polarization as shown in figure 5, reducing the index of refraction, which changes the phase of light exiting the liquid crystal.

DMD based SLM

Another approach is to use a standard DMD (Digital Micromirror Device) chip, a type of MEMS that allows for binary amplitude modulation[9]. A DMD is made of lots of small mirrors that can be in one of two states, on or off. The mirrors in the on state reflect the light to further optics while those in the off state reflect the light onto a beam dump, allowing for binary intensity modulation of the wavefront. In a projector, this is expanded to display more intensity values by modulating the on-time of the mirrors, flashing them on and of at a high frequency.
While a projector trades temporal resolution to get multiple intensities, it is also possible to trade spatial resolution to modulate the phase of a wavefront. Conkey et al. suggest that the DMD chip is placed in an off-axis configuration and that pixels are grouped into macro pixels, each of which can be set to a selected phase shift through binary amplitude off-axis holography[8], giving a pattern as shown in figure 6.

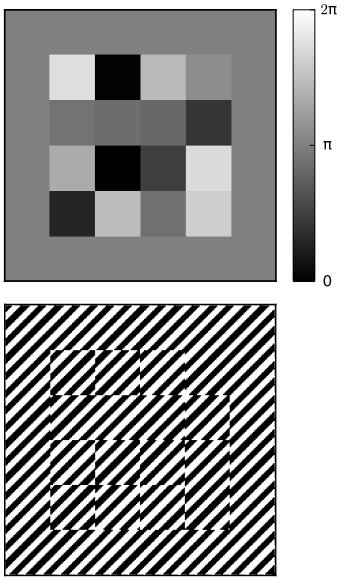

Figure 6: The phase shift (top) and the corresponding binary intensity pattern that creates this given phase shift through off-axis holography (bottom) [8].

In my experiment, I use such an SLM in an off-axis configuration that groups four pixels into a macro-pixel whose phase can be set in increments of $\pi/2$ to focus using only the SLM (see figure 14). This configuration was non-optimal because at 532 nm, the useful diffraction order for such a off-axis configuration was quite weak, so for the other measurements, I did not work in an off-axis configuration. Instead, I placed the SLM so that all pixels are in phase, a configuration that only allows the amplitude to be modulated.

Methods to Focus through Turbid Media

In this section, I'll give a quick overview of the methods used to focus through turbid media. A more detailed description will follow in chapter .

The easiest method to create a focus simply iterates over all pixels of the SLM, sets each to all possible phases, and chooses the one which gives the largest contribution at the target[10]. While simple to implement, this method has the disadvantage that in each step, only a small part of the SLM is modulated, which results in a rather weak signal. To get a better signal, it is possible to measure in the Hadamard base [11] or to use genetic algorithms[8]. Both of these methods modulate the phase of many pixels which results in a much stronger signal.

If you are interested in a transmission matrix, but do not care if it is in the canonical basis, then it is possible to measure in the k-basis using a tilting mirror[12]. If sufficient k-vectors are measured, it would be possible to Fourier transform the data from this method into the canonical basis and use the so gained information to focus using an SLM. But doing it like that has the disadvantage that while calculating the Fourier transform, an error in a single phase measurement for a k-vector spreads to all positions corresponding to the SLM-pixels. To prevent this effect, the method I'll propose uses optics to make each single pixel correspond to a k-vector, in effect doing the Fourier transform optically. This has the advantage that each pixel is set to the phase of a single measurement.

If the setup allows to send photons in the reverse direction, it is also possible to measure the phase of light arriving at the plane of the SLM and then setting the SLM to create a wavefront that is the conjugate of the measured wavefront. This method allows to focus within milliseconds since measuring the complex field of the wavefront can be measured by a CCD taking a single image, for example, by using ultrasound to create a guide star[13].

Faster Focusing Through Turbid Media

In the previous section, I described the experiment of Hyeonseung et al.[12] where they measured the transmission matrix by tilting a mirror and then recording the intensity of the speckle pattern on a CCD. The transmission matrix they measure contains an element for each combination of k-vector for the input light and output CCD pixel. If one were to Fourier transform this TM from the k-vector basis into the canonical basis, one could calculate the optimal wavefront, at the position of the tilting mirror, to focus on any spot of the CCD.

While calculating the Fourier transform after acquisition is possible, this method would have some disadvantages: For example, if a few of the measurements have a large error, or are simply just incorrect because the sample moved between the measurement time and the time when the information is used, then this error would propagate into the optimal phase calculated for all the SLM pixels. Also, aligning and selecting the k-vectors that correspond to the Fourier transform of the SLM pixels would be more difficult. To avoid these problems, I propose to bring the SLM pixels into k-space using a lens of focal length f placed a distance f from the SLM. This way, it is possible to do most of the alignment optically, and no Fourier transform needs to be calculated, and the phase information measured while scanning in k-space can be directly placed onto the SLM to create a focus. This also has the advantage that in principle, it would be possible to send the optimal phases to the SLM right after each scan-line, each of which takes $1/4000$ of a second to measure.

Measuring the Phase of Light

To measure the transmission matrix or to focus through turbid media, one needs to measure the phase of light that has passed through the media. There are many different approaches to do this which I'll describe in the next paragraphs.

One of the simplest approaches, experimentally, is to illuminate the sample with light from an SLM, to treat all areas of the SLM except for the area whose contribution one wants to find as a reference, and then take four measurements where the selected area of the SLM is set to a phase shift of $\alpha = 0$, $\pi/2$, π, and $3\pi/2$. The phase and amplitude contributed by the modulated area can be calculated as

$$A = \sum_{\alpha} \exp(i\alpha) I(\alpha). \tag{1}$$

With this method, the reference is created by the whole SLM minus the area for which the phase is measured. This means that for each area, a slightly different reference is used. In practice, this does not cause any problems because in each measurement, only a small part of the SLM gets off of reference duty. As shown in figure 3, the phases align already in the first pass, and there is hardly any change in phase or intensity in subsequent optimization passes.

This method is very easy to implement, with the simplest setups consisting of a beam expander illuminating directly an SLM which is imaged onto a sample using a simple lens. A CCD is then placed behind the sample at a distance where the size of the speckles created by the scattering sample are larger than a CCD pixel.

In such a four phase measurement, the intensity at our target pixel can be described by calculating the interference of the light coming from the reference pixels of the SLM having a complex amplitude of A_{ref} and by the light coming from the currently modulated pixels A_{mod}. This gives a measured intensity of

$$\begin{aligned} I(\alpha) &= |A_{\text{ref}} + \exp(i\alpha) A_{\text{mod}}|^2 \\ &= |A_{\text{ref}}|^2 + |A_{\text{mod}}|^2 + |A_{\text{ref}} A_{\text{mod}}| \cdot \cos(\alpha + \theta) \end{aligned} \tag{2}$$

where $\theta = \angle A$. When measuring the phase, it is only the cosine term of this equation that will contribute to the measured value, while the other two terms contribute a constant offset of the measured value.

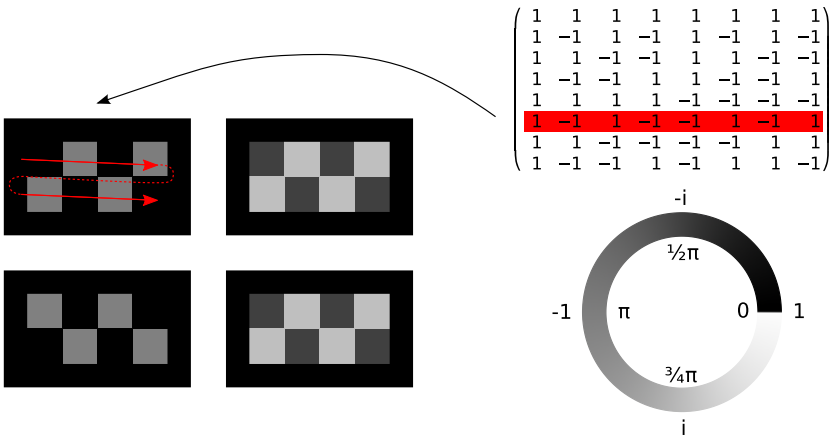

Figure 7: Segments of the SLM are set to values corresponding to the entries in a line of a Hadamard matrix. Values of 1 correspond to a phase shift of 0 while values of -1 correspond to a phase shift of π. The segments are then modulated as a group to create four measurements. Afterwards, this process is repeated for the other lines of the hadamard matrix.

There are many methods that improve on the just described method by modulating a large area of the SLM. A rather simple one modulates half the pixels of the SLM, using the Hadamard basis. This gives a much stronger signal relative to the offset, since I_{ref} and I_{mod} are of similar magnitude. But for simply focusing through turbid media, the Hadamard method has the disadvantage that the acquired intensity data needs to be Hadamard-transformed back into real space. When there are measurement errors or noise, the Hadamard-transform will spread these artifacts to the phase calculated for all pixels.

Besides the methods described, there are also methods that use a reference arm that illuminates the sensor such as a CCD with light that bypasses the sample. These have the advantage that the reference is not some arbitrary static speckle pattern, but a plane wave instead.

When using a reference arm, a plane wave created by light that bypassed the sample is used as a reference. If the reference wave is slightly off axis, the interference between the speckles and the plane wave will produce holographic fringes. From these (given that a camera with sufficient resolution is used) the phase of the speckles can be calculated, allowing single shot phase measurements, replacing the time-consuming four-phase measurement method described earlier.

If a light source is placed at a position where a focus is desired, it is possible to focus using a single-shot measurement. For this, a CCD is placed so that it is in a mirror plane of the SLM, illumi-

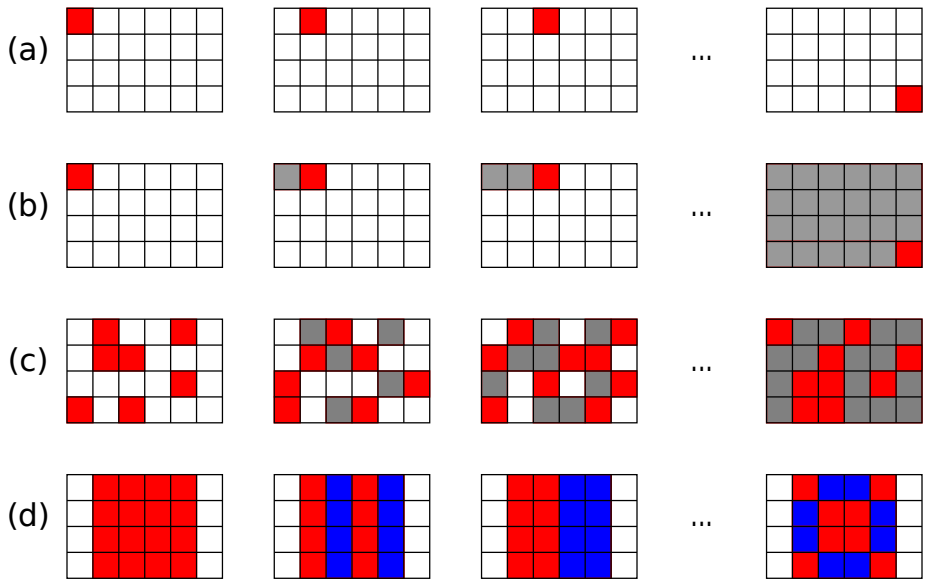

Figure 8: Methods to measure the optimal phase for a focus. (a) Measuring the optimal phase by measuring the phase contribution segment by segment. (b) Same as (a), but right after a segment's contribution has been measured (red), they are set to the their optimal phase (grey). (c) Another possibility is to randomly select segments, find the optimal phase change for these segments as a group (red) and then set them to that phase (gray). (d) Measure in the Hadamard basis. Here, a group of N segments is set by taking a line of a NxN Hadamard matrix and setting the segments to either a 0 (red) or π (blue) phase shift. Then, the intensity is measured when shifting all the colored segments by 0, $\pi/2$, π and $3\pi/2$ to get the phase contribution of the current pattern. This is repeated for all the lines of the Hadamard matrix, giving the complex amplitude of the individual Hadamard patterns. To get the phase information for the individual segments, the data acquired has to be transformed from the Hadamard basis back into the canonical basis by multiplying by the Hadamard matrix used in the measurement.

nated by the speckles from the sample which interfere with a plane wave from a reference arm. With the data from the CCD, it is now possible through holography to calculate the phase of the speckles imaged onto the CCD. If the SLM is set to the conjugate of these phases, then, when illuminated by the speckles from the sample, a plane wave will emerge from the SLM. The experiment can now be done in reverse, by illuminating the SLM by a plane wave. Because of time reversal, this will result in a focus at the position of the point source used for the single-shot measurement[14].

The methods just described all have some disadvantages: The method that sequentially measures the phase contribution of a small area of the SLM has a poor signal to noise ratio. The method measuring in the Hadamard basis has the disadvantage that errors from one measurement will spread into all of the deduced phases. Finally, all methods measuring the phase by modulating an SLM are limited by its refresh rate.

The new method I am proposing is based on the sequential method first described in this section, in that it measures the phase contribution of one area of the SLM after another. But instead of modulating a small part of the SLM, it uses a second beam whose phase is modulated. This second beam has a much stronger intensity than the corresponding area of the SLM, so that the intensity of A_{ref} is much closer to the intensity of A_{mod}, which gives a much better signal to noise ratio because the cosine term in equation (2) is much larger compared to the other non-phase dependent terms. Also, instead of using the SLM to measure the intensity at four different modulated phases, the method uses an AOTF (increaseing the frequency of the reference beam by 100MHz) which creates a reference beam whose phase offset continuously goes from 0 to 2π every 10ns. With a sufficiently high photon density, this would allow to measure the phase of an area of the SLM in 10ns. By moving the reference beam so that it scans the surface of the sample at positions corresponding to different areas of the SLM, it is possible to get the phase contribution (and therefore the optimal phase to get a focus) for all areas of the SLM. In the next section I'll explain the optical setup necessary to focus using this new method.

Experimental Setup

For the scanning beam, I use a wide beam from a beam expander and two tiltable mirrors, one a galvo mirror and the other a resonant mirror, which bring the center of the beam onto a 5mm pinhole. By tilting the mirrors, it is possible to scan the k-vector of the wavefront passing through the pinhole in a 2D space.

Because the pinhole is behind the mirrors, there is a small offset of the area of the beam that passes through the pinhole as the scanning process proceeds. To prevent an intensity fluctuation and to ensure an even illumination of the pinhole as the beam scans the k-space, the beam is expanded and only the center of the beam with quasi-uniform intensity is used.

The aim of the method is to scan using one beam, and then use the information gained to set the phase of a second beam with which it is then possible to focus through a scattering media. Lets call the wavefront of the scanning beam of a specific k-vector Φ_k. The wavefront we now want to create with the SLM is given by

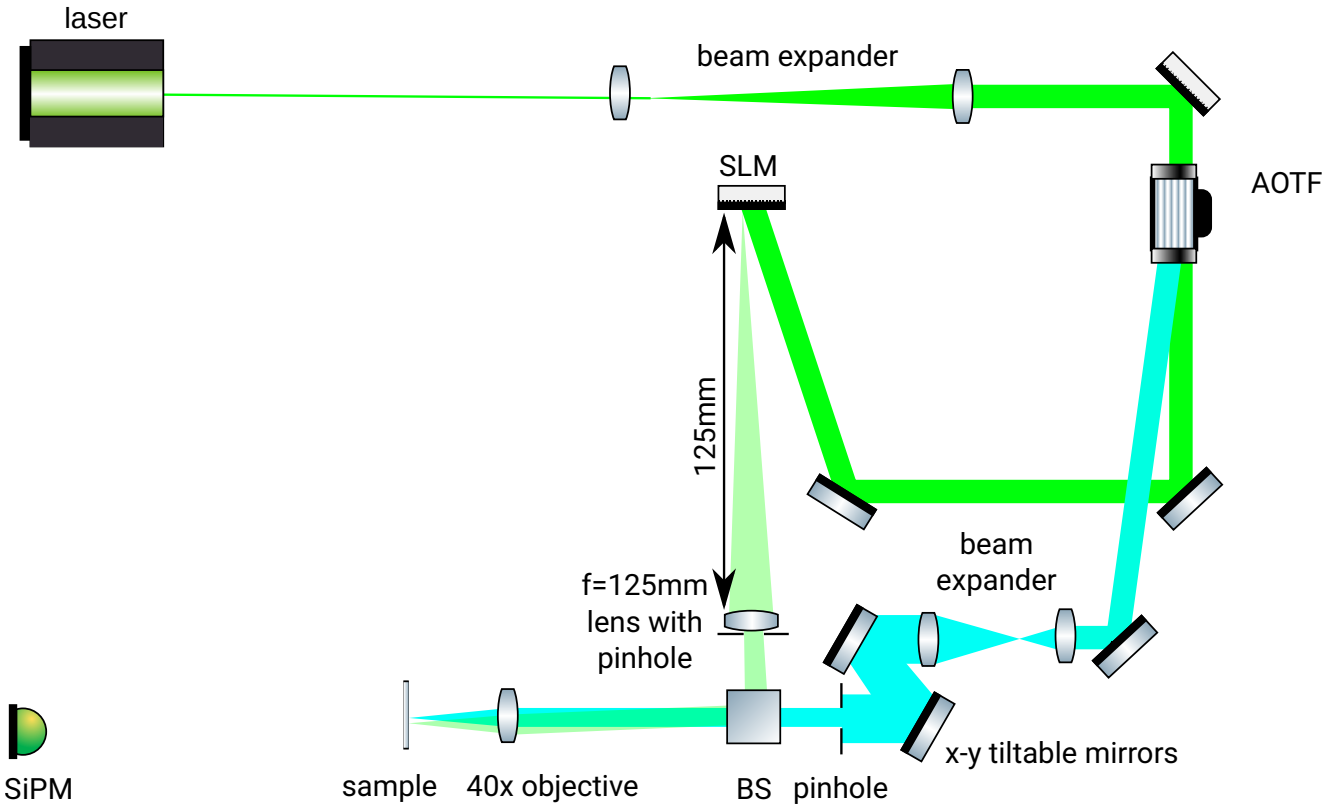

Figure 9: The scanning setup to focus through turbid media. The beam from a 532 nm laser passes through a beam expander, followed by a acousto-optic modulator (AOM). In the AOM, part of the beam gets diffracted on a 100MHz acoustic wave. This diffracted part has a frequency shifted by 100MHz, exaggerated in the image by the change of the hue. One part passes through another beam expander, followed by a x-y scanning mirror assembly, changing the k-vector of the beam. Of this beam, only the center with almost constant intensity is selected by a 5 mm pinhole. The other part of the beam coming from the AOM illuminates an SLM. In the image, light reflected from a single pixel of the SLM is shown. It is collimated by a lens and the edges are cut of as in the other beam. The pinholes are placed to be in mirror images of each other relative to the reflecting surface of the beam splitter that merges the light passing through them. After the beam splitter, a objective images the SLM onto the back of the sample, which is the same state as when the light from the other branch is imaged to its smallest spot. Behind the sample, an SiPM collects the light.

$\int_k \Phi_k \theta_k$ where θ_k is the optimal phase measured for a given k-vector with its position of the tiltable mirrors.

In the setup, this second light path joins the scanning light path in a beam splitter. The second light path has a pinhole which, with the beam splitter, creates a mirror image of the scanning light path. Right behind this pinhole is a $f = 100$mm lens collimating light coming from pixels of an SLM that is at its focal length from the lens. After the lens, the wavefront $\Phi_{x,y}$ created by a single pixel of the SLM is close to a plane wave, and there is a relation between its

k vector and the pixel position x, y. With this setup, all that needs to be done to get a focus is to set the SLM pixels x, y to the phase calculated for the corresponding k vector of the scanning beam.

Parallel Beams

In the experiment, there are many places where a parallel beam is required. To ensure a beam is parallel, I checked if the fringes created by a lateral shearing interferometer (Thorlabs SI050) were horizontal. [1]

[1] For a description on how to use a shearing interferometer and the math behind it, see, for example, [15].

Detecting the Signal

To measure the phase required to get a focus behind the turbid media, my setup uses the interference of the reference and the focusing light path. Between these light paths, there is a frequency difference of about 100MHz. This, after joining them through a beam splitter, causes a beating in the intensity of again 100MHz. When creating a focus, the phase of the beating pattern corresponds to the phase that should be loaded onto the pixel of the SLM corresponding to the position of the scanning beam. Measuring this phase presents a bit of a challenge.

I started my setup using an amplified photodiode [2]. This worked as long as it was placed directly in the beam, but there was insufficient signal when measuring behind the scattering media. Next, I considered using a photomultiplier, hoping to make use of its higher sensitivity and faster response, but it did not work out because after each detected photon, there is a dead time of at least 1 ns [16] for the internal capacitors to recharge – during this dead time, the photomultiplier is inactive. For a 100MHz modulated signal, this would mean that at most 10 photons could be measured within a cycle, which would be insufficient events to deduce the phase of the signal from.

[2] Thorlabs PDA015A amplified photodetector

Currently, I am using a silicon photomultiplier (SiPM)[3]. An SiPM is built up of avalanche photodiodes. These are diodes, operated with a large reverse bias of about 29V. This creates a strong electric gradient within the diode which, when an electron-hole pair is created, causes these pairs to gain so much kinetic energy that they can create new electron-hole pairs through collisions. The electrons

[3] The setup contains a SensL J-Series 30035 driven at 5-6V overvoltage. The numbers given in the following paragraphs are based on its data sheet [17].

and holes then create an avalanche of new electrons and holes, quite similar to how electrons are amplified in a photomultiplier.

The avalanche diode, just like a photomultiplier, has a capacitor that needs to be recharged after an avalanche. Just as in a photomultiplier, this creates a dead time, which in the SiPM used in the experiment is of the order of 45ns. This is a lot longer than the 1 ns available in a good photomultiplier, but this is not a problem: An SiPM chip contains lots of avalanche photodiodes in parallel. Each has a dead time of about 45 ns, but, for randomly distributed photons, the chance of hitting the same photodiode twice within the dead time is small. This allows the SiPM to have high sensitivity single-photon detection like a photomultiplier while at the same time producing useful data at high photon densities.

Of course, SiPMs have some disadvantages: While the quantum efficiency of photomultiplier tubes and the individual avalanche photo diodes in an SiPM are similar, in SiPM, the dark counts are much higher. In the SensL J 3 mm SiPM I use, the dark count is given as 150kHz. For our measurement, this is no problem, since the signal required to reliably detect the phase is much higher than this 150kHz dark count. There is also a chance of cross talk. SiPMs are made of many individual photodiodes. If one fires, there is a chance that a neighboring photodiode will also fire. For the used SiPM, the crosstalk rate is between 8% and 25%.

The quantum efficiency of an SiPM is similar to a traditional photomultiplier. It peaks at 50% at 425 nm, and goes down to about 30% at 532 nm. But unlike in a photomultiplier tube, in an SiPM, the quantum efficiency does not tell the whole truth. The stated efficiency is the chance of a pulse to be formed if the active area of the SiPM is hit by a photon. SiPM detector chips are made up of individual photo diodes separated by gaps. To get the total efficiency of a chip, the quantum efficiency (30%) has to be multiplied by the fill factor (75%) which for our chip gives a total efficiency of 22%.

At high photon counts, SiPMs perform quite well at phase detection. While at low photon intensities, the photon current is proportional to the number of detected photons, as the photon count increases, at some point, there is a non-negligible chance that the time between two consecutive photons arriving at a given pixel will be lower than the dead-time of the sensor. So at high photon intensities, the signal will no longer be proportional to the signal in photon density, but this is the range where the signal is sufficiently

strong anyway.

Alignment to Measure a Beating Pattern

The simplest experiment to measure the beating pattern of the two 100 Mhz shifted beams consists of the AOTF splitting the beam into two parts, followed by some mirrors which bring the beam onto a beam splitter through which the two beams are joined and left to interfere. When measuring the beating pattern, it is very important that the two beams are as close to parallel to each other as possible, because otherwise, if the two beams are slightly off, on the sensor, there will be a pattern of areas of constructive and destructive areas. Some of these areas will cancel each other out, leaving a very weak signal.

Phase Detection

In the experiment, the phase of the signal relative to the reference needs to be determined using IQ demodulation. The IQ demodulation can be done by the CPU after the signal is measured by an ADC converter, or it can be done using analogue electronics placed before the ADC converter. In the first case, the ADC measures the full waveform of the reference and of the beating pattern, in the second case, the ADC measures the real and imaginary part of the IQ-demodulated signal.

In both cases, the signal gets multiplied with the reference signal (both signals filtered with a 100MHz bandpass filter). This multiplication is done for the reference signal without time shift, and once again for the reference signal shifted by $\pi/2$. The two multiplied signals are then further filtered with a 1 Mhz low-pass filter, resulting in two signals corresponding to the complex and imaginary part of the complex phase measured by the scanning beam. The whole filtering operation can be described by the following equation:

$$\phi_t = \angle \mathrm{LOWPASS}_{1\mathrm{MHz}} \left(I_t \cdot \left(R_t + iR_{t+\frac{1}{4f}} \right) \right)$$

where $\angle$ is the angle of its complex argument, $\mathrm{LOWPASS}_{1\mathrm{MHz}}$ is a low-pass filter that filters away everything above 1MHz, R is the reference signal and I is the signal.

For both the software and the electronic method, a USB oscilloscope is used to acquire and transfer the data to the computer. The electronic method is much faster because it can work at a much lower sample rate (two channels of 10 Ms/s instead of two channels of 500Ms/s), allowing the data to be transmitted in real-time and then processed further without the time consuming filtering and demodulating step.

Repeatability of the Measurements

To use the phase information of a measurement made using the scanning beam to create a focus, it is important that the phase measurement is repeatable over time. I repeated the scanning process multiple times and compared the data, by plotting the phase of certain scan lines, and by creating images from the phase and intensity data. In the images, it is clear that there is some similarity between measurements, but it is unclear by how far the phase deviates. But with the line scans through the images, it quickly becomes apparent that the phase deviation is below a sixth of a wavelength, sufficient accuracy to create a focus. The measurements are shown in figure 11 to figure 12.

In addition to the repeatability of the scanning measurement, another important point is the stability of the setups SLM arm. In figure 14 a measurement of the optimal wavefront measured by the SLM is shown. A focus created by such a measurement is stable over many hours. Also, from the similarity of neighboring pixels in that image, it becomes clear that the measurements are repeatable, since as expected, neighboring pixels have similar phase and intensity contribution to the desired focus.

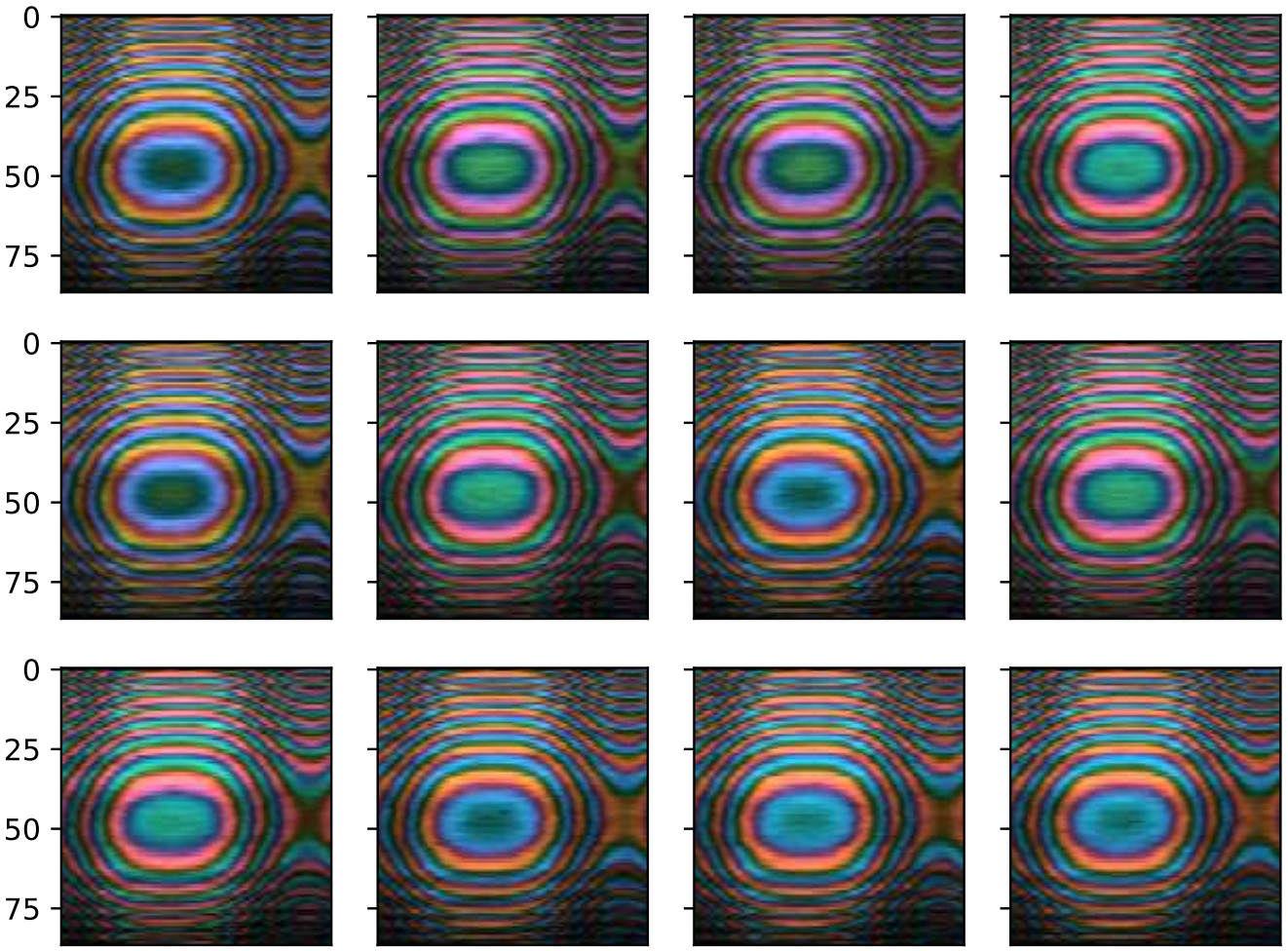

Figure 10: The intensity and phase acquired by scanning using the moving mirrors, without a sample. The rings are caused by the objective. The horizontal direction corresponds to the resonant x-mirror and the vertical direction corresponds to the galvo mirror. The angle of the resonant mirror follows a sinusoidal trajectory. This causes a distortion where the resonant mirror is at its extremes. The phase of a slice along the x-axis and along the y-axis is displayed in figure 11. The colorbar for this and the following images is shown to the right.

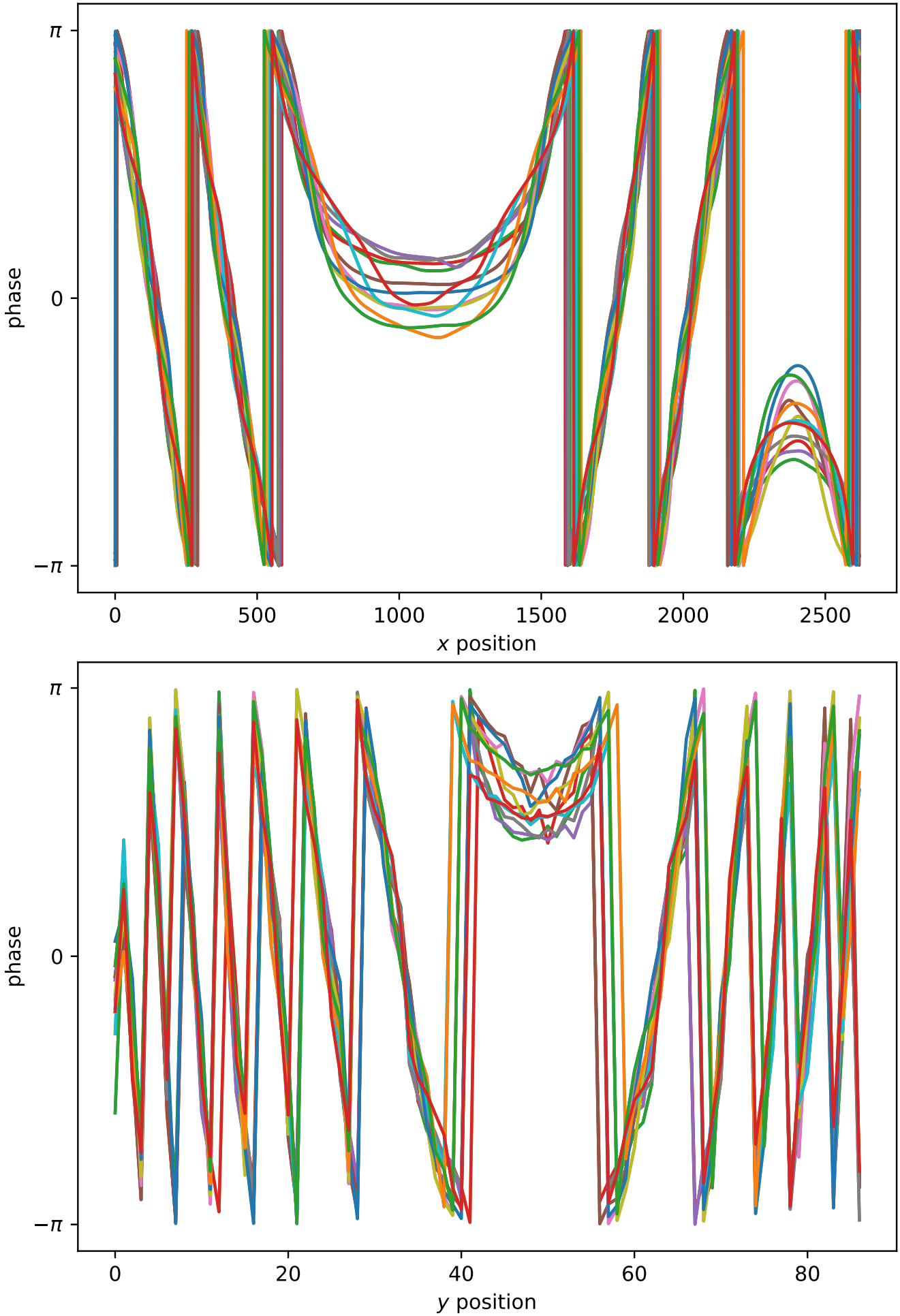

Figure 11: The phase of a slice along the x-axis (top) and y-axis (bottom) of the image shown in figure 11

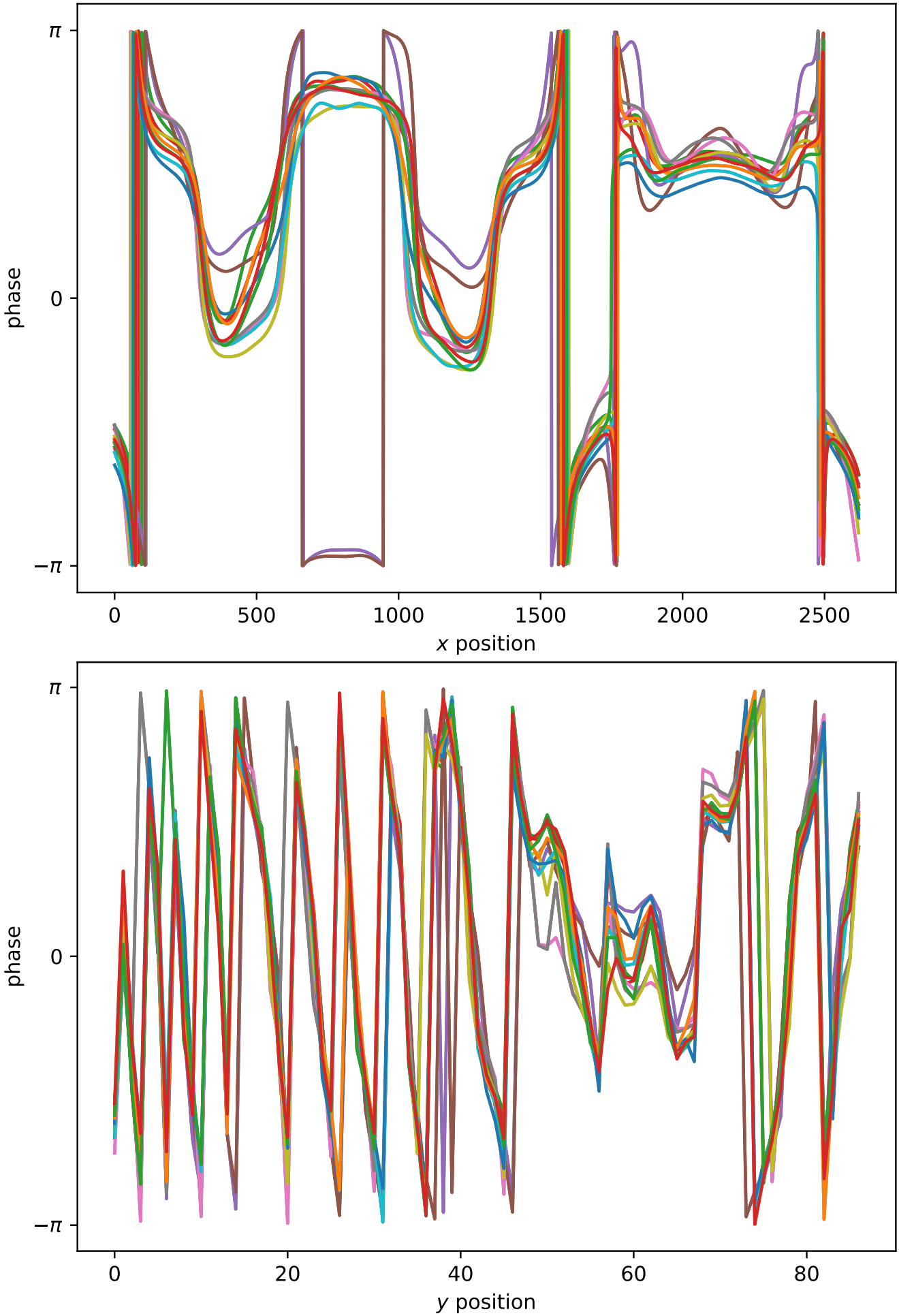

Figure 12: The phase of a slice along x-axis (top) and y-axis (bottom) of the image shown in figure 13

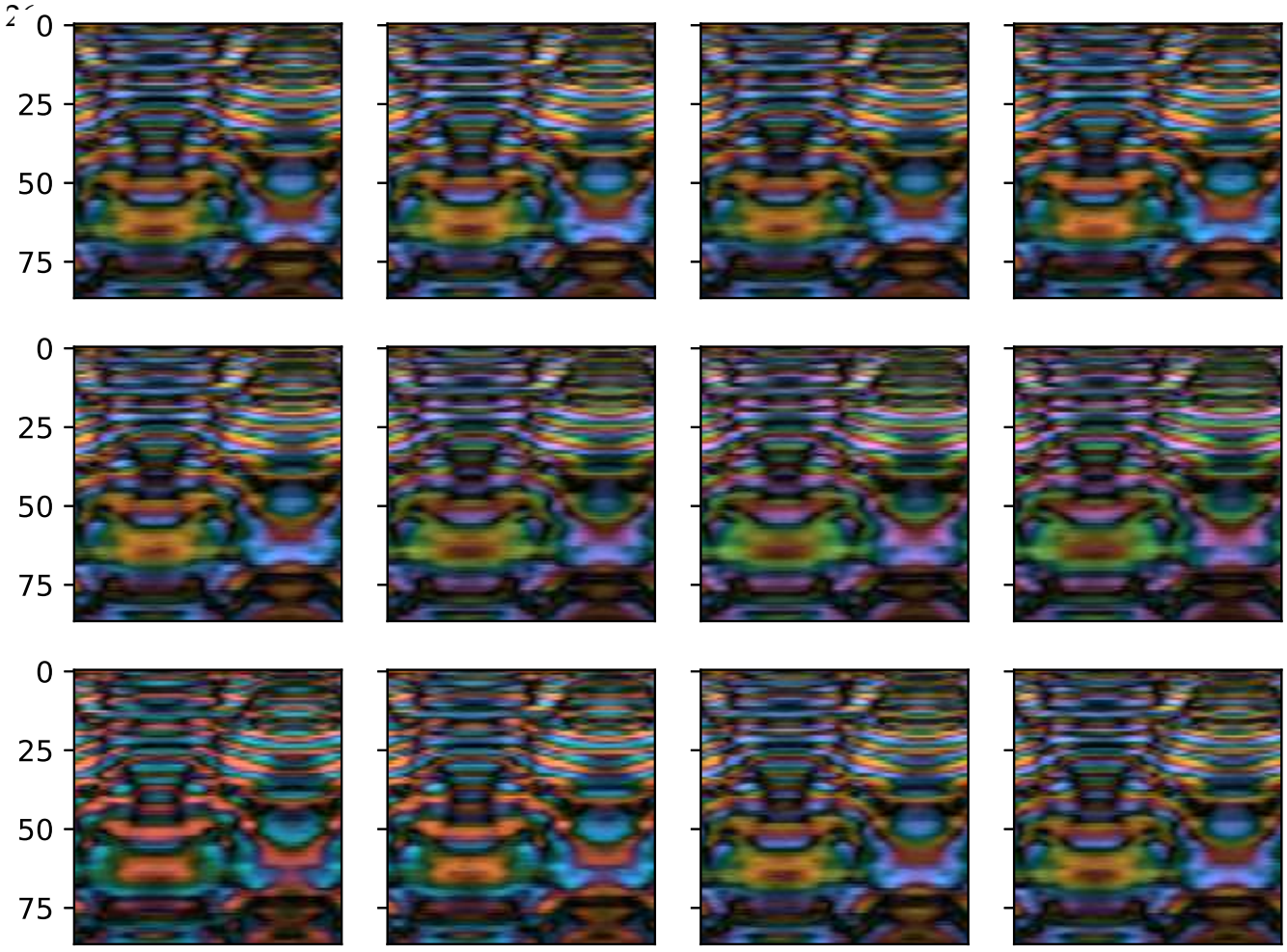

Figure 13: Same image as in figure 11, but measured with a diffuser. See figure 12 for the phase along lines parallel to the x- and y-axis

Plane of Focus

When aligned, there should be a focus of the scanning beam in the same plane as contains the image of the SLM. Theoretically, this should be the case when the two pinholes are illuminated by parallel beams, one by the scanning beam and the other by the collimated light from a single pixel of the SLM. The difficulty lies in ensuring that these two beams actually are parallel. For the scanning beam, a shearing interferometer was used. For the beam from the SLM, if only a single pixel is set into the on-state, there is insufficient light to use the shearing interferometer. Instead, we tried other approaches to set the distance between the collimating lens and the SLM:

My first approach was to focus the scanning beam onto a sample, a simple diffuser, by checking the speckle size which is maximal

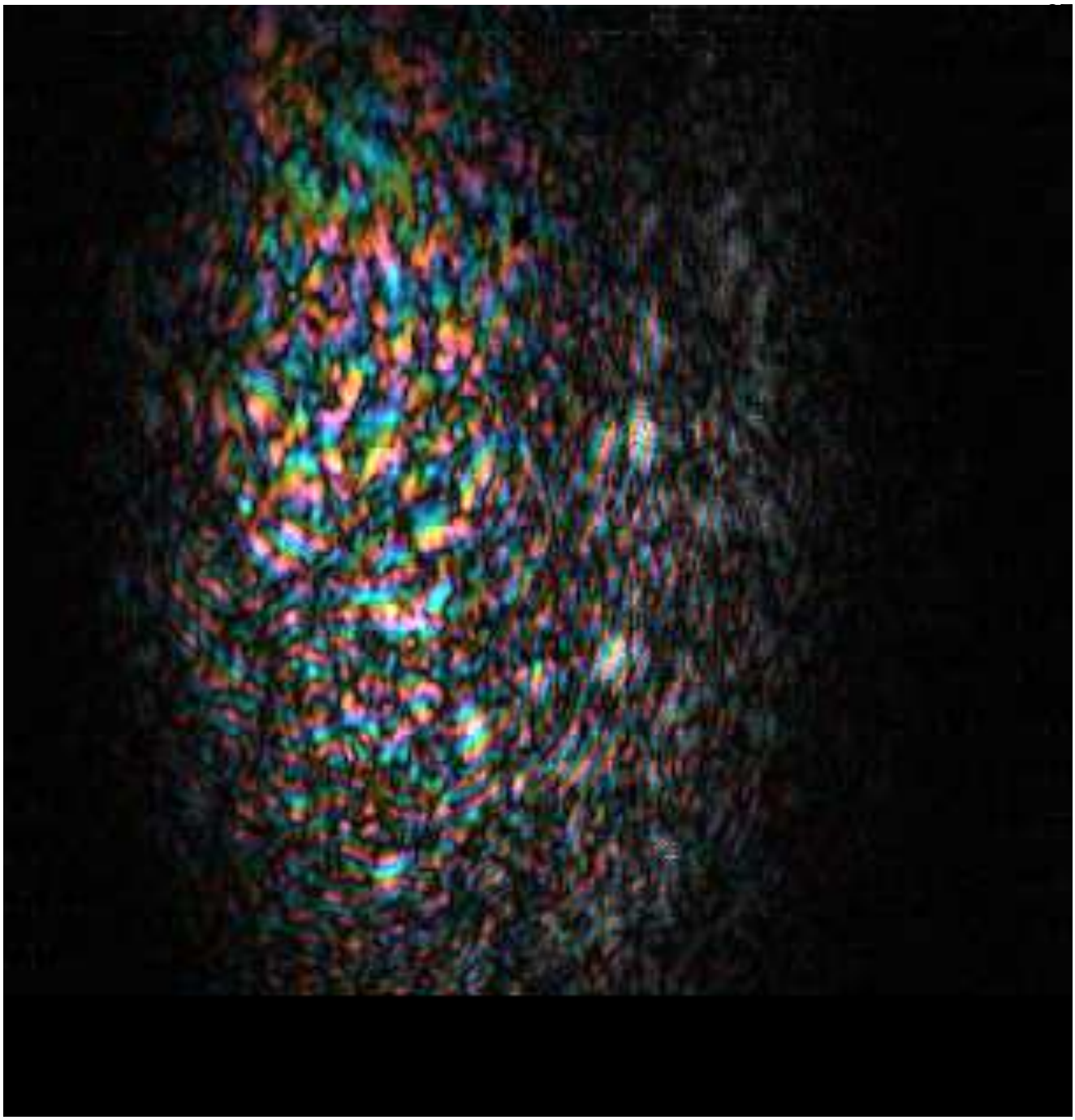

Figure 14: Phases measured by modulating pixels of the SLM. Groups of 8x8 segments where modulated in the hadamard basis. The modulation followed the protocol described in figure 7 with the difference that 8x8 segments were modulated, with the phase information taken from a 64x64 element Hadamard matrix. The groups of segments were measured in lines left to right, top to bottom.

when the scanning beam is focused onto the diffuser. Then we placed the SLM in the position where the image of the spot created by the combination of microscope objective and collimating lens was sharpest.

Second, we focused the scanning beam onto a 5 mm pinhole

using the 40x microscope in the setup and then set the SLM to only let a vertical slit of light pass. We adjusted the position of the vertical slit and the distance between the collimating lens and the SLM to maximize the amount of light from the slit of the SLM passing through the pinhole.

A third approach was to only let a vertical slit of light pass through the SLM and check the speckle pattern created by this slit. As a slit gets focused onto a scattering sample, the speckles become very wide. The optimal position is reached when the slit is focused onto the sample, which is the moment that the speckles emerging by the sample are at their widest.

Another approach, is to illuminate the sample with a vertical slit and move it in horizontally. When moving a beam across a diffuser, the speckles move, either in the same or in the opposite direction of the motion of the diffuser. This motion is caused by the curvature of the illuminating wavefront: Before the beam waist, the wavefront follows that of a converging, while after the beam waist, it follows the phase of a diverging spherical wave. As the sample moves, the tilt of the wavefront at a given position on the sample tilts, which makes the speckles move as described by the memory effect[18]. The moment when the SLM pixels are imaged onto the sample is also the moment when the beam waist of the beam from a single SLM pixel coincides with the plane of the sample. I used this approach while setting up the experiment, placing the sample at a distance where the speckles (both from the scanning beam and from the SLM beam) do not appear to move as the sample is moved horizontally, but rather, speckles seem to appear and disappear without any motion visible.

Mapping the Scanned Information to the SLM

To create a focus, first the phase and intensity contribution measured while scanning needs to be mapped onto the SLM. After mapping, there might be an additional position-dependent phase offset that has to be applied, to compensate, for example, an SLM that is not perfectly flat.

A simple approach would be to place a test target[4] into a focal plane of the steered beam which is also the image plane of the SLM. When scanning with the mirrors and measuring just the intensity,

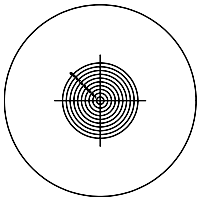

[4] We used the central part of a Thorlabs Positive Concentric Circle Reticle placed after a 75 mm lens that followed the pinhole in the setup. Scanning barely reached the edge of the first 1 mm diameter circle.

the cross becomes clearly visible. The same measurement can then be done with the SLM, letting light on the SLM pass through just a small square and then scanning this across the whole surface of the SLM, and will give the same image. Using the images from the two measurements, it should in principle be possible to create a mapping from mirror orientations to SLM pixels by comparing the images.

A better way is to place the SiPM onto the image plane of the two pinholes. At that plane, light from a single SLM pixel is parallel, as is light coming from the scanning mirrors, and by construction, illuminates a small circular area slightly bigger than the SiPM. If the mirror is set to scan, then a beating pattern will be observed only for the angles where the light from the mirrors is parallel to the light from one of the currently transmitting SLM pixels (see figure 15). So by allowing only the pixels corresponding to vertical or horizontal lines on the SLM to transmit light, one can scan which angles of the mirrors correspond to the x- and y-positions of the pixels on the SLM. From such a measurement, a lookup table can

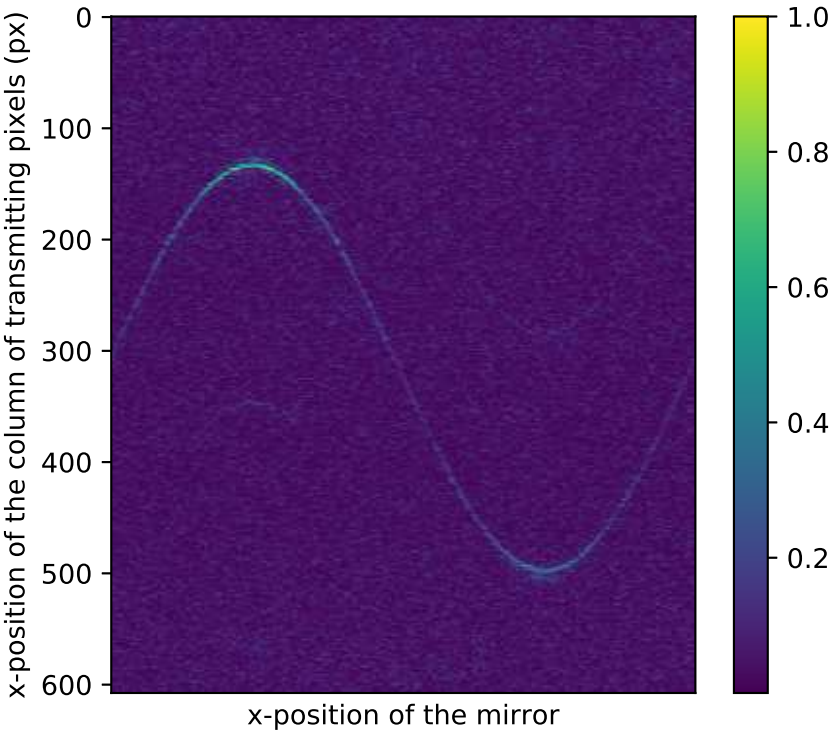

Figure 15: Amplitude of the beating pattern measured while scanning the x-mirror while different columns of the SLM are set to transmit light. The x-axis of the image corresponds to the time taken by the x-mirror for one harmonic oscillation of the x-mirror. It is this motion which creates the sinusoidal areas of high intensity.

be created that maps SLM-pixels to the corresponding angles of the mirrors.

The just described method performs well, the only difficulty is detecting the mirror positions corresponding to the SLM rows and columns from the noisy amplitude of the beating pattern acquired while scanning the mirrors. To solve the noise problem, we modeled the movement of the mirrors and fit this model to the acquired measurements.

In the setup, the angle of the y-mirror could be set by an output of the oscilloscope, so we were able to make the angle linearly dependent on time. This allows a simple linear regression to be used to map the positions of the y-mirror to the y-axes of the SLM. The x-mirrors angle, on the other hand, due to its resonant construction, follows a sinusoidal function. Here we fitted a sine function with offset, amplitude, and phase as parameters.

Creating the Optimal SLM Pattern

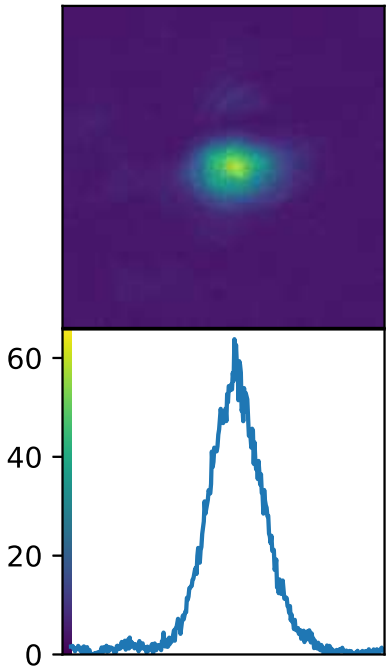

Figure 16: Preliminary results of the new new algorithm: The enhancement of a focus as an image (top) with its color bar (bottom left) together with a plot of the values of the brightest scanline (bottom).

To create the optimal wavefront, we first mapped the phase information acquired behind the turbid media to SLM pixels as described in the last section. In addition, we mapped the phase information acquired by placing the SiPM in a mirror plane of the pinhole, with all of the SLM set to pass light. This second measurement we used as a phase reference. To calculate the optimal phase to be placed onto the SLM, we multiplied the conjugate of the measurement with the reference measurement, giving values who's angle correspond to the phase of the optimal wavefront for all the SLM pixels. Then, since we ran our SLM in binary-amplitude modulation, we set the pixels where the real part of the optimal wavefront is positive to transmit light. This gave a clear focus at the position of our SiPM target (see figure 16) giving a enhancement factor of about sixty.

Optimizing the Data Processing and Outlook

While the measurement itself currently easily finishes in 20 ms, it is the calculation of the optimal wavefront that currently takes a couple of seconds. Currently, the setup acquires a I- and a Q-channel of the beating pattern at a sample rate of 100 MS/s. Of

these signals, the high frequency components are removed using a phase-preserving low-pass filter created by using an iir filter with filtfilt, after which the signal is decimated to a sampling frequency of 10 Ms/s and then mapped onto SLM pixels. Then, the pixel values are sent to the SLM over a DVI link.

Currently, the scanning system is set up to measure 400 oscillation of the x-mirror. With the horizontal mirror oscillating at 4 kHz, this gives 0.1 s per measurement. Another limit in the current setup is the delay introduced by buffers which the phase values pass through before they are sent to the DLP chip on the SLM: Data is sent to the SLM every $1/60^{\text{th}}$ of a second, so data has to wait in a buffer before it can be transmitted. Then, it takes a $1/60^{\text{th}}$ of a second to transmit all of the data across the DVI link before it can be displayed. In addition to the SLM side, there is also buffering on the oscilloscope side which introduces more delay. Measuring the computer-SLM-oscilloscope-computer round-trip gives a time of about 0.1 s.

It should be possible to remove the delay from both the SLM and from the oscilloscope side by streaming the data scanline-by-scanline from the oscilloscope to the computer, do the calculations, and start sending the data to the SLM while the measurement is still in progress. While scanning, light comming from the SLM pixels act as a reference to measure the phase of the scanning beam. If the SLM were updated scanline by scanline, then the reference would change durring a measurement, but that should not be a problem since all changes calculated for the SLM should, by construction, increase the intensity but not change the phase of the light reaching the detector from the SLM.

If these adjustments were made and the number of oscillations of the x-mirror were reduced to about 50 (which still gives a hundred scanlines because one can measure as the mirror is moving both ways) then a full measurement could be done in about 13 ms, which would be competitive with the 80 ms needed by Tao et al.[19], the fastest method I have found that works without requiring a setup that illuminates the sample from both sides.

The Transmission Matrix and Anderson Localization

Anderson localization is a phenomenon first proposed by P. W. Anderson in 1958 that predicts that in very strongly scattering media [1], photons have, compared to the predictions of the diffusion model, an enhanced probability of passing locations near positions they previously passed. My first project was to measure the transmission matrix of samples showing the signature of Anderson localization. We expected that the singular value decomposition of localizing and non-localizing samples would be statistically different, which would mean that the intensity distribution for the transmitting modes would differ for localizing and non-localizing samples[2]. Hoping to experimentally validate these expectations, I set out to measure the transmission matrix of localizing samples.

[1] Strong scattering for Anderson localization means that the wavenumber multiplied by the free scattering path, where $kl^* < 1$.

[2] Such an analysis, but ultrasound in brazen beads, has been described by [20].

The Transmission Matrix

The transmission matrix describes how light passes through a medium. If the phase and amplitude of input modes are described by a vector of complex values A_{input}, then the output modes can be calculated by multiplying the transmission matrix M with these values to give the phase and amplitude information of the output modes of the sample.

$$A_{\text{output}} = \text{M}A_{\text{input}}$$

Measuring the Transmission Matrix

When experimentally measuring the transmission matrix of a sample, the input modes A_{input} are usually mapped to pixels of an SLM

while the output modes are mapped to the pixels of a CCD. One way to measure the transmission matrix is to measure the phase of all the pixels of the CCD using the four-phase measurement technique with the phases of the SLM set to be in the Hadamard basis as described by Popoff et al.[11]. This method follows the process of focusing onto a single spot using the Hadamard basis as described in the last chapter, with the difference that during the four-phase measurements, all the pixels are recorded. As in the case of focusing, after each four-phase measurement, complex amplitudes can be calculated using equation (1), one for each CCD pixel. These complex amplitudes are in the Hadamard basis.

Reproduceability of the Measurement

To reproducibly measure a TM, the speckles created by the media need to be stable over the time of a measurement.

With the thick samples I used[3] , I was not able to get sufficient stability – there was no correlation between measurements seconds apart[4]. At the time, I suspected that some of the TiO_2 colloids were moving, which I tried to inhibit by freezing the sample in a cryostat to a temperature of 4° K. Cooling did not detectably change the speckle stability, however. I now believe that even with a stable sample, it would have been impossible to get a stable speckle pattern when using an insufficiently frequency-stable laser as I was using. I'll describe the calculations leading to this conclusion in the section.

[3] The samples were about 0.7 to 1.3mm thick, the minimum thickness at which we believed that localization would occur for our TiO_2 powders.

[4] With my setup, I was not able to measure at smaller intervals. Even though the sample was illuminated by a 2 W Verdi from coherent, there was insufficient light transmitted all the way through the 1 mm sample to record any meaningful speckles at exposure times below 1 s, making a useful analysis of the decorrelation time impossible.

The Lost Speckle Correlation

To simulate the effect of a drift in laser wavelength on the speckle correlation, I used time-of-flight (see figure 17) data of a typical 1mm sample. For each time step of the time-of-flight measurement, I created the complex amplitude of a random speckle pattern. These, weighted by the intensity of light measured at each time step, and then summed together, give the amplitude of the simulated speckle pattern. As a final step, to simulate a CCD which measures the intensity and not the complex amplitude, the square of the absolute value of the complex amplitude has to be calculated.

To simulate the speckle pattern for the same sample, but at a slightly different wavelength, I shifted the angle of the complex

amplitudes of the individual speckle patterns by $e^{it\Delta\omega}$. Here, t is the time corresponding to the complex speckle pattern and $\Delta\omega$ is the change in angular frequency between the original wavelength and the changed wavelength for which the speckle pattern is currently being calculated. This formula assumes that while the photons now have a slightly different wavelength, they still take the exact same path. Simulated images of the intensity for a given wavelength can be calculated by the following code:

```
def calculate_image(d_omega):
  # Input:  d_omega  - change in frequency
  #         I        - N ToF intensity values
  #         t        - time values corresponding to I
  #         speckles - complex amplitude of speckles,
  #                    N W*H 2d arrays
  # Output: intensity of the simulated speckle pattern
  #         of shape W*H

  m = I * np.exp(1j * d_omega * t)
  amplitude = (speckles * m[:,newaxis, newaxis]).sum(0)
  return np.abs(amplitude)**2
```

Listing 2: Calculation of the speckle pattern for a given change in light frequency

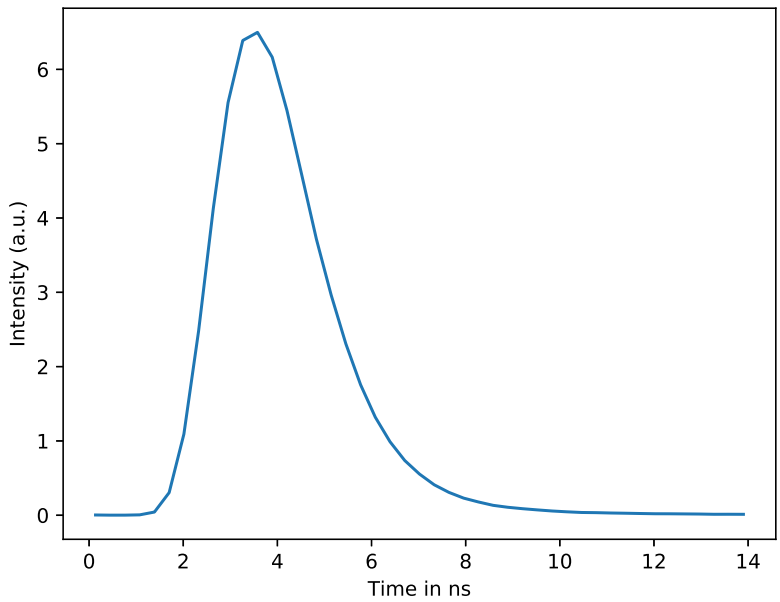

Figure 17: Time of flight $I(t)$ data used to calculate the speckle stability under change of wavelength.

Having simulated speckles for different wavelengths, it is now possible to calculate how the correlation of the speckles decays as the wavelength changes using an image correlation function:

```
def correlation(a,b):
  # calculate the correlation of two images a and b
  return ((a-a.mean())*(b-b.mean())).mean() \
           / (a.std() * b.std())
```

Listing 3: The correlation of two images

In the measurements, I used a Coherent Verdi V2. For a similar laser, the Verdi V5, extensive frequency stability measurements have been made (see figure 19) from which we can deduce that on the timescale of about five seconds, which is also the exposure time necessary to get sufficient light through our sample, that the laser drifts about 50 MHz. From our calculations above, after a drift of 50 MHz, there should still be a correlation of about 0.9. So with the assumptions made, the laser drift is not sufficiently large to explain the total lack of speckle correlation.

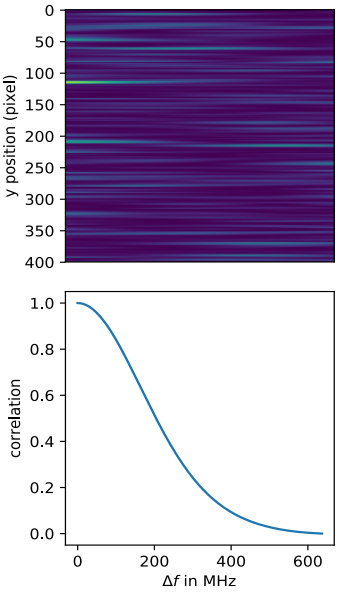

Figure 18: Decrease in the speckle correlation as the frequency of the illuminating laser changes. Top: a slice of the speckle pattern is shown for different wavelength shifts. Bottom: the correlation between two speckle patterns that are calculated for light with a given wavelength difference.

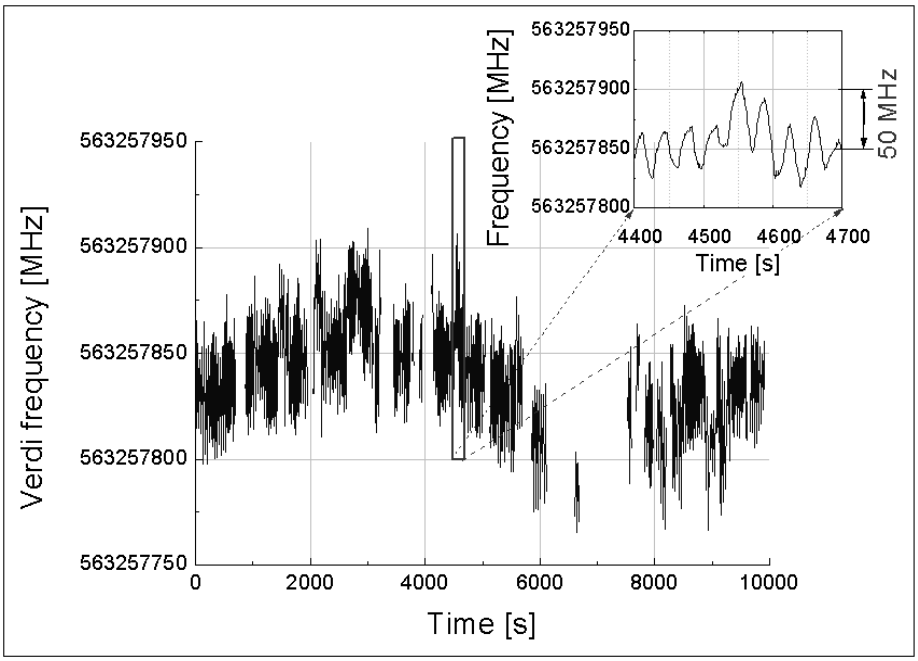

Figure 19: Frequency stability of a Verdi V5[21]

Temperature Stability

For the necessary temperature stability of the sample, the same approach can be used. We can assume that the whole sample expands homogeneously, and as before, that the light takes the same

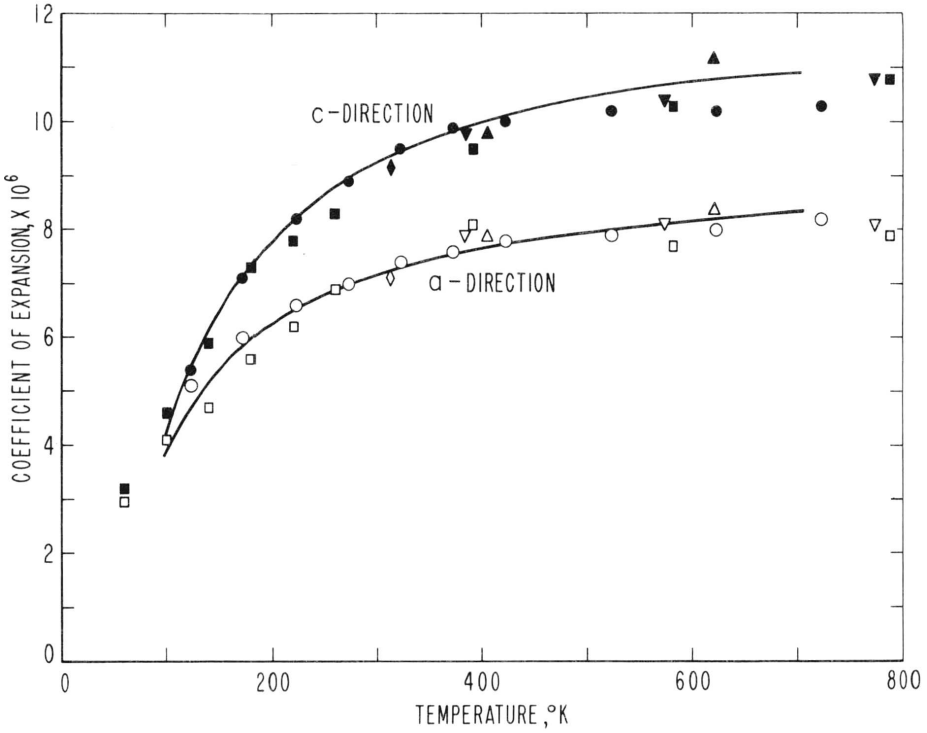

Figure 20: Expansion of TiO_2[22]

paths at all temperatures. For the temperature stability, one needs to know the thermal coefficient of expansion. From [22] one can deduce that the average expansion at room temperature should be about $\alpha_L = 8 \cdot 10^{-6}/^\circ$ while in liquid helium, extrapolating, it should be between $\alpha_L 1 \cdot 10^{-6}/^\circ$ and $\alpha_L 2 \cdot 10^{-6}/^\circ$ (see figure 20).

With the assumption from the last section, expanding the sample by a given fraction should have the same effect as reducing the wavelength by the same fraction. So for the speckle correlation, a temperature increase of 1° should, in approximation, be equivalent to an increase of the laser frequency of $\Delta f = \frac{c}{532\text{nm}} \cdot \alpha_L$. For the case of $\alpha_L = 1 \cdot 10^{-6}/^\circ$ this gives a Δf of about 600 Mhz/°. Assuming a sample temperature stability of 0.1°, this again is insufficient to explain the nonexistent speckle correlation for a sample in liquid helium.

Conclusion

While the calculations can not explain the total correlation of the speckles by themselves, they do show that, already with conservative assumptions, the speckle correlation would decrease to about 95% just with a laser frequency instability of 50 MHz or a temperature instability of 0.1°. This speckle decorrelation would probably

be to large to reliably measure the transmission matrix of our samples, and this effect should be taken into account if in the future, the transmission matrix of thick samples should be measured.

The non-existent correlation between neighboring measurements probably indicates that either the sample is non-static, or that the assumption made of light paths being independent of the wavelength and temperature does not hold.

A Postmortem of Anderson Localization of Light in 3D

While Anderson postulated localization in 1958[23], it took many years until the first claims of Anderson localization of infrared light in 3D turned up[24], though for the data in that paper, it was later shown that they could be explained with classical diffusion coupled with absorption[25].

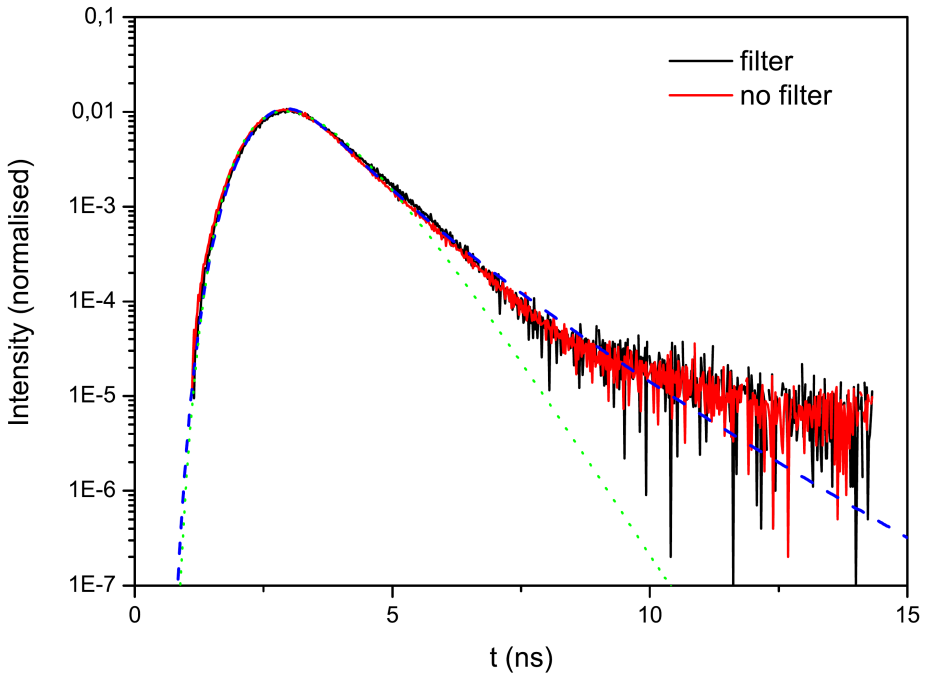

Figure 21: Plot from [26] showing time of flight data fitted with $I(t)$ of a localizing sample as given in equation (2). Note how at the long time tail, where the interesting physics of localization would be visible, the noise of the deconvolved data is very strong, and, when shown in log space, additionally highly asymetric, which makes the decision of where the curve should pass through the data a dificult decision.

In this section, I'll look into my groups claim to have observed Anderson localization of light in 3d slabs of TiO_2 powders. I'll describe the data analysis of the time-of-flight data, how it compares

to the profile measurements of Tilo Sperling, and finally describe how our redesigned data analysis helped show that what we earlier interpreted to be signs of localisation were actually signs of fluorescence.

Anderson Localization

Anderson localization[23] describes how with waves in a strongly scattering medium, the waves are scattered back stronger to positions they have already passed through than diffusion theory would predict. For an overview of Anderson localization, see [27].

Since we found our samples not to be localizing, I won't go too deep into the theory of localization but instead just give a quick overview of localization and how we expect it would affect the transport of light in turbid media. I'll later show that while most of our data qualitatively fits the expectations of localization, with a better analysis and also with new data of small samples it is evident that our samples do not show any localization.

To start, a simple model of localization in a strongly scattering sample states that the enhanced intensity of the wave returning to a position it has passed by before is caused by the many paths the wave can take to return to the origin. Each of the paths can be split into loops and subloops. The direction the loops are taken do not matter for the length of the path, so there are a lot of possible paths the wave can take which all constructively interfere. This strongly increases the intensity of the returning wave relative to the intensity expected in a pure diffusion model. We call light which travels on these constructively interfering loops localizing modes.

From this model, we can deduce that a sample needs to have a minimum size to show localization, else too many of the paths are cut off which would contribute to the through localization enhanced intensity. It was samples thinner than the localization length that originally got us to question our interpretation of our data[28].

When illuminated by a pulsed light source, we expect a part of the light to enter the localizing modes, stay in these for longer than diffusion theory would predict, but continuously leak out of these modes. We expect that light leaks out of the modes where the loops are cut at the border of the sample. At long times after an illuminating pulse, we expect that the intensity of light emitted by

the sample will be dominated by the leakage of localized modes, resulting in a signal stronger than pure diffusion would predict, as shown figure 21.

Additionally, if a point of our sample is illuminated by a laser pulse on one side, then we expect that on the other side, the spot would first grow as predicted by diffusion, and then at long times, to stop growing at long times when the light of localizing modes dominates. While our measurements also followed this prediction (see figure 22 and [29]) we later found there was a simpler explanation for our data.

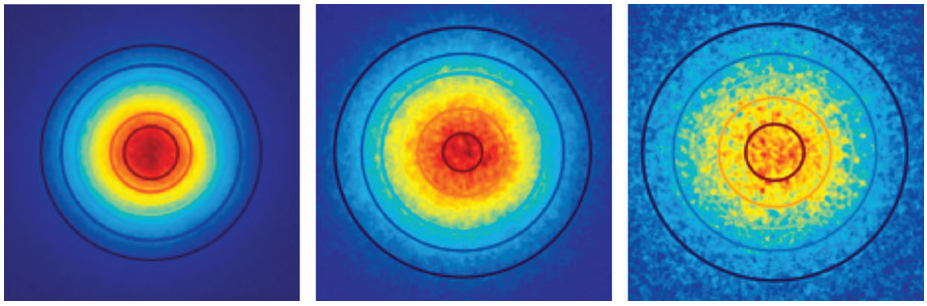

Figure 22: Profile created by illuminating a sample of TiO_2 by a laser pulse and taking an image on the other side 4 ns, 6 ns and 8 ns after the pulse entered the sample. Between 4 ns and 6 ns, the pulse clearly grows, while from 6 ns to 8 ns, the size no longer changes[29].

ToF Experimental Setup

The experimental setup to measure the time of flight (ToF) data consists of a pumped titanium sapphire laser (HP Mira) followed by a frequency doubled OPO to produce visible light pulses with a pulse width of about 250 fs and a repetition rate of 76 MHz. After passing through a sample, the light pulses are detected by a fast photomultiplier (HPM-100-40). The signals from the photomultiplier are then counted by a multichannel analyzer. Because of the dead time of the photon multiplier and because of limits of the multichannel analyzer, the photon detection rate is kept below one detection per pulse through the use of neutral-density filters.

Theoretical ToF Curve to Interpret the Data

Because calculating $I(t)$ for a localizing sample thousands of mean free paths thick was at the time computationally not feasible[26],

our group first used a poor man's approximation that extended the $I(t)$ for a non-localizing sample.

For a scattering medium not showing Anderson localization, the measured $I(t)$ for light from a laser pulse can be described by a standard equation for diffusion given by

$$I(t) \propto e^{-t/\tau_{\text{abs}}} \cdot \sum_n (-1)^{n+1} n^2 \exp[-n^2\pi^2 Dt/L^2], \qquad (1)$$

where τ is the absorption length and L is the thickness of the sample, and D is the diffusion coefficient. For localizing samples, we expect that the diffusion-coefficient is non-constant, but reduces at large times. We change $I(t)$ to

$$I(t) \propto e^{-t/\tau_{\text{abs}}} \cdot \sum_n (-1)^{n+1} D(t)/D_0 n^2 \exp[-n^2\pi^2 D(t)t/L^2], \quad (2)$$

where $D(t)$ is a time dependent diffusion coefficient given by $D(t) = D_0\tau_{\text{loc}}^a/(\tau_{\text{loc}}^a + t^m)^{a/m}$ where τ_{loc} is the localization time, m is a cross-over exponent set to $m = 10$ and a is the localization exponent describing the decay of D at large times given by $D(t) \propto t^{-a}$[26]. How we fitted these functions will be described in the next section.

Because by 2015, computers had gotten quite a bit faster, I attempted to optimize and parallelize the code based on self consistent theory written by [30] and used by [31], hoping to use it to fit the $I(t)$ we measured from samples we believed to be localizing. The optimizations I made to the code, decreasing the time of the calculations by three orders of magnitude, are described in appendix A.

While working on the self-consistent code, new measurements of very thin samples, thinner than the localization length, also showed the signature long time tail we believed to be caused by localization (see figure 23). Since these samples where way thinner than the localization length, we did not expect to see localization in them. We made further measurements where we flooded the TiO_2 samples with water. If the samples were actually localizing, then flooding with water should change the difference in refractive index between the TiO_2 particles and their surrounding to reduce the scattering strength to give a $kl \gg 1$ for which localization is impossible. Since we still saw the long time tail with the same decay constant, a new theory was needed to describe our data.

I developed a new model based on $I(t)$ for the pure diffusive case, but adjusted the curve to take into account that the TiO_2 particles

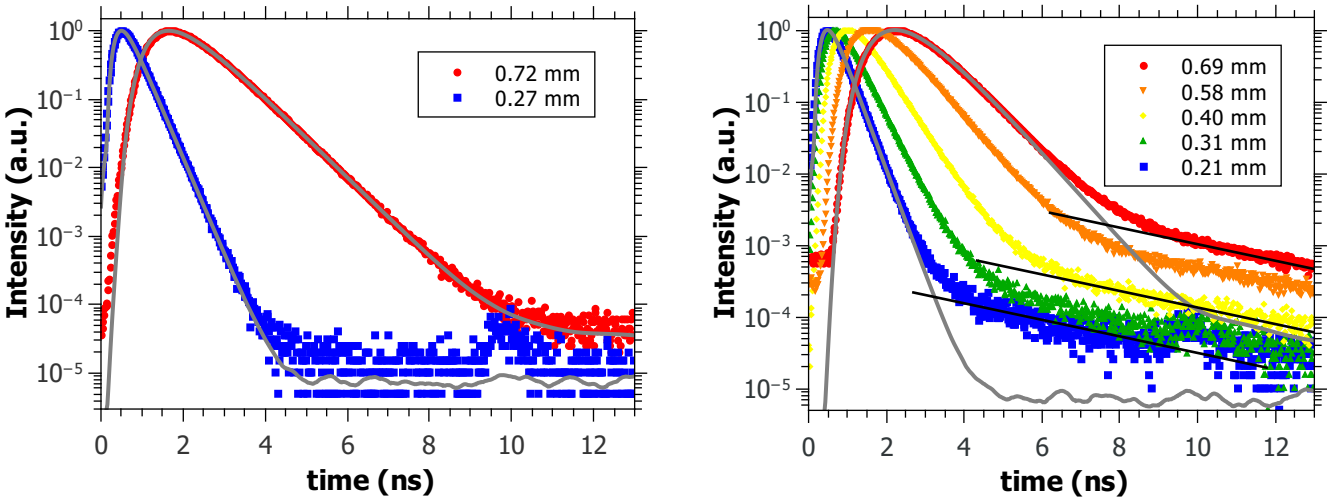

Figure 23: Time of flight measurement of samples to thin to be localizing, top: Anatase, bottom: R700. The gray lines are the pure diffusion fit. The R700 measurements clearly show a deviation from the ToF profile expected for a purely diffusive sample. In the R700 sample, it is clearly visible that after the peak intensity, the intensity decreases following an exponential decay modeled by diffusion theory, followed by another exponential decay (made visible by the black lines) at longer times that has a larger time constant. From [28].

we used can absorb photons and re-emit them later through fluorescence. For this, I introduced a new function $p(t_{sc}, t_d)$ that describes the probability that a photon that, under pure diffusion, would take t_{sc} to pass through the medium, is delayed by an additional time t_d. The delay probability is calculated by

$$p(t_{sc}, t_d) = (1 - r_{fl}\, t_{sc})\delta(t_d) + r_{fl}\, t_{sc} \frac{\exp(-t_d/\tau_{fl})}{\int_0^\infty \exp(-t'/\tau_{fl})\, dt'}. \quad (3)$$

In this function, r_{fl} is the rate that photons are absorbed and τ_{fl} is the decay time of the fluorescenct state. Both τ_{fl} and r_{fl} are material constants that do not change for different sample thicknesses. The function $p(t_{sc}, t_d)$ makes two assumptions: That photons undergo at most a single fluorescence process and that no photons are lost in the fluorescence process. For the first assumption, note that the absorption rate is small enough that there are to few photons undergoing multiple fluorescence processes to measurably change the intensity profile of $I(t)$. For the second assumption, adding an extra parameter might make sense, but already this simple model fits much better than the localizing model used previously so we omitted this parameter for simplicity.

Analyzing the Time of Flight Data

While the pulse length of the laser is on the order of a picosecond, the time resolution of the system as a whole is limited by the channel size of the multichannel analyzer but also by the response time of the photomultiplier. Without any scattering media, the measured intensity curve has a width of about 0.2 ns, which is orders of magnitudes bigger than the pulse width of the laser (250 fs). We treat this reference measurement as the response function of the whole measurement setup. When measuring an actual scattering sample, the peak of the recorded data will be widened by this response function. To compare the experimental data to theory, there are two options: Either the data has to be deconvolved by a reference measurement as done by my predecessors[32], or else, the theoretical data has to be convolved with the reference measurement[33]. In the next paragraphs, I'll try to make the argument for why convolving the theoretical data is the better option than to deconvolve the measurement.

To Deconvolve, or not to Deconvolve

A convolution $I_{\text{meas}} = I_{\text{ref}} * I_{\text{actual}}$ can be calculated in the fourier space by

$$I_{\text{meas}} = IFFT(FFT(I_{\text{ref}}) \odot \text{FFT}(I_{\text{actual}}))$$

where $\odot$ is the elementwise Hadamard product. Solving for the signal without the effects of the photomultiplier gives

$$I_{\text{actual}} = \text{IFFT}(\text{FFT}(I_{\text{meas}})/\text{FFT}(I_{\text{ref}}))$$

where / is the elementwise division. This works alright as long as $\text{FFT}(I_{\text{ref}})$ does not contain values close to zero. If there are values close to zero, then the corresponding frequencies of I_{meas} will be strongly enhanced, which produces high-frequency noise as is visible in figure 21. This high-frequency noise could be reduced through filtering. If one were to filter the signal, care would have to be taken to prevent the strongly rising signal on the left from shifting further to the left, as happens when using a convolution filter when filtering a signal that increases orders of magnitude over a very short time.

If one insists on deconvolution, other methods might give better results. A possible example is Gold deconvolution, a method that, relative to the FFT based method, produces a deconvolved signal with a lot less noise. Such a deconvolution is show in figure 24, also showing that the deconvolved signal follows quite closely the theoretical curve calculated directly from the raw data.

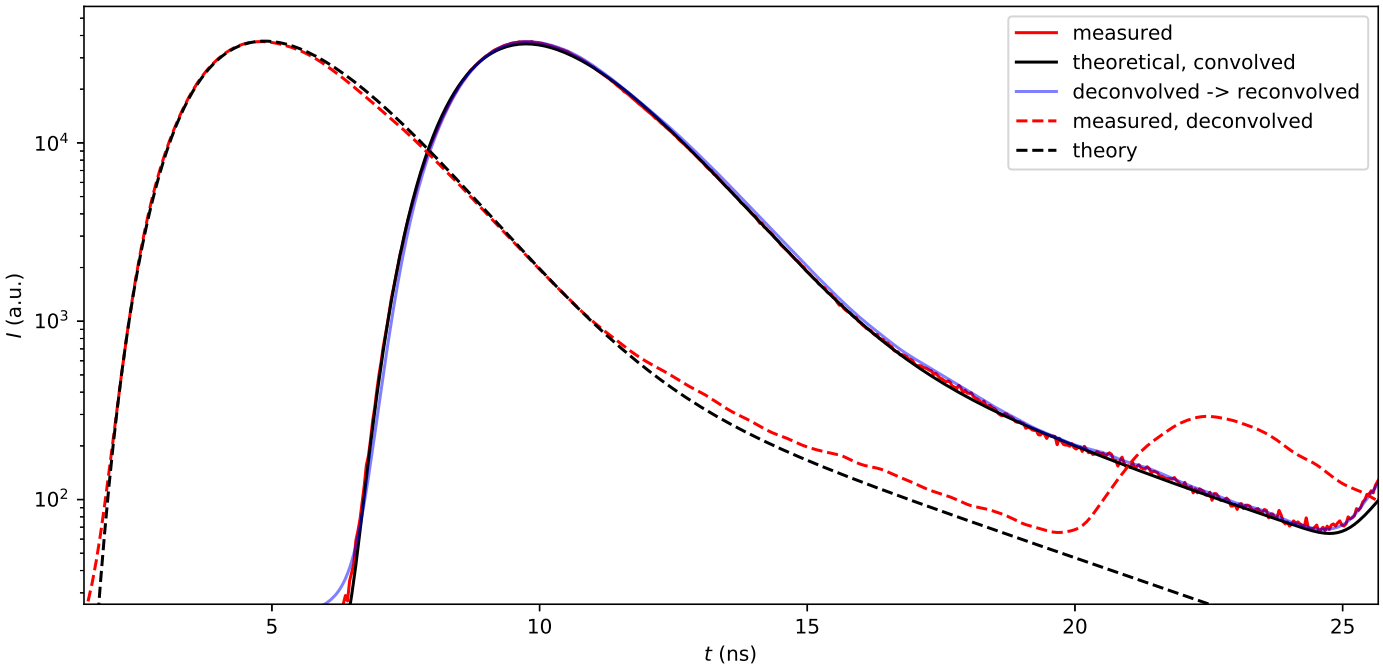

Figure 24: Plot of ToF measurement of R700 taken in 2005 showing the raw data (red) fitted with the equation for diffusion with luminescence and convolved with the response of the setup (black). Additionally, the signal deconvolved with a Gold deconvolution of three iterations (dashed red) and the equation from before, without convolution (dashed black) is shown. Finally, the deconvolved signal reconvolved with the response function (blue) is shown, to check if the deconvolution is reversible. In the deconvolved signal, the afterpulse of the laser is visible on the right, which is the next pulse generated by the laser, but strongly reduced in intensity by the pulse picker. Note that while the deconvolved signal deviates quite a bit from the curve fitted with the raw signal at long times, it still has the same slope in log space.

The Loss Function

When fiting with least squares, one has to decide whether the loss function L to minimize is calculated using the difference of the intensities

$$L = \sum_t \left(I_{\text{meas}}(t) - I_{\text{theo}}(t)\right)^2$$

or the difference of the log of the intensities

$$L = \sum_t \left(\log(I_{\text{meas}}(t)) - \log(I_{\text{theo}}(t))\right)^2.$$

Because localization would be visible in the tail of the measurement, and the tail has a much lower intensity, the second option makes sense, because since the curve has such a large change in magnitude between the peak and the tail, with the first option, the tail hardly contributes to the loss function.

When fitting in log space, care has to be taken to minimize the noise since at high noise levels, after the conversion to log space, the noise is no longer symmetric but is skewed to low values (see figure 21) so minimizing a function like

$$L = \sum_t \left(I_{\text{meas}}(t) - I_{\text{theo}}(t)\right)^2 / I_{\text{meas}}^2.$$

that works in linear space while still giving more weight to the long time tail might make more sense.

To solve the noise problem, we switched from fitting deconvolved data to fitting a theoretical curve convolved with the system response, just like Watson, Fleury and McCall in their paper on time of flight measurements of diffusive samples[1]. Results of such fit are shown figure 24 and figure 25. Note that our new model also explains the profile data mentioned in the introduction to Anderson localization. By taking a Gaussian profile that grows with time according to diffusion theory, multiplying this by $I(t)$ from diffusion theory, and then using the delay probability from equation (3), the profile for a luminescent sample can be calculated. If these profiles are then fitted with a Gaussian, one finds that the spot size closely follows the experimental data (see the right part of figure 25).

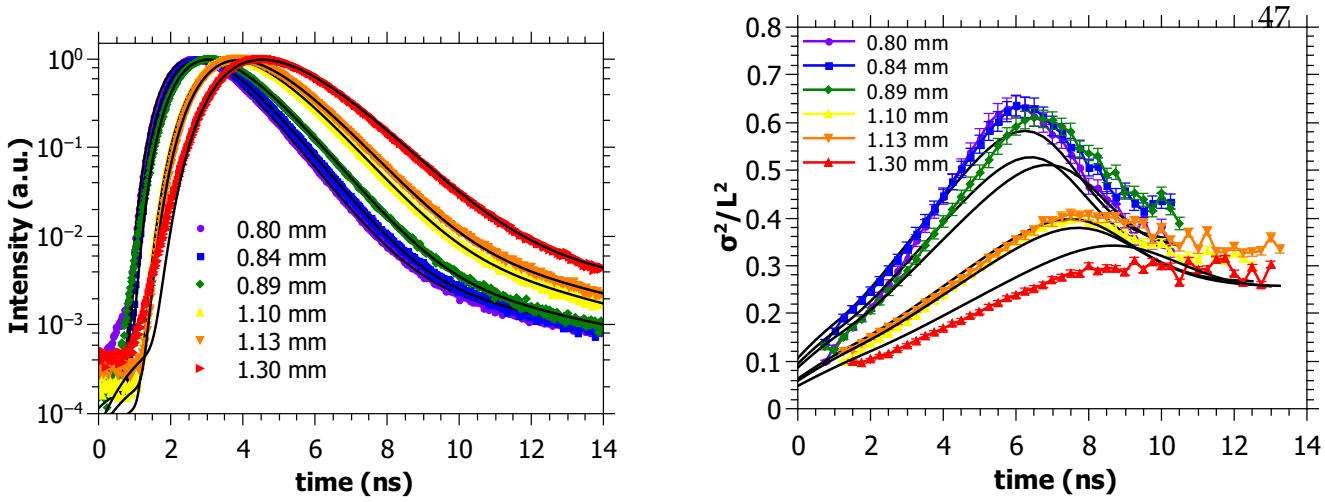

Figure 25: Time of flight (left) and profile measurement (right) of TiO_2 samples. For each sample, the Time of flight data and the profile data were fit with a single set of parameters. For each of the curves, the decay constant $\tau_{fl} = 3.85$ ns was taken from the fit shown in figure 26. The only fit parameters left were the absorption coefficient τ_a, the diffusion coefficient D the absorption rate r_{fl}, and for the profiles, an additional parameter describing the spot size of the illuminating beam.

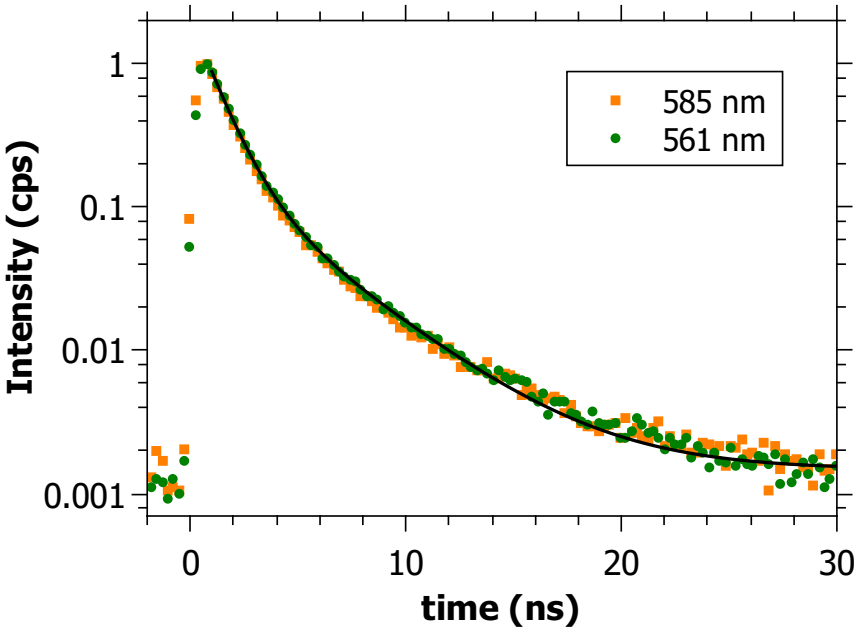

Figure 26: Lifetime measurement of the luminescence

Conclusion

In this thesis, I introduced a novel method to focus through turbid media. The current setup can measure a scan line of the optimal wavefront in 1/4000 of a second, which allows it to measure the optimal wavefront at a vertical resolution of 200 lines, a sufficient resolution to create a focus, in fifty milliseconds. I showed that the method works with a diffusor as scattering media. In the future, it would be interesting to optimize the algorithm to take less time by reducing the number of scanlines and additionally optimizing the software to see how the method performs with non-static scattering media such as biological tissue.

Besides this new method, I described how in thick samples of scattering media, the frequency stability of the illuminating light source is very important. For this, I proposed a computational model that can predict how fast the speckle correlation is lost as the illuminating wavelength changes. This model could be useful in the future if localizing samples are found, which would raise the question about the properties of these samples' transmission matrix.

Finally, I discussed the difficulties in interpreting time of flight data of samples suspected to be Anderson localizing. I explained how the fit to noisy data, when viewed in log space, can lead to systematic errors. Additionally, I demonstrated how this problem can be reduced by convolving the theoretical curve with the system response, instead of deconvolving the measurement curve with the system response. Finally, I showed how luminescence can explain the data of samples we thought to be localizing, with a model that, with a single set of parameters, fits both the intensity values of the time of flight measurements but also the spot sizes from the profile measurements.

Bibliography

[1] G.H. Watson, P.A. Fleury, and S.L. McCall, Searching for photon localization in the time domain, *Physical Review Letters* **58**(9), 945–948 (1987).

[2] T. Sperling, *The Experimental Search for Anderson Localisation of Light in Three Dimensions*, (PhD thesis). Universität Konstanz, Konstanz (2015).

[3] R. Amézquita, O. Rincón, and Y.M. Torres, Aberration compensation using a spatial light modulator LCD, *Journal of Physics: Conference Series* **274** 012111 (2011).

[4] H. Zhu, P. Bierden, S. Cornelissen, T. Bifano, and J.H. Kim, Design and fabrication of reflective spatial light modulator for high-dynamic-range wavefront control, (2004).

[5] V. Shrauger and C. Warde, Development of a high-speed high-fill-factor phase-only spatial light modulator, (2001).

[6] D. Wang, E.H. Zhou, J. Brake, H. Ruan, M. Jang, and C. Yang, Focusing through dynamic tissue with millisecond digital optical phase conjugation, *Optica* **2**(8), 728 (2015).

[7] E. Hecht, *Optik* (Oldenbourg Verlag München, 2002).

[8] D.B. Conkey, A.M. Caravaca-Aguirre, and R. Piestun, High-speed scattering medium characterization with application to focusing light through turbid media, *Optics Express* **20**(2), 1733 (2012).

[9] D. Akbulut, T.J. Huisman, E.G. van Putten, W.L. Vos, and A.P. Mosk, Focusing light through random photonic media by binary amplitude modulation, *Optics Express* **19**(5), 4017 (2011).

[10] I.M. Vellekoop and A.P. Mosk, Universal Optimal Transmission of Light Through Disordered Materials, *Physical Review Letters* **101**(12), (2008).

[11] S.M. Popoff, G. Lerosey, R. Carminati, M. Fink, A.C. Boccara, and S. Gigan, Measuring the Transmission Matrix in Optics: An Approach to the Study and Control of Light Propagation in Disordered Media, *Physical Review Letters* **104**(10), (2010).

[12] H. Yu, T.R. Hillman, W. Choi, J.O. Lee, M.S. Feld, R.R. Dasari, and Y. Park, Measuring Large Optical Transmission Matrices of Disordered Media, *Physical Review Letters* **111**(15), (2013).

[13] Y. Liu, C. Ma, Y. Shen, J. Shi, and L.V. Wang, Focusing light inside dynamic scattering media with millisecond digital optical phase conjugation, *Optica* **4**(2), 280 (2017).

[14] A.S. Hemphill, Y. Shen, Y. Liu, and L.V. Wang, High-speed single-shot optical focusing through dynamic scattering media with full-phase wavefront shaping, *Applied Physics Letters* **111**(22), 221109 (2017).

[15] J.B. Saunders, Some Applications of the Wave Front Shearing Interferometer, *JOURNAL OF RESEARCH of the National Bureau of Standards - C. Engineering and Instrumentation* **69C** (1965).

[16] A. Migdall, S. Polyakov, J. Fan, and J. Bienfang, *Single-Photon Generation and Detection: Physics and Applications*, pp.. 69-82 (Academic Press, 2013).

[17] sensl, J-Series DATASHEET, (2017).

[18] I. Freund, M. Rosenbluh, and S. Feng, Memory Effects in Propagation of Optical Waves through Disordered Media, *Physical Review Letters* **61**(20), 2328–2331 (1988).

[19] X. Tao, D. Bodington, M. Reinig, and J. Kubby, High-speed scanning interferometric focusing by fast measurement of binary transmission matrix for channel demixing, *Optics Express* **23**(11), 14168 (2015).

[20] H. Hu, A. Strybulevych, J.H. Page, S.E. Skipetrov, and B.A. van Tiggelen, Localization of ultrasound in a three-dimensional elastic network, *Nature Physics* **4**(12), 945–948 (2008).

[21] N. Beverini, N. Poli, D. Sutyrin, F.Y. Wang, M. Schioppo, M.G. Tarallo, and G.M. Tino, Absolute frequency measurement of unstable lasers with optical frequency combs, (2010).

[22] R.K. Kirby, Thermal Expansion of Rutile from 100 to 700 °K, *JOURNAL OF RESEARCH of the National Bureau of Standards – A. Physics and Chemistry* **71A** (1967).

[23] P.W. Anderson, Absence of Diffusion in Certain Random Lattices, *Physical Review* **109**(5), 1492–1505 (1958).

[24] D.S. Wiersma, P. Bartolini, A. Lagendijk, and R. Righini, Localization of light in a disordered medium, *Nature* **390**(6661), 671–673 (1997).

[25] F. Scheffold, R. Lenke, R. Tweer, and G. Maret, Localization or classical diffusion of light?, *Nature* **398**(6724), 206–207 (1999).

[26] C.M. Aegerter, M. Störzer, S. Fiebig, W. Bührer, and G. Maret, Observation of Anderson localization of light in three dimensions, *Journal of the Optical Society of America A* **24**(10), A23 (2007).

[27] A. Lagendijk, B. van Tiggelen, and D.S. Wiersma, Fifty years of Anderson localization, *Physics Today* **62**(8), 24–29 (2009).

[28] T. Sperling, L. Schertel, M. Ackermann, G.J. Aubry, C.M. Aegerter, and G. Maret, Can 3D light localization be reached in `white paint'?, *New Journal of Physics* **18**(1), 013039 (2016).

[29] T. Sperling, W. Bührer, C.M. Aegerter, and G. Maret, Direct determination of the transition to localization of light in three dimensions, *Nature Photonics* **7**(1), 48–52 (2012).

[30] S.E. Skipetrov and B.A. van Tiggelen, Dynamics of Anderson Localization in Open 3D Media, *Physical Review Letters* **96**(4), (2006).

[31] H. Hu, A. Strybulevych, J.H. Page, S.E. Skipetrov, and B.A. van Tiggelen, Localization of ultrasound in a three-dimensional elastic network, *Nature Physics* **4**(12), 945–948 (2008).

[32] C.M. Aegerter, M. Störzer, and G. Maret, Experimental determination of critical exponents in Anderson localisation of light, *Europhysics Letters (EPL)* **75**(4), 562–568 (2006).

[33] T. Sperling, W. Bührer, M. Ackermann, C.M. Aegerter, and G. Maret, Probing Anderson localization of light by weak non-linear effects, *New Journal of Physics* **16**(11), 112001 (2014).

[34] G.B. Rybicki and D.G. Hummer, Fast Solution for the Diagonal Elements of the Inverse of a Tridiagonal Matrix, (1990).

Apendix A

A fast method to find the diagonal of the inverse of a tridiagonal matrix

The self-consistent code by written by Sergey Skipetrov that has been used to self-consistently calculate time-of-flight intensity values and profiles of Anderson localising samples[30] uses a tridiagonal matrice M to describe the position-dependent diffusion. In the inner most loop of the program, it spends most of its time solving an equation of the form $Mx = e_i$ using the ZGTSL BLAS routine. In this equation, e_i is a vector that is all zeros except for the ith element which is one. While I was optimizing the code to use it to fit our curves, I noticed the code only cares about the i'th element of x. From a calculation standpoint, these calculations are the same as calculating a matrix $MX = 1$ and keeping only the diagonal elements of the matrix X. For the calculation of $X = M^{-1}$, I found a more efficient method proposed by Rybicki and Hummer [34] which, when implemented in the program, removes the innermost loop, reducing the running time by a factor of thousand for a system size as described in [31]. For localization of light, where the sample size (measured in the number of mean free paths) is much larger than for the ultrasound samples, the gain from this optimization would probably be even larger.

What follows on the next page is the code to calculate the diagonals of X, in its FORTRAN77 glory:

```
c *
c * fsdeitm implements the algorithm of the paper
c * "Fast Solution for the Diagonal Elements of the Inverse of a
c * Diagonal Matrix"
c *
      subroutine fsdeitm(right, diag, left, lambda, m)
      integer m, i
      complex*16 left(1:m), diag(1:m), right(1:m), lambda(1:m)


c * inup and indn are source vectors that when multiplied with the
c * tridiagonal matrix give a vector that contains all zeros exept for the
c * last/first position.  The last/first position will probably contain a
c * non-zero value.

      complex*16 inup(1:m), indn(1:m)
c *   intensity comming from left or above / right or above
      complex*16 factor, tmp, nz, tmp1, tmp2, tmp3, tmp4

      inup(1) = 1
      do i = 1, m
        tmp = diag(i) * inup(i)
        if (i.GT.1) then
          tmp = tmp + right(i) * inup(i-1)
        end if
        if (i.LT.m) then
          inup(i+1) = -tmp / left(i)
          tmp3 =      -tmp / left(i)
        endif


        if (i.NE.m .AND. i.NE.1) then
          tmp1= diag(i) * inup(i) + right(i) * inup(i-1)
          tmp2= tmp1 + inup(i+1) * left(i)
        endif
      end do

      indn(m) = 1
      do i = m, 1, -1
        tmp = diag(i) * indn(i)
        if (i.LT.m) then
          tmp = tmp + left(i) * indn(i+1)
        end if
        if (i.GT.1) then
          indn(i-1) = -tmp / right(i)
        endif

        if (i.NE.m .AND. i.NE.1) then
          tmp1= diag(i) * indn(i) + right(i) * indn(i-1)
          tmp2= tmp1 + indn(i+1) * left(i)
        endif
      end do
```

```
c * inup and indn now contain solutions that (except for their respective
c * end points,  consist entirely of zeros, except at their respective ends.
c * Now, splice the start of inup with the end of indn, each with some
c * factor, so that applying the spliced vector to the tridiagonal matrix
c * results in a vector that has only one non-zero element. Use that to
c * calculate the value of its corresponding lambda value. The non-zero
c * value can be on the left or right of the splice. Calculate both, and use
c * the better one.

      do i = 1,m

        nz = diag(i) * inup(i)
        if (i.NE.1) then
          nz = nz + right(i) * inup(i-1)
        endif

c * find out by how much the from the right has to be multiplied to get a
c * zerro at i+1 factor = inup(i) / indn(i)

        if (i.NE.m) then
          nz = nz + factor * left(i) * indn(i+1)
        endif

        lambda(i) = inup(i)/nz

      enddo
      end
```

Appendix B

Contribution to the Papers in this Appendix

For the first two papers, *Can 3D light localization be reached in 'white paint'?* and *Probing Anderson localization of light by weak nonlinear effects*, my main contributions were rewriting the curve fitting code used to analyze the data, which included the methodological improvements described in the chapter *A Postmortem of Anderson Localization of Light in 3D*. In addition, for the second paper, I developed a luminescent theory that was able to describe our time-of-flight data for both the intensity and for the profile measurements, and implemented it in our curve fitting code. In addition, I extended our curve fitting code to fit our intensity and our profile data using a single set of parameters, as is described in the second of the two papers.

Besides improving the evaluation of our time-of-flight data, I repaired the electronics of the setup used to measure the backscattering cone of our strongly scattering samples, with which the kl* values in the papers were measured. Besides fixing the wiring, the repair consisted of changes to the setup to almost completely eliminate noise from electromagnetic interference.

For the paper, *Structured illumination behind turbid media*, I introduced the method of using the Fourier transform to calculate predicted spot patterns for given phase masks. I also developed the stochastic algorithm presented in the paper to create a optimal phase mask for a 4x4 pattern.

IOP Publishing New J. Phys. 18 (2016) 013039 doi:10.1088/1367-2630/18/1/013039

New Journal of Physics
The open access journal at the forefront of physics

Deutsche Physikalische Gesellschaft DPG
IOP Institute of Physics

Published in partnership with: Deutsche Physikalische Gesellschaft and the Institute of Physics

OPEN ACCESS

RECEIVED
24 September 2015

REVISED
19 November 2015

ACCEPTED FOR PUBLICATION
4 December 2015

PUBLISHED
18 January 2016

PAPER

Can 3D light localization be reached in 'white paint'?

T Sperling[1,3], **L Schertel**[1,2,3], **M Ackermann**[2,3], **G J Aubry**[1], **C M Aegerter**[2] **and G Maret**[1]

[1] Fachbereich Physik, Universität Konstanz, D-78457 Konstanz, Germany
[2] Physik-Institut, Universität Zürich, Winterthurerstr 190, 8057 Zürich, Switzerland
[3] These authors contributed equally.

E-mail: Georg.Maret@uni-konstanz.de

Keywords: Anderson localization of light, fluorescence, titania powder

Abstract

When waves scatter multiple times in 3D random media, a disorder driven phase transition from diffusion to localization may occur (Anderson 1958 *Phys. Rev.* **109** 1492–505; Abrahams *et al* 1979 *Phys. Rev. Lett.* **42** 673–6). In '*The question of classical localization: a theory of white paint?*' Anderson suggested the possibility to observe light localization in TiO_2 samples (Anderson 1985 *Phil. Mag.* B **52** 505–9). We recently claimed the observation of localization effects measuring photon time of flight (ToF) distributions (Störzer *et al* 2006 *Phys. Rev. Lett.* **96** 063904) and evaluating transmission profiles (TPs) (Sperling *et al* 2013 *Nat. Photonics* **7** 48–52) in such TiO_2 samples. Here we present a careful study of the long time tail of ToF distributions and the long time behavior of the TP width for very thin samples and different turbidities that questions the localization interpretation. We further show new data that allow an alternative consistent explanation of these previous data by a fluorescence process. An adapted diffusion model including an appropriate exponential fluorescence decay accounts for the shape of the ToF distributions and the TP width. These observations question whether the strong localization regime can be reached with visible light scattering in polydisperse TiO_2 samples, since the disorder parameter can hardly be increased any further in such a 'white paint' material.

1. Introduction

The prediction of a disorder induced metal-insulator phase transition made by Anderson [1] and the generalization as a wave phenomenon [6] stimulated many theoretical and experimental studies over more than 50 years [7]. Scaling theory predicts a phase transition from classical diffusion to localization to occur above two-dimensions only [2, 8]. Furthermore, advances [9, 10] in the self-consistent theory [11] predict a position and time dependent diffusion coefficient in the localized regime. Experimental verifications of this phase transition in three-dimensional highly scattering media has been a challenging task ever since. There are experimental reports with light [4, 5, 12, 13], ultrasound [14] and ultra cold atoms [15–18], but doubts have been raised concerning the interpretation of some of these results in terms of localization of light waves ([19–21] and [22, 23]) and for ultra cold atoms [24, 25].

This controversial discussion illustrates the difficulty to carry out sufficiently complete and accurate sets of experiments, to fabricate appropriate samples and, finally, to reach a consistent interpretation of all results. In previous publications [4, 5, 23, 26–29] we interpreted our measurements on strongly scattering TiO_2 powders as evidence for strong localization of light in three-dimensions, as suggested by Anderson [3]. However, inconsistencies of recent data with the interpretation of Anderson localization led us to perform additional sensitive experimental tests.

In this article, after presenting our experimental setups (section 2), we will show (in section 3) new multiple light scattering measurements, where deviations from the diffusion theory are observed. While these deviations were previously interpreted as Anderson localization, we now observe similar deviations in regimes of weak multiple scattering where Anderson localization should not occur. In section 4, we characterize a weak fluorescent signal we find in all powders that were supposed to localize and show that the scaling of the

IOP Publishing New J. Phys. 18 (2016) 013039 T Sperling et al

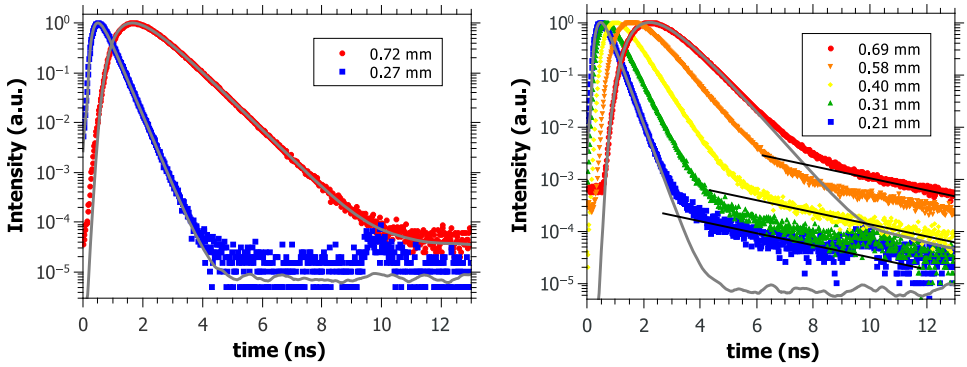

(a) Aldrich anatase (b) R700

Figure 1. (a) ToF distributions for a thin ($L = 0.72$ mm) and a very thin ($L = 0.27$ mm) AA sample are shown. The diffusion fit (solid gray lines) matches perfectly. (b) Size dependent ToF distributions for R700 starting from a small sample size ($L = 0.69$ mm) going down to very thin sample sizes ($L = 0.21$ mm). The diffusive fit (solid gray line) does not match at long times. Black lines (guide to the eye) are shown to emphasize the exponential behavior. The incident wavelength is 590 nm for all measurements.

deviations from diffusion with the disorder strength can be explained by a single exponential decay of this fluorescence process. We reinterpret previously published data with the help of a diffusion model including this fluorescence lifetime process (section 5). These experiments show that a weak fluorescent signal in some of our 'white paint' materials was misinterpreted as a signature of strong light localization.

2. Methods

Time delayed photons, i.e. photons that spend more time inside a multiple scattering medium than expected for classical diffusion, have previously been used to look for light localization [4, 5]. Our light source is a femtosecond pulsed laser system tunable between 550 and 650 nm (further described in [5]). On the detection side, we use a photo multiplier (HPM-100-40, Becker & Hickl GmbH) for ToF measurements [29, 30] and an ultra fast gateable camera system (Picostar, LaVision) for TP measurements [5, 31].

Our samples are 'white' powders made of TiO_2 nano-particles ($n_{\text{anatase}} \approx 2.5$ and $n_{\text{rutile}} \approx 2.7$ [32]). The high refractive index of the rutile phase and the low absorption in the used wavelength range make them an ideal material for scattering experiments. These samples are commercially available powders from DuPont and Sigma-Aldrich, characterized in detail in [30, 31, 33, 34]. Deviations from classical diffusion have been observed for three powders from DuPont in the rutile phase (R700, R902 and R104) [5]. For samples with a typical filling fraction of 50%, these white powders have an inverse turbidity kl^* of 2.8, 3.4 and 3.7 [31], where kl^* is defined as the product of the wave vector k and the transport mean free path l^*. Their polydispersities range between 25–45% with a mean diameter varying from 233 to 273 nm. Anatase as well as rutile powders from Sigma-Aldrich (respectively AA and AR) with $kl^* = 6.4$ and 5.2 did not show any deviation from the diffusive behavior [26, 35] and are therefore used as diffusive reference samples (see figure 1(a)). AA has a mean particle size of 170 nm with 47% polydispersity and AR has a mean particle size of 540 nm with 37% polydispersity [31].

3. Questioning the localization interpretation

3.1. Samples thinner than the previously inferred localization length

The theory of Anderson localization predicts the waves to be confined to a certain length scale, the localization length ξ. In previous experiments, this length was obtained from TP measurements, finding $\xi_{\text{R700}} = 670\ \mu$m for R700 [5]. It is expected that decreasing the thickness of the slab-shaped samples well below the localization length will lead to a reduction of the localization signatures since large spatial localizing modes should be significantly disturbed by boundary effects. Figure 1 shows ToF distributions of AA and R700 for various thicknesses L.

A series of R700 samples, where the largest sample is just as thick as the earlier evaluated localization length, can be seen in figure 1(b). For comparison, figure 1(a) shows two AA samples. A diffusive fit [35] for the thinnest

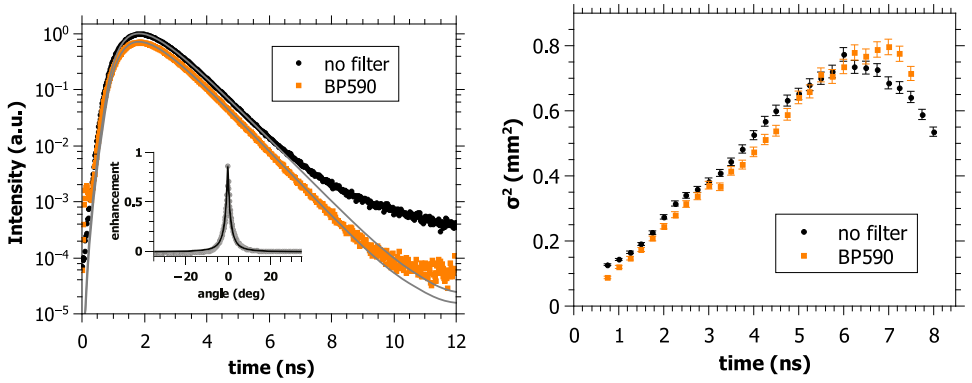

(a) Time of flight: R700 in agarose (b) Transmission profile width: R700 in H_2O

Figure 2. ToF distributions (a) and TP widths (b) for a fixed incident wavelength $\lambda_{inc} = 590$ nm with (orange squares) and without (black dots) bandpass filter set to the incident wavelength (FWHM 10 nm). In (a) a sample ($L = 2.3 \pm 0.1$ mm) of R700 solved in agarose gel was used. The gray lines show diffusion fits for both curves. Inset: backscattering cone used to determine the mean free path ($l^* = 1.0 \pm 0.1$ μm) [36]. In (b) R700 powder was solved in H_2O (ratio 1:1). The profile width was determined following [5].

and the thickest sample of each material is shown (gray lines)[4]. For all R700 samples, even those in the $L < \xi$ regime, a clear deviation from the diffusion theory is present at long times. The photons in the long time tail seem to occur as a second exponential (black lines in figure 1(b)) with a larger time constant. In contrast, all AA and AR samples (data not shown for AR) closely follow the diffusion theory predictions.

3.2. Decreasing the turbidity

In 3D, Anderson localization occurs as a disorder driven phase transition. We quantify the disorder by the turbidity $(kl^*)^{-1}$ as obtained from the width of coherent backscattering cone. A sensitive test to check whether the long time tail originates from a second process different from localization is to strongly decrease the disorder (increase kl^*). In previous experiments the turbidity was varied by using different powders [4] and by changing the incident wavelength [5, 29]. Here, we expand the accessible range of kl^* by lowering the refractive index contrast between the particles (refractive index of $n \approx 2.7$ [32]) and the surrounding medium, increasing thus the transport mean free path l^*, by replacing air ($n = 1$) by agarose gel ($n \approx 1.33$) as a surrounding medium.

Figure 2(a) shows a ToF distribution (no filter, black curve) of R700 surrounded by agarose gel. Coherent backscattering [36, 37] was used to quantify $kl^* \approx 10$. Measuring the same sample with a 590 nm bandpass filter (10 nm FWHM; BP590, orange squares in figure 2(a)), as described in [29], allows us to probe the light transmitted at the incident wavelength. Diffusive fits for both measurements are plotted in gray. The ToF with filter follows the expected distribution for diffusive transport [35] better than the non-filtered one which shows a much more pronounced upturn for the long time tail. Thus this long time tail must have been wavelength shifted, and is unlikely to be caused by localization since $kl^* \approx 10$ should be far in the diffusive regime. The same measurement was also performed with water or glycerol as surrounding medium, leading to the same result.

Similarly, signs of localization are tested with the TP method [5] by suspending R700 in water and evaluating the transmission profile width with and without the 590 nm bandpass filter (see figure 2(b)). The width of the transmitted profile should show a linear increase for a diffusive sample [38]. The data without filter (black dots) show a deviation from the linear diffusive increase of the width at long times. This deviation occurs similar to the one observed in [5], but in a higher kl^* regime. The same results were obtained for the TP with glycerol as surrounding medium. Note that in both ToF and TP with a bandpass filter, deviations from classical diffusion can be observed [29]. However, the filter has a FWHM bandwidth of 10 nm and thus some wavelength shifted light can still pass to the detector.

In conclusion, measuring ToFs and TPs, we observed wavelength shifted photons leading to kinks at long times, which were earlier interpreted as localization signatures. These observations are now present in a regime of low turbidity where no localization effects are expected.

[4] The noise in the fit-curves is due to the convolution of the theory-function with a measured laser reference pulse [29].

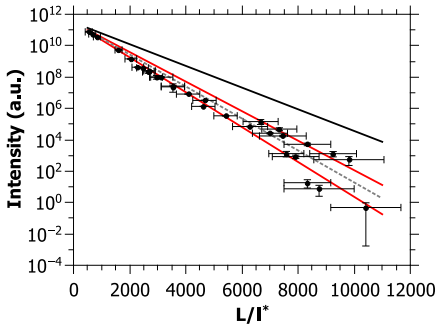

Figure 3. Total transmission of a R700 sample as a function of sample thickness L normalized to l^*. Same data as in [27]. The gray dotted line shows an exponential according to the absorption length $L_a = 106.5\ \mu$m with an error of $\pm 8.8\ \mu$m (red lines) obtained by diffusion fits to the ToF data of figure 7(a). The absorption decay can explain the data, without assuming localization effects. The black line shows an exponential according to $L_a = 157\ \mu$m, as obtained in [26].

3.3. Static transmission data

In diffusive ($kl^* \gg 1$), sufficiently thick ($L \gg l^*$) and absorbing slabs, the transmission scales with $\exp(-L/L_a)$, with L_a the macroscopic absorption length. In contrast, in the localization regime the total transmission is dominated by the localization length and is proportional to $\exp(-L/\xi)$ on top of absorption [19]. In early experiments, indications of localization were found in static transmission measurements performed on slabs of R700 [26, 27]. The static transmission data could not be explained by absorption only. Deviations were found to be in accord with the inferred localization length extracted from localization fits ([35], equation (2) in [26]).

At this time the absorption length was obtained as a result of this localization fit on the ToF distributions, and gave a result of $L_a = 157\ \mu$m ([26], see black line in figure 3). Extracting the absorption length by fitting only the diffusive part of R700 ToF distributions by diffusion theory yields a smaller average absorption length of $L_a = 106.5 \pm 8.8\ \mu$m than the one obtained by the localization fit[5]. This new absorption length value allows us to re-interpret the static transmission data of [26, 27]. The exponential decay is now explainable by absorption alone (gray dotted line in figure 3).

Similarly, earlier claims of light localization in 3D by Wiersma *et al* in the transmission coefficient [12] could also be explained by absorption [19, 21]. The same exponential signatures of localized light and absorbed light in static transmission data make it very difficult to distinguish these effects and should be handled with care. A clear data analysis can only be guaranteed by an absorption-free time-resolved method such as the transmission profile width measurements from Sperling *et al* [5]. However figure 2(b) questions the interpretation of these data.

4. Signs of a weak fluorescent signal

We showed in figure 2(a) a first crude spectral analysis of the ToF distribution for a sample consisting of R700 embedded in agarose. This measurement indicates that the deviation in the long time tail originates from wavelength shifted photons with respect to the incident value $\lambda_{inc} = 590$ nm. In figure 4 we further investigate the spectral shift of the photons in the long time tail.

ToFs of a pure R700 sample were measured using different filters, similarly to measurements performed in [29]. The distribution with no filter between the sample and the detector (black dots) shows a strong upturn of the long time tail. A measurement with a bandpass filter around 590 nm reveals that the non-wavelength shifted light propagates through the sample diffusively[6] (orange squares). A measurement with a shortpass filter blocking all photons above 600 nm (blue down triangle) highlights that the long time tail is dominated by red shifted light: the long time tail is blocked by the SP600 filter. The ToF using a longpass filter for wavelengths above 550 nm (red up triangle) nearly matches the measurement with no filter, strengthening the observation of a signal in the red shifted region[7].

[5] Despite better data evaluation, we now use a diffusion fit instead of a localization fit. It turned out that the diffusion fit results in reliable absorption times for all samples of one powder, whereas the localization fit did match the data poorly and produced scattered (and quite different) absorption times.

[6] Up to the small effect in the late time due to the finite width of the BP590 which was already discussed in section 3.2.

[7] These observations are in contrast to earlier observations published in [27], in which a problem with the used filter can not be excluded.

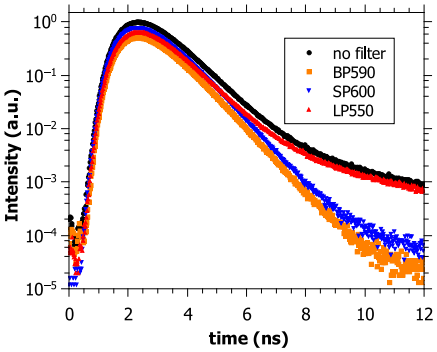

Figure 4. ToF distribution of a R700 sample ($L = 0.83$ mm) measured without filter (no filter), a bandpass filter around 590 nm (BP590), a shortpass filter 600 nm (SP600) and a longpass filter above 550 nm (LP550) with an incident wavelength $\lambda_{inc} = 590$ nm. The red shifted photons show a long time tail, indicating a fluorescence while the blue shifted and non-shifted light behaves purely diffusively.

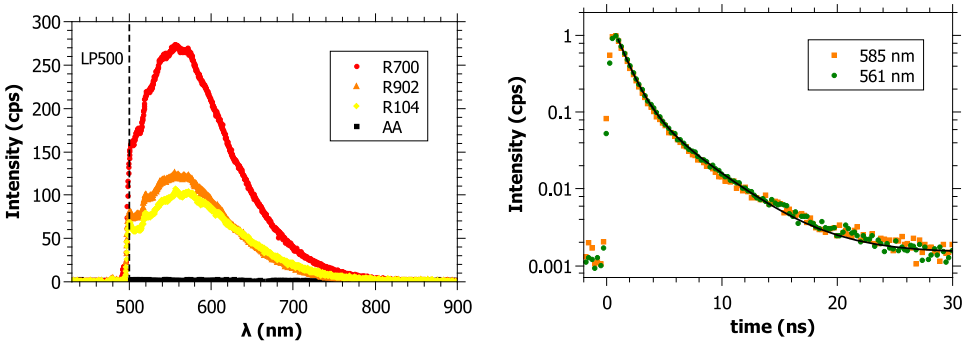

(a) Emission spectra (b) Lifetime measurements of R700

Figure 5. (a) Emission spectra of R700 (red dots), R902 (orange triangles), R104 (yellow diamonds) and AA (black squares) with $\lambda_{inc} = 485$ nm using a long pass 500 nm filter and a laser power of $P = 50$ μW. (b) Lifetime measurements for two different incident wavelengths (585 nm (orange squares) and 561 nm (green dots)). The corresponding bi-exponential fit is shown as black line. The first exponent corresponds to the electronic setup response and can be ignored.

In the spectral study shown in figure 4, all the photons in the long time tail occur as red shifted light. In figure 2(a) the long time tail occurs for wavelength shifted photons in a low scattering regime. An exponential behavior of the long time tail in ToF distributions for very thin samples is observed in figure 1(b). All together, these observations suggest that localization claims do not hold anymore and that a lifetime process, such as fluorescence, is most likely the source of these photons.

Thus, in order to quantify the origin of the long time tail in the ToF and the kink in the TP measurements we search for a fluorescent signal in the visible region. The white powders are therefore spectrally analyzed in a sensitive micro-luminescence microscope setup, further described in [39]. The light source is a widely tunable pulsed ps-laser system and the detector is an EMCCD[8] placed behind a monochromator grating. In all samples that were previously claimed to localize (R700, R902, R104) a weak fluorescent signal is observed with a broad emission in the visible range. The photo luminescence (PL) spectra of R700, R902, R104 and AA are shown in figure 5(a). All samples are excited at $\lambda_{inc} = 485$ nm with a laser power of $P = 50$ μW. A 500 nm longpass filter was used to filter the scattered laser light. R700 shows the strongest signal followed by R902 and R104. For AA no fluorescent signal within the sensitivity of the setup is observed. This relative intensity dependency follows the material dependent kl^*—scaling of the observed deviations from diffusion in [4, 5, 30, 31, 33]. No fluorescent signal was detected for a rutile phase powder from Aldrich (data not shown), excluding the rutile phase to be the origin of the deviations from diffusion.

[8] Electron multiplying charge-coupled device.

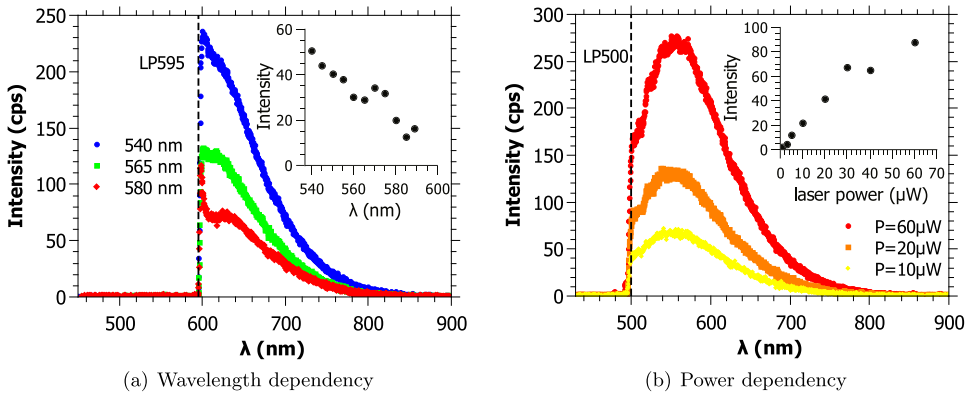

Figure 6. (a) PL spectra for three incident wavelengths (540 nm (blue dots), 565 nm (green squares) and 580 nm (red diamonds)) are shown using a longpass 595 nm filter. Inset: integrated PLE spectra for λ_{inc} between 540 and 590 nm (arbitrary unit). (b) PL spectra for three laser powers (60 μW (red dots) 20 μW (orange squares) and 10 μW (yellow diamonds)) with $\lambda_{inc} = 485$ nm using a longpass 500 nm filter. Inset: integrated PLE spectrum for laser power between 1 and 60 μW.

Measurements of the fluorescent lifetime of the samples were possible with a Hanbury–Brown–Twiss experiment followed by an avalanche photodiode (see [39]). An average lifetime of $\tau_L = 3.85 \pm 0.07$ ns was extracted from exponential fits to lifetime measurements for two incident wavelengths $\lambda_{inc} = 585$ nm and $\lambda_{inc} = 561$ nm (see figure 5(b)).

In [29] an increase of the long time tail for shorter wavelength was observed, explained by the wavelength dependency of kl^*. Figure 6(a) shows PL spectra of R700 for three different incident wavelengths. For shorter wavelength, the PL spectra increase as can be seen in the inset of figure 6(a) in a range from 540 to 590 nm. This measurement explains the increase of the long time tail in ToF distributions and stronger deviations for TPs with decreasing wavelength without assuming localization effects.

The power dependent study of the fluorescence of R700 in figure 6(b) shows an increase with increasing incident power. The inset of figure 6(b) shows the power dependent integrated intensity. A slight saturation is observed as expected from fluorescence. This is in contrast to the nonlinear power dependent increase of the long time tail in ToF distributions in [29–31], which have found an increase in the long time transmitted intensity with higher power. This might be due to the fact that the ToF was measured in transmission, while the fluorescence spectra were recorded in reflection. A volume of saturation for the fluorescence excitation located near the incident surface, growing with incident intensity, would explain such geometrical difference.

The occurrence of this fluorescence only in powders from DuPont led to the search of impurities in these white paint materials. An elementary analysis showed 0.2% of carbon in R700, which could originate from organic material. In AA and AR no carbon was found, consistent with the absence of a fluorescent signal.

5. A time delaying fluorescent diffusion model

To test whether the measured fluorescent signal suffices to explain our old and new data, we extended the ToF intensity distribution $I(t)$ and the time dependent width of the TP, both known from the diffusion theory [26, 35, 38], by including a fluorescence decay. We assume that there is an absorption rate r_{fl} by which photons traveling through the sample are absorbed. Those photons are re-emitted after a time t_d with a probability density proportional to $\exp(-t_d/\tau_{fl})$, τ_{fl} being the fluorescence lifetime. For a photon that, without fluorescence, takes a time t_{sc} to travel through the sample, this gives a probability density of being delayed by an additional time t_d due to fluorescence of

$$p\left(t_{sc}, t_d\right) = \left(1 - r_{fl}\, t_{sc}\right)\delta\left(t_d\right) + r_{fl}\, t_{sc}\, \frac{\exp\left(-t_d/\tau_{fl}\right)}{\int_0^\infty \exp\left(-t'/\tau_{fl}\right) \mathrm{d}t'}. \quad (1)$$

The first term of the sum takes into account the photons that were not delayed ($t_d = 0$), while the second describes those which participated in a fluorescence event. The absorption rate r_{fl} is sufficiently small that re-absorption of fluorescent photons can be neglected.

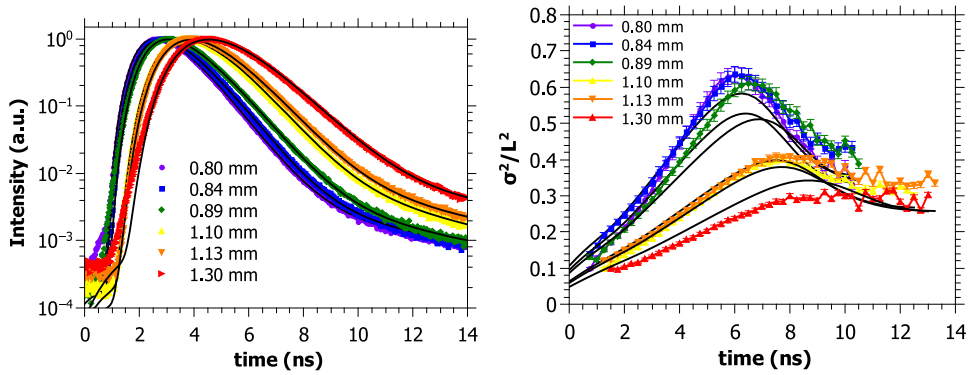

(a) ToF (b) TP

Figure 7. Measured ToF distributions (a) and TP widths (b) of R700 for different sample sizes L. ToF data taken from [31]. TP data taken from [5]. Diffusion fits including fluorescence from equation (2) with fixed $\tau_{fl} = 3.85$ ns are shown as black lines. For each sample size, the corresponding ToF and TP are fitted together, the ToF in log space and the TP in real space. The fit depends only on four fit parameters (r_{fl}, τ_a, D and an offset to compensate the finite size of the illuminating beam in the TP measurements).

Let us recall that $I(t_{sc})$ is the intensity of photons that arrive at time t_{sc} without fluorescence. The intensity $I_{fl}(t)$ for a sample showing fluorescence can now be calculated by integrating $I(t_{sc} = t - t_d)$ over all delay times, weighted by the delay probability density $p(t - t_d, t_d)$ that the photons take an additional time t_d due to fluorescence. This gives a ToF distribution of

$$I_{fl}(t) = \int_0^t I\left(t - t_d\right) p\left(t - t_d, t_d\right) \mathrm{d}t_d. \tag{2}$$

For the TP width, $I(t)$ in equation (2) needs to be replaced by a position dependent intensity distribution $I(r, t)$ to give a 2D profile $I_{fl}(r, t)$ from which the width can be calculated according to [38]. For fitting, the curves calculated with equation (2) were convoluted with the time dependent detector response function for both the ToF and the TP width data.

In figure 7 ToF and TP measurements of R700 for different sample thickness are shown and fitted (black lines) with the extended diffusion equations that include fluorescence (equation (2)). The corresponding ToF distribution and TP width are always fitted *together* with the same set of parameters. Each dataset was fitted with only four free parameters: the fluorescence rate r_{fl}, the (usual) absorption time τ_a, the diffusion constant D and an offset to compensate the spot size enlargement caused by the finite size of the illuminating beam in the TP measurements. Note that the fluorescence lifetime is not fitted but set to $\tau_{fl} = 3.85$ ns as obtained from lifetime measurements shown in figure 5(b). The second exponential in the ToFs is recovered very well by this decay time. In general a remarkable good agreement with the data is observed. The upturn of the long time tail in the ToF distributions can be explained by the extended theory. We are furthermore able to explain all features of the TP width measurements, in particular the thickness dependent saturation and narrowing at long times, without invoking localization effects (contrary to [5]). The latter appears essentially because photons on relatively short diffusion paths (arriving at the backside of the slab at times $t < \tau_{max}$) contribute mostly to the central part of the TP and thus, their fluorescence signal, which is delayed by the fluorescence lifetime, appears mostly in the central part of the TP. This effect gives rise to the peak in the TP width. The fits give an average fluorescence absorption rate of $r_{fl} = 0.0044 \pm 0.0006\ \mathrm{ns}^{-1}$, an average diffusion constant of $D = 11.9 \pm 0.7\ \mathrm{m}^2\ \mathrm{s}^{-1}$ and an average absorption time of $\tau_a = 0.92 \pm 0.03$ ns.

6. Conclusion

In this article, we present new measurements that show features previously interpreted as signs of Anderson localization [4, 5, 23, 26–29], but in regimes where no localization should occur. ToF measurements of very thin samples ($L < \xi$) still show deviations from diffusion, contrary to an expected transition to pure diffusion in the Anderson localization picture. Furthermore, lowering the turbidity $(kl^*)^{-1}$ by changing the surrounding medium of the scattering particles does not affect the long time tail. This is also unexpected for Anderson localization since kl^* is well above the expected transition value for these samples. We were also able to show that

the static transmission data of [26, 27], previously interpreted as a localization signature, can be actually described with absorption only, further weakening the interpretation of localization.

Besides the aforementioned observed inconsistencies, the deviations from diffusion occurred as a red shifted signal in ToF distributions. Thus we measured PL spectra for all mentioned powders in a fluorescence microscope setup, with the result that all powders earlier claimed to localize (R104, R700, R902) show a weak fluorescence signal in the visible. Probably by chance, the samples with low kl^* (reached either by using different samples or by changing the incident wavelengths) are those where the fluorescence signal is the strongest.

Finally, we performed a calculation based on diffusion theory, but including a lifetime process. This modified theory is able to fit all our data, both ToFs and TPs, with excellent agreement. A measured lifetime of the fluorescence is used in the fits as a fixed parameter and explains the second exponential decay very well.

These results strongly suggest that all deviations from pure diffusion in our 'white paint' powders are caused by a weak fluorescence and do not originate from Anderson localization. Chemical analysis of the powders showed that they additionally contain carbon, implying the fluorescence to originate from organic impurities. However, the exact origin of the fluorescence is still unknown due to the low concentration of the impurities.

In summary, Anderson localization of light in 3D has still not been observed yet, neither in the infrared (reported in [12], questioned in [19] and refuted in [21]) nor in the visible (reported in [4, 5], questioned in [22] and refuted in this article). Although attempts have been made with higher refractive index materials (macroporous GaP—bulk refractive index of 3.3—[13], Ge powder—bulk refractive index of 4—[40]), they all failed to reach the localization transition. Recent theoretical predictions suggest that near field effects could suppress Anderson localization of light in a 3D ensemble of point scatterers [41]. Furthermore, recent numerical simulations and experimental data explored the effect of near field coupling between Mie scatterers on the transport properties of light, so far only in the diffusive regime [42].

Is this the end of 3D Anderson localization of light? The present reasonable answer is no: it has just not been observed yet. The quest should continue with high index 'white paint' samples, getting rid of any fluorescent signal, and by increasing the scattering strength to currently unreached low kl^* values (either in the visible or in the IR). This might be achieved by lowering the polydispersity and thus tuning the scattering to Mie-resonances in monodisperse materials.

Acknowledgments

We acknowledge support by the Deutsche Forschungsgemeinschaft (DFG), the Center for Applied Photonics (CAP), University of Konstanz and the Schweizerischer Nationalfonds (SNF). We thank the AG Leitenstorfer, and especially Denis V Seletskiy and Florian Werschler for their most helpful cooperation regarding the PL spectra study. We are grateful to Mengdi Chen for the elementary analysis of our powders. We further acknowledge measurements and helpful discussions with Wolfgang Bührer.

References

[1] Anderson P W 1958 *Phys. Rev.* **109** 1492–505
[2] Abrahams E, Anderson P W, Licciardello D C and Ramakrishnan T V 1979 *Phys. Rev. Lett.* **42** 673–6
[3] Anderson P W 1985 *Phil. Mag.* B **52** 505–9
[4] Störzer M, Gross P, Aegerter C M and Maret G 2006 *Phys. Rev. Lett.* **96** 063904
[5] Sperling T, Bührer W, Aegerter C M and Maret G 2013 *Nat. Photonics* **7** 48–52
[6] Anderson P W 1972 *Science* **177** 393–6
[7] Lagendijk A, van Tiggelen B A and Wiersma D S 2009 *Phys. Today* **62** 24
[8] Thouless D J 1974 *Phys. Rep.* **13** 93–142
[9] van Tiggelen B A, Lagendijk A and Wiersma D S 2000 *Phys. Rev. Lett.* **84** 4333–6
[10] Skipetrov S E and van Tiggelen B A 2006 *Phys. Rev. Lett.* **96** 043902
[11] Vollhardt D and Wölfle P 1980 *Phys. Rev.* B **22** 4666–79
[12] Wiersma D S, Bartolini P, Lagendijk A and Righini R 1997 *Nature* **390** 671–3
[13] Schuurmans F J P, Megens M, Vanmaekelbergh D and Lagendijk A 1999 *Phys. Rev. Lett.* **83** 2183
[14] Hu H, Strybulevych A, Page J H, Skipetrov S and van Tiggelen B 2008 *Nat. Phys.* **4** 945–8
[15] Kondov S S, McGehee W R, Zirbel J J and DeMarco B 2011 *Science* **334** 66–8
[16] Jendrzejewski F, Bernard A, Müller K, Cheinet P, Josse V, Piraud M, Pezzé L, Sanchez-Palencia L, Aspect A and Bouyer P 2012 *Nat. Phys.* **8** 398–403
[17] McGehee W R, Kondov S S, Xu W, Zirbel J J and DeMarco B 2013 *Phys. Rev. Lett.* **111** 145303
[18] Semeghini G, Landini M, Castilho P, Roy S, Spagnolli G, Trenkwalder A, Fattori M, Inguscio M and Modugno G 2015 *Nat. Phys.* **11** 554–9
[19] Scheffold F, Lenke R, Tweer R and Maret G 1999 *Nature* **398** 206–7
[20] Wiersma D S, Rivas J G, Bartolini P, Lagendijk A and Righini R 1999 *Nature* **398** 207
[21] van der Beek T, Barthelemy P, Johnson P M, Wiersma D S and Lagendijk A 2012 *Phys. Rev.* B **85** 115401
[22] Scheffold F and Wiersma D 2013 *Nat. Photonics* **7** 934
[23] Maret G, Sperling T, Bührer W, Lubatsch A, Frank R and Aegerter C M 2013 *Nat. Photonics* **7** 934–5

[24] Müller C A and Shapiro B 2014 *Phys. Rev. Lett.* **113** 099601
[25] McGehee W R, Kondov S S, Xu W, Zirbel J J and DeMarco B 2014 *Phys. Rev. Lett.* **113** 099602
[26] Aegerter C M, Störzer M and Maret G 2006 *Europhys. Lett.* **75** 562–8
[27] Aegerter C M, Störzer M, Fiebig S, Bührer W and Maret G 2007 *J. Opt. Soc. Am.* A **24** A23–7
[28] Aegerter C M, Störzer M, Bührer W, Fiebig S and Maret G 2007 *J. Mod. Opt.* **54** 2667–77
[29] Sperling T, Bührer W, Ackermann M, Aegerter C M and Maret G 2014 *New J. Phys.* **16** 112001
[30] Bührer W 2012 Anderson localization of light in the presence of nonlinear effects *PhD Thesis* Universität Konstanz (http://nbn-resolving.de/urn:nbn:de:bsz:352-207872)
[31] Sperling T 2015 The experimental search for Anderson localisation of light in three-dimensions *PhD Thesis* Universität Konstanz (http://nbn-resolving.de/urn:nbn:de:bsz:352-0-300030)
[32] Shannon R D, Shannon R C, Medenbach O and Fischer R X 2002 *J. Phys. Chem. Ref. Data* **31** 931–70
[33] Störzer M 2006 Anderson localization of light *PhD Thesis* Universität Konstanz (http://nbn-resolving.de/urn:nbn:de:bsz:352-opus-22027)
[34] Fiebig S 2010 Coherent backscattering from multiple scattering systems *PhD Thesis* Universität Konstanz (http://nbn-resolving.de/urn:nbn:de:bsz:352-opus-123390)
[35] Berkovits R and Kaveh M 1990 *J. Phys.: Condens. Matter* **2** 307–21
[36] Gross P, Störzer M, Fiebig S, Clausen M, Maret G and Aegerter C M 2007 *Rev. Sci. Instrum.* **78** 033105
[37] Fiebig S, Aegerter C M, Bührer W, Störzer M, Akkermans E, Montambaux G and Maret G 2008 *Europhys. Lett.* **81** 64004
[38] Cherroret N, Skipetrov S E and van Tiggelen B A 2010 *Phys. Rev.* E **82** 056603
[39] Beha K, Batalov A, Manson N B, Bratschitsch R and Leitenstorfer A 2012 *Phys. Rev. Lett.* **109** 097404
[40] Rivas J G, Sprik R, Lagendijk A, Noordam L D and Rella C W 2001 *Phys. Rev.* E **63** 046613
[41] Skipetrov S E and Sokolov I M 2014 *Phys. Rev. Lett.* **112** 023905
[42] Naraghi R R, Sukhov S, Saenz J J and Dogariu A 2015 *Phys. Rev. Lett.* **115** 203903

New Journal of Physics
The open access journal at the forefront of physics
Deutsche Physikalische Gesellschaft DPG | IOP Institute of Physics

Fast Track Communication

Probing Anderson localization of light by weak nonlinear effects

T Sperling[1], W Bührer[1], M Ackermann[2], C M Aegerter[2] and G Maret[1]
[1] Fachbereich Physik, Universität Konstanz, 78457 Konstanz, Germany
[2] Physik-Institut, Universität Zürich, Winterthurerstr. 190, 8057 Zürich, Switzerland
E-mail: Georg.Maret@Uni-Konstanz.de

Received 2 July 2014, revised 2 October 2014
Accepted for publication 20 October 2014
Published 31 October 2014
New Journal of Physics **16** (2014) 112001
doi:10.1088/1367-2630/16/11/112001

Abstract
Breakdown of wave transport due to strong disorder is a universal phenomenon known as Anderson localization (AL). It occurs because of the macroscopic population of reciprocal multiple scattering paths, which in three dimensional systems happens at a critical scattering strength. Intensities on these random loops should thus be highly increased relative to those of a diffusive sample. In order to highlight localized modes of light, we exploit the optical nonlinearities of TiO_2. Power dependent and spectrally resolved time of flight distribution measurements in transmission through slabs of TiO_2 powders at various turbidities reveal that mostly long loops are affected by nonlinearities and that the deviations from diffusive transport observed at long times are due to these localized modes. Our data are a first step in the experimental investigation of the interplay between nonlinear effects and AL in 3D.

Keywords: Anderson localization, nonlinear optics, multiple light scattering

1. Introduction

Anderson localization (AL) of quantum mechanical waves such as electrons in atomic lattices containing impurities was predicted more than 50 years ago [1] to account for the metal–

insulator transition [2] observed at finite impurity densities. The analogous phenomenon of AL of classical waves such as light has been intensively studied since the mid 80s [3–6]. These studies underlined the fundamental nature of AL which originates from constructive interference of waves scattered along multiple scattering paths corresponding to localized modes, a phenomenon that should occur for any wave scattered in any sufficiently disordered medium. Quantum and classical localization essentially always take place for 1D and 2D systems [7] as demonstrated experimentally e.g. for microwaves [8, 9], light [10, 11] and cold atoms [12, 13]. In 3D, AL is physically more intriguing, but also more challenging to observe. This is due to the fact that 3D localization occurs only above a critical scattering strength [7, 14] which may be difficult to reach experimentally depending on the nature of the wave and the scattering material. In addition, the experimental observation of localized classical waves may also be obscured by several artifacts. For instance absorption in the bulk can easily lead to experimental signatures similar to AL [15, 16] and settling questions concerning such artifacts requires long and careful studies [17]. Other factors include leakage through the sample boundaries [18] or resonant scattering [19, 20]. So far, experimental evidence for 3D AL excluding these systematics has been obtained for visible light [21, 22], ultrasound [23] and ultracold atoms [24–26].

A careful quantitative study of bulk localizing samples is required to test simultaneously several long-standing key predictions concerning localized states and the localization transition [7]. On the one hand, this entails the observation of a slow-down of diffusion, using time-resolved measurements, by probing either the total transmission or spatially resolved intensity profiles. This has been achieved recently for sound waves [23] and visible light [21, 22], where the spatially resolved measures are such that the influence of absorption can be fully neglected [27]. In the optical 3D localization experiment, this allowed for a direct determination of the localization length which revealed its scaling with the samples' turbidity and provided a clear signature of the localization transition [22]. In addition, the shape of the spatial intensity distribution shows an exponential rather than a Gaussian profile, as predicted [10, 24], see supplementary material of [22]. On the other hand, one expects a great increase in the fluctuations of transmitted intensities of single speckles, because of a strong overpopulation of localized modes [11, 28], visible e.g. in a skewed (non-Rayleigh) intensity distribution, which have been observed in 3D experiments on ultrasound [23], but are only fully described for quasi 1D systems [29, 30].

In this work we take advantage of the nonlinear optical response of titania particles as scatterers to emphasize intensity dependent effects. The interplay between AL and nonlinear effects (NL) is a field of growing theoretical interest [31–33], but NL-experiments were reported so far only for a few 2D systems [6, 10, 11, 34]. One may anticipate that the positive Kerr nonlinearity of TiO_2 [35–37] is significantly excited by the contribution of macroscopically populated localized modes, with a noticeable influence on the detected time of flight signals (TOF) from 3D slabs. This is analogous to the recent second harmonic study on AL in ZnO nanorod mats [11] and to random lasing from closed recurrent scattering loops in 3D [28]. In this work we use the frequency shifts incurred by these nonlinear effects in combination with stimulated Raman scattering [37] to highlight localized modes. Note that due to the macroscopic population of these modes above a critical turbidity, we expect a qualitative difference in the excitation of nonlinear effects as a function of turbidity, analogous to the strong Raman laser emission observed above threshold in multiply scattering $BaSO_4$ powders [38].

New J. Phys. **16** (2014) 112001 Fast Track Communications

Measuring wavelength-resolved TOF distributions in transmission we find increased non-exponential long time tails at wavelengths above and below the incident wavelength. The latter blue shifted signals exclude simple fluorescence contributions. Consistent with our non-frequency resolved earlier data [21, 22] the deviations from classical TOF scale with turbidity $(kl^*)^{-1}$ as is expected for AL transition. Here, k denotes the wavevector and l^* the transport mean free path. The values of the localization lengths thus obtained quantitatively agree with those from measurements of the time dependent spatial intensity profiles [22] over the entire kl^*-range covered. The experimental study reported here thus complements our earlier non-wavelength-resolved results to study intensity distributions in our samples and is consistent with the observation of optical AL modes in 3D samples at elevated turbidities ($2.4 < kl^* < 5$) [39, 40]. Note that the value of the critical turbidity in this case is consistent with the Ioffe-Regel criterion which estimates a kl^* of order unity for the transition to occur. However, there are no numerically accurate predictions for the value of the critical turbidity.

2. Methods

In order to be able to see the slow-down of the light diffusion we use a pulsed laser system consisting of a frequency doubled Nd:YVO_4-laser with output power of 18 W pumping a Titanium–Sapphire oscillator, which subsequently pumps a frequency doubled OPO. We get a pulsed output of 1 W at 590 nm with a repetition rate of 76 MHz and a pulse duration of ≈250 fs. Furthermore, the central wavelength of the pulses can be tuned between 550 and 650 nm. We reduce the repetition rate with a pulse picker to be able to take data for time intervals longer than the repetition time of 13.2 ns. We operate the TOF measuring card (by B&H) at a total scan time of typically 20 ns with 1024 channels time resolution. The detector used was a hybrid photo multiplier HPM-100-40 (from B&H) avoiding the typical after-pulsing in standard photomultipliers thus increasing the time resolution. The samples consist of TiO_2 nanoparticles with a particle diameter ranging between 170 and 245 nm and polydispersities between 25 and 45%, which are commercially available from DuPont. The TiO_2 particles are in the rutile crystal structure for samples R700 (diameter 245 nm, polydispersity 45%) and R104 (diameter 230 nm, polydispersity 25%), which has a refractive index of 2.7. In one of our samples, a one-to-one mixture of anatase (refractive index 2.5, diameter 170 nm, polydispersity 45%) and rutile (R104 sample) nanoparticles was made (R104AA) in order to decrease the turbidity. Since the intensity of the light transmitted through the sample is very low typical spectral resolution techniques like interference spectrometers would either imply very long measurement times, thereby drastically reducing the signal-to-noise ratio, or they would fail because of the insufficient intensity. Therefore, instead, we use a set of interference band pass filters with bandwidths of 10 nm around a central wavelength indicated in figure 2 positioned between the sample and the detector.

3. Power dependent and spectrally resolved time of flight distribution

The nonlinear optical properties of TiO_2 are well known (see e.g. [35–37]). They give rise to significant power dependent spectral broadening as revealed from near infrared transmission measurements on monomode titania waveguides [37], which are mostly due to stimulated Raman scattering providing a nonlinear, as well as inelastic response. In our samples, which

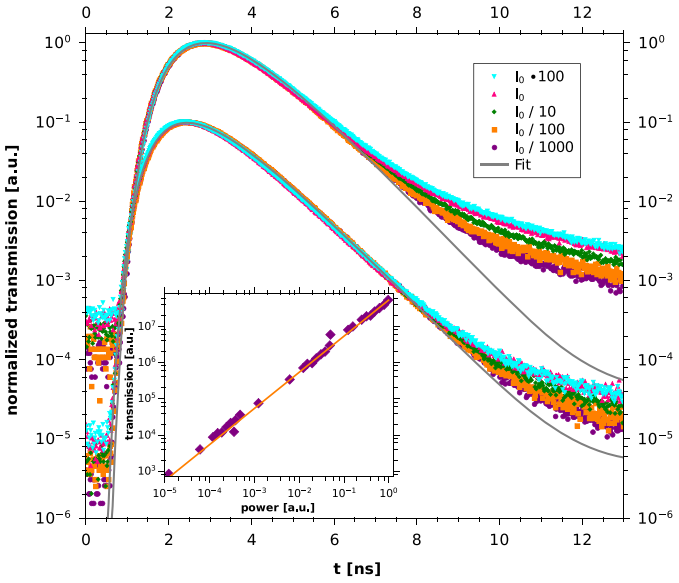

Figure 1. Power dependence of the time resolved and time integrated (inset) optical transmission. Inset: total transmission for sample R700 with $kl^* = 2.7$, $L = 1.25$ mm. Time resolved transmission[5] for (top) sample R700 with $kl^* = 2.7$, $L = 0.93$ mm, (bottom) sample R104AA with $kl^* = 5.7$, $L = 1.00$ mm at different incident intensities with $I_0 \approx 1$ GWm^{-2}. The continuous lines indicate the analytical solution of the classical diffusion equation for a slab with the indicated sample parameters convoluted with time dependent detector response function. The R104AA-data are down-shifted by one decade for clarity.

consist of rather irregularly shaped polydisperse TiO_2-particles (for a picture see [21]) there are no strict symmetry rules for the different NL-effects and hence many of them may occur and mix along the multiple scattering paths. We do expect, however, a power dependent spectral broadening qualitatively similar to [37]. The inset of figure 1 shows the dependence of the total time integrated transmission on the incident laser power for a sample with inverse turbidity $kl^* = 2.7$ (R700, rutile). For all samples discussed here kl^* was obtained from the width of the coherent backscattering cone [41–43]. Within error bars the total transmission increases linearly with incident power indicating that overall, nonlinear effects are rather weak, of order 10^{-5} or less. However, the time resolved data (see footnote 5) shown in figure 1 reveal a clear upturn of the long time tail which increases with increasing power. The upturn at long times is associated with the onset of AL [21] because the deviation from classical diffusion (indicated by the continuous line) strongly increases with increasing turbidity (figure 1 and [21]). Figure 1 shows that the upturn is clearly weaker for the essentially non-localizing sample R104AA than for the localizing sample R700. Both the long time intensity upturn at fixed incident power and its power dependence become weaker with increasing kl^*, i.e. when moving away from the AL-transition. When the incident power is varied by five orders of magnitude, the intensity of the long-time tail is enhanced by less than a factor of three for both samples. This shows that while nonlinear effects are significant, they are weak. They manifest themselves primarily in the long time upturn, or slowing down of the decay, in TOF which was associated with AL [21]. While

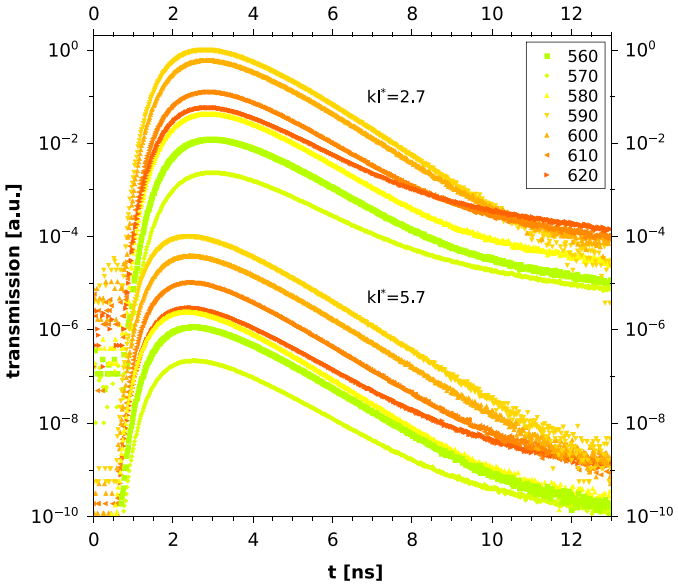

Figure 2. Time of flight distributions for fixed incident wavelength $\lambda_{\rm inc} = 590$ nm ($I_0 \approx 1$ GW m^{-2}) at different detected spectral shifts as indicated by the central wavelength of the bandpass filter $\lambda_{\rm BP}$ for sample R700, ($kl^* = 2.7$, $L = 0.93$ mm) and sample R104AA ($kl^* = 5.7$, $L = 0.94$ mm). The latter data are down-shifted by 4 decades for clarity.

due to the diffusive spreading of the power density through the sample, nonlinear effects are a priori more likely to occur near the front surface, our data imply that they are also more likely within the localized modes in the bulk because of the higher intensity of these modes, consistent with [11]. NL effects can thus be used to enhance signatures of high intensity transmission modes in TOF more clearly. This is particularly important because in our samples the overall fraction of photons in the upturn, i.e. 'delayed' by AL is very small compared to the classically diffusing photons, even for high turbidities. In order to connect these high intensity transmission modes with AL in 3D systems, it is important to study the turbidity dependence, where these modes should only appear above a critical turbidity. This turbidity dependence is discussed in detail below.

We now turn to the spectrally resolved data. Figure 2 shows results of TOF measurements for a sample with rather modest turbidity ($kl^* = 5.7$) compared to one with high turbidity ($kl^* = 2.7$) taken at fixed incident wavelength $\lambda = 590$ nm, fixed incident power $I_0 \approx 1$GW m^{-2} and different spectral shifts indicated by the center wavelength $\lambda_{\rm BP}$ of the band pass filter inserted between sample and detector. Given that these are data at a fixed incident intensity, we here mainly probe inelastic component, which we associate with the nonlinear stimulated

[5] TOF data shown here correspond to raw transmission counts for a time span determined to reach 65536 counts in the highest bin. They are not deconvoluted with respect to the laser pulse dark count levels and temporal response of detector.

Raman scattering [37]. Contributions from direct coupling to e.g. phonons, while unlikely given the intensity dependent measurements of figure 1, can not be excluded in these data.

The TOF data shown were corrected for the different optical densities of the band pass filters at the central wavelengths and the detector dark noise subtracted so that they show the relative wavelength dependent transmission[3]. In both samples the overall transmission is highest at the incident wavelength and the spectrally shifted intensities rapidly decrease with increasing frequency shift away from λ. This illustrates that the major part of the transmitted light has undergone elastic scattering and classical diffusion, even for $kl^* = 2.7$. In the less turbid sample the shape of the TOF signal does not significantly depend on the detected frequency and essentially agrees with classical photon diffusion (see figure 3). However, from figure 2 it is evident that the more turbid (localizing) sample shows much higher upturns at long times relative to the transmission peak than the less turbid (non-localizing) sample. This can also be seen when looking only at the elastically scattered light, which is separately shown for clarity in figure 3. The relative upturn increases with increasing frequency shift rather independent on the sign of the shift which basically excludes simple fluorescence contributions. Note also that the observed spectral broadenings are qualitatively consistent with the power dependent nonlinearities and stimulated Raman scattering reported for titania waveguides [37]. While a quantitative account of the observed frequency shift in terms of nonlinear processes remains a challenging issue for our granular powders, the fact that the frequency shifted nonlinear upturn increases strongly with decreasing kl^* indicates that above a critical turbidity, long-lived modes are more highly populated, exciting nonlinear effects more strongly. This is consistent with a picture of AL, where after the transition to localization AL-modes are strongly populated [44], which have a relatively increased intensity, as has been found in [23]. These high intensity modes can then more strongly excite e.g. stimulated Raman scattering leading to a strong increase in frequency shifted TOF contributions.

It should be noted that figure 2 also shows that the inelastic contribution does *not* exceed the elastic contribution, as was claimed recently to argue against a signature of localization in the saturation of the width of the photon distribution at long times [39]. Therefore, this direct sign of AL can still be observed when only studying the non-frequency shifted part, shown in figure 3. In addition, the figure shows the elastic contribution of the temporal increase of the width of the photon distribution as determined in [22], where a clear saturation can be seen [40]. This shows that the late time modes are spatially localized even in the elastic case. Considering the TOF data in figure 2, one can see that the strong classically scattered light, which is diffusing as well as absorbed, overrides and therefore hides the long time tail when the bandpass filter is set close to the incident wavelength. Here it is important to note that absorption still plays a role in TOF measurements and this absorption can dominate the decay modes. However, when selecting the inelastic contribution by frequency shifted detection, this diffusing and absorbing part is largely suppressed[4] thus highlighting the long time tail due to AL, which is directly seen in the spatially resolved measurements, where absorption is canceled out of the experiment.

[3] The wavelength dependence of the photo multiplier can be neglected.

[4] The leakage of the elastically scattered light at $\lambda = 590$ nm through the different band pass filters is quantified by their optical density BP560 nm (4.1), BP570 nm (4.4), BP580 nm (2.3), BP590 nm (0.4), BP600 nm (1.1), BP610 nm (2.8) , BP620 nm (4.1)

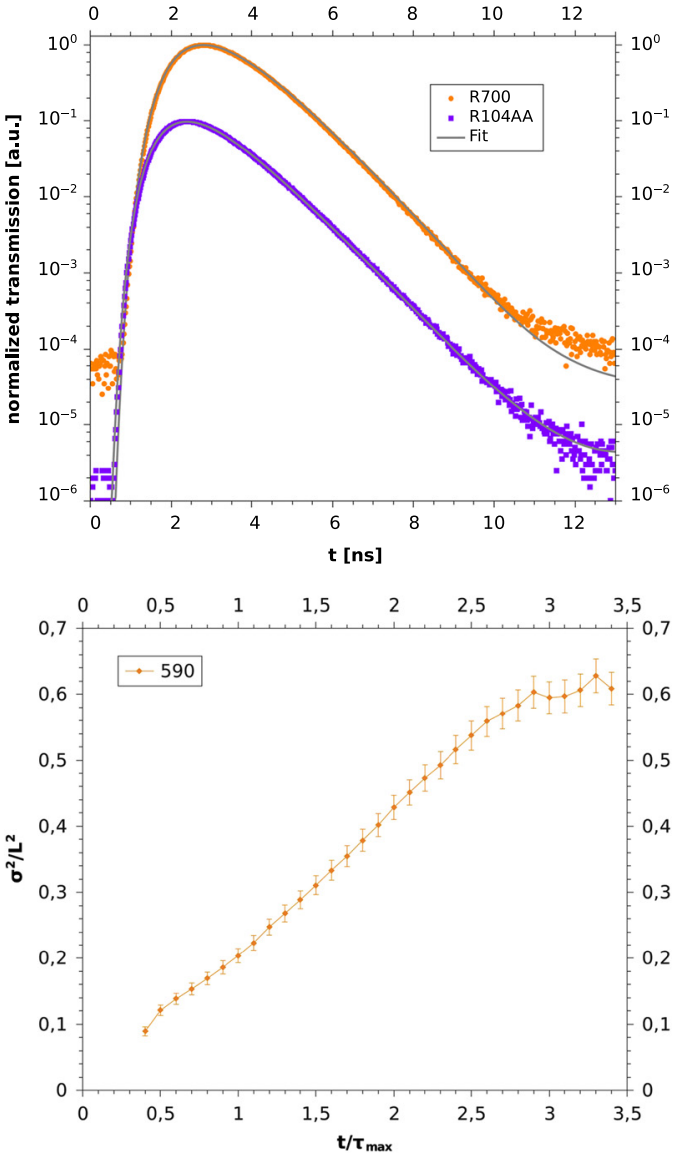

Figure 3. (a) Time of flight distributions for fixed incident wavelength $\lambda_{\text{inc}} = 590$ nm with bandpass filter set to the incident wavelength. For sample R700, ($kl^* = 2.7$, $L = 0.93$ mm) and sample R104AA ($kl^* = 5.7$, $L = 0.94$ mm). These data are also part of figure 2. Continuous lines like figure 1. (b) The width of the photon distribution as determined in [22], but with an added bandpass filter set to the incident wavelength for R700 ($kl^* = 2.7$, $L = 0.86$ mm).

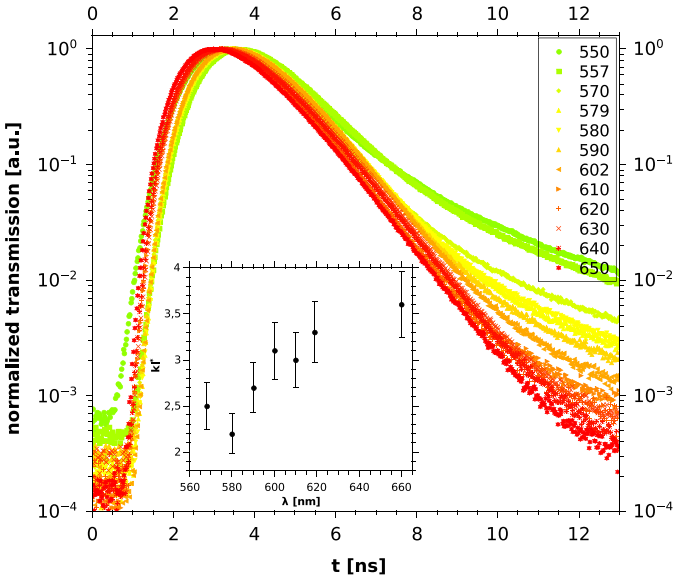

Figure 4. Time of flight distributions for various incident wavelengths λ_{inc} without band pass filter behind the sample. Sample R700, ($kl^* = 2.7$, $L = 0.98$ mm), $I_0 \approx 1$ GW m^{-2}. Inset: wavelength dependence of the inverse turbidity kl^*.

The same conclusion can be drawn from another experiment (figure 4) were we varied the turbidity $1/kl^*$ by varying the incident wavelength for a single given sample (R700). The increase in refractive index of rutile with decreasing wavelength leads to a significant reduction of kl^* from 3.7 to 1.9 (linear interpolation), shown in the inset to figure 4. Note that here we are changing kl^* in a completely independent way from the experiment above, such that effects of sample quality, pressure induced fluorescence, etc can be ruled out. When changing kl^* this way by a factor close to two, the corresponding long time upturn relative to the classical diffusive signal changes by about two orders of magnitude which is spectacular (see figure 5 for the excess signal Ξ (see footnote 6) in the long time tail). At the same time, the photon diffusion constant D_0 merely changes by 50% as directly seen from the small shift of the maximum of the TOF curves and from the data shown in figure 5(a). This comparatively small change of D_0 is consistent with the modest change in kl^*. These observations clearly indicate critical behavior of the upturn in the vicinity of a transition to AL. The kl^*-range of the critical behavior is in quantitative agreement with the observations of spectrally unresolved TOF [45] and the time resolved transmission profiles [22]. Finally, we can look at the spectral shifts of the TOF data for these experiments. This is shown in figure 5(b), where we plot TOF data at three different incident wavelengths, corresponding to three different values of $kl^* = 3.5$, 2.6 and 2.2 with a corresponding spectral filter below the incident wavelength as given in the figure legend. We observe the same trend of a strong increase of the spectral shifts at long times with decreasing kl^*. Note that the data for $kl^* = 2.6$ correspond to one of the curves shown in figure 2 (R700).

Thus, the observations reported here show conclusively that below a critical value of kl^*, long photon paths become increasingly populated. This is shown by the increased frequency shifts at long times, which only appear at low kl^* and at long times, where we varied kl^* in two

New J. Phys. **16** (2014) 112001 Fast Track Communications

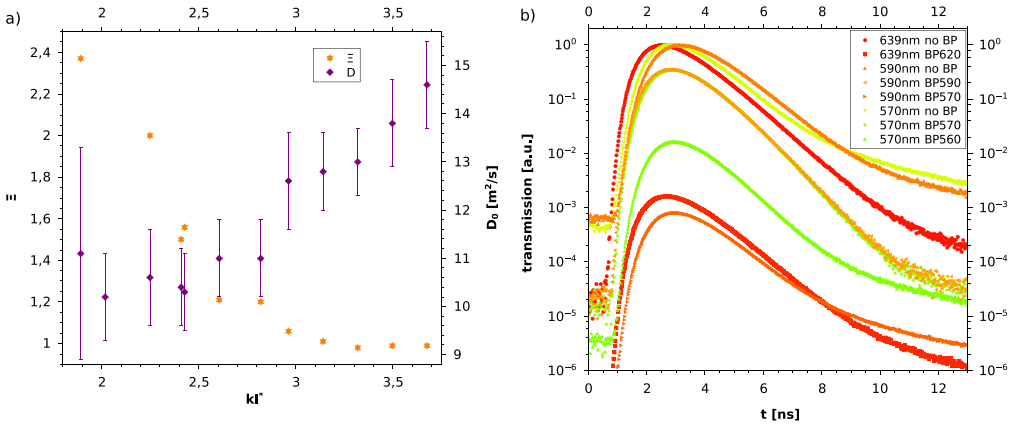

Figure 5. (a) Dependence of the classical photon diffusion constant D_0, as obtained from a fit to classical diffusion, and a quantification Ξ[6] of the excess of photons at long times on the sample turbidity $1/kl^*$. Data are for the sample described in figure 3(b). Time dependence of the spectrally shifted excess for different turbidities. The plot shows TOF distributions for three different experiments determining the spectral shifts corresponding to values of $kl^* = 3.5$ (red), 2.6 (orange) and 2.2 (green). Data are for the sample described in figure 2 (R700).

independent ways with quantitatively comparable results. These results are similar to previous evidence for AL based on the direct determination of the width of the diffusing photon distribution [22]. This, we believe, rules out an alternative interpretation of our data, which would not show a critical turbidity [39, 40].

4. Conclusion

In conclusion we have measured photon time of flight distributions in transmission through optically thick slabs ($L \gg l^*$) of powders of TiO_2 as function of incident power, incident wavelength and detected wavelength. This allowed to vary the turbidity $1/kl^*$ in two independent ways, either by the wavelength dependence of the scattering cross section or by the packing fraction. We find deviations of the time of flight distribution from classical diffusion at long times which show that photons with long transit times spend significantly more time inside the sample than expected from classical diffusion. The number of these 'delayed' photons dramatically increases with increasing turbidity. The scaling of this deviation with the turbidity $1/kl^*$ signals a progressive slowing down of photon diffusion with time at long times consistent with the transition to AL. The nonlinear optical response of TiO_2 provides a significant spectral broadening which, combined with the nonlinear increase of the number of 'delayed' photons with incident laser power, allows to strongly enhance the contributions of localized modes to the TOF signals, thus allowing the use of nonlinearities as a probe for the skewed intensity distribution in localized modes at long times.

[6] The excess of the signal is quantified by the time integral of the ratio of the TOF data and the diffusive fit over a time window of 2 τ_{max} to 3.5 τ_{max} : $\Xi = \int_{2\tau_{max}}^{3.5\tau_{max}} T(t)/T_{fit}(t)\mathrm{d}t$.

While the nonlinear effects as well as the fraction of detected photons from within the localized modes are still small compared to the overall classically diffusing photons in our samples the coupling between the nonlinear effects and AL will be of great interest in the future. For instance, it has been discussed that the critical point of AL changes in nature in the presence of negative nonlinearities [33]. In the case of positive nonlinearities, as is the case in TiO_2, localization may be enhanced [10, 32], which may also explain the fact that in our experiments the critical value of kl^* is somewhat higher than the usually expected value of $kl_c^* = 1$ [14]. This however remains to be studied in future investigations.

Acknowledgements

We acknowledge support by the Deutsche Forschungsgemeinschaft (DFG), the Center for Applied Photonics (CAP), University of Konstanz and the Schweizerischer Nationalfonds (SNF).

References

[1] Anderson P W 1958 *Phys. Rev.* **109** 1492
[2] Imada M, Fujimori A and Tokura Y 1998 *Rev. Mod. Phys.* **70** 1039–263
[3] John S 1984 *Phys. Rev. Lett.* **53** 2169
[4] Anderson P W 1985 *Phil. Mag.* B **52** 505
[5] Lagendijk A, van Tiggelen B and Wiersma D 2009 *Phys. Today* **62** 2429
[6] Segev M, Silberberg Y and Christodoulides D N 2013 *Nat. Photonics* **7** 197
[7] Abrahams E, Anderson P W, Licciardello D and Ramakrishnan T V 1979 *Phys. Rev. Lett.* **42** 673
[8] Genack A and Garcia N 1991 *Phys. Rev. Lett.* **66** 2064
[9] Dalichaouch R, Armstrong J P, Schultz S, Platzman P M and McCall S L 1991 *Nature* **354** 53
[10] Schwartz T, Bartal G, Fishman S and Segev M 2007 *Nature* **446** 52
[11] Maschek M *et al* 2012 *Nat. Photonics* **6** 293
[12] Billy J *et al* 2008 *Nature* **453** 891
[13] Roati G *et al* 2008 *Nature* **453** 895
[14] Ioffe A F and Regel A R 1960 *Prog. Semicond.* **4** 237
[15] Wiersma D S, Bartolini P, Lagendijk A and Righini R 1997 *Nature* **390** 671
[16] Scheffold F, Lenke R, Tweer R and Maret G 1999 *Nature* **398** 206
[17] van der Beek T, Barthelemy P, Johnson P M, Wiersma D S and Lagendijk A 2012 *Phys. Rev.* B **85** 115401
[18] Skipetrov S E and van Tiggelen B A 2006 *Phys. Rev. Lett.* **96** 043902
[19] Drake J M and Genack A Z 1989 *Phys. Rev. Lett.* **63** 259
[20] Lagendijk A and van Tiggelen B A 1996 *Phys. Rep.* **270** 143
[21] Störzer M, Gross P, Aegerter C M and Maret G 2006 *Phys. Rev. Lett.* **96** 063904
[22] Sperling T, Bührer W, Aegerter C M and Maret G 2013 *Nat. Photonics* **7** 48
[23] Hu H, Strybulevych A, Page J H, Skipetrov S E and van Tiggelen B A 2008 *Nat. Phys.* **4** 945
[24] Kondov S S, McGehee W R, Zirbeland J J and DeMarc B 2011 *Science* **334** 66
[25] Jendrzejewski F *et al* 2012 *Nat. Phys.* **8** 398
[26] Semeghini G *et al* 2014 arXiv:1404.3528v1
[27] Cherroret N, Skipetrov S E and van Tiggelen B A 2010 *Phys. Rev.* E **82** 056603
[28] Cao H *et al* 1999 *Phys. Rev. Lett.* **82** 2278
[29] Nieuwenhuizen T M and van Rossum M C 1995 *Phys. Rev. Lett.* **74** 2674
[30] Chabanov A A, Stoytchev M and Genack A Z 2000 *Nature* **404** 850

[31] Fishman S, Krivolapov Y and Soffer A 2012 *Nonlinearity* **25** R53
[32] Conti C 2014 *Chin. Phys. Lett.* **31** 030501
[33] Cherroret N, Vermersch B, Garreau J C and Delande D 2014 *Phys. Rev. Lett.* **112** 170603
[34] Lahini Y *et al* 2008 *Phys. Rev. Lett.* **100** 013906
[35] Adair R, Chase L L and Payne S A 1989 *Phys. Rev.* B **39** 3337
[36] Long H, Chen A, Yang G, Li Y and Lu P 2009 *Thin Solid Films* **517** 5601
[37] Evans C C *et al* 2013 *Opt. Express* **21** 18582
[38] Hokr B H *et al* 2014 *Nat. Commun.* **5** 4356
[39] Scheffold F and Wiersma D 2013 *Nat. Photonics* **7** 934
[40] Maret G *et al* 2013 *Nat. Photonics* **7** 934–5
[41] van Albada M P and Lagendijk A 1985 *Phys. Rev. Lett.* **55** 2696
[42] Wolf P E and Maret G 1985 *Phys. Rev. Lett.* **55** 2696
[43] Gross P, Störzer M, Fiebig S, Clausen M, Maret G and Aegerter C M 2007 *Rev. Sci. Instrum.* **78** 033105
[44] Mirlin A D 2000 *Phys. Rep.* **326** 259
[45] Aegerter C M, Störzer M and Maret G 2006 *Europhys. Lett.* **75** 562

Research Article | Vol. 24, No. 20 | 3 Oct 2016 | OPTICS EXPRESS 23018
Optics EXPRESS

Structured illumination behind turbid media

A. MALAVALLI, M. ACKERMANN AND C. M. AEGERTER*

Physics Institute, University of Zurich, Winterthurerstrasse 190, 8057 Zurich, Switzerland
**aegerter@physik.uzh.ch*

Abstract: In turbid media, light gets multiply scattered to an extent that all the information of its propagation is scrambled over a characteristic distance called the transport mean free path. Controlling light propagation through such media is therefore challenging. By using a feedback signal, the input wavefront of light can be shaped such that light gets focused through or even inside a scattering medium [Vellekoop et al., Opt. Express *36*, 67 (2008)]. In this article, we show that such an interferometric focus can be transformed into an array of multiple focal spots with a desired structure. These focal spots can serve as a structured illumination source to image the interior of thick scattering tissues as in deconvolution imaging or in the optical micromanipulation of microscopic targets.

OCIS codes: (110.0113) Imaging through turbid media; (110.2945) Illumination design; (120.5060) Phase modulation

References and links

1. I. M. Vellekoop and A. P. Mosk,"Focusing coherent light through opaque strongly scattering media," Opt. Lett. **32**(16), 2309–2311 (2007).
2. I. M. Vellekoop, E. G. van Putten, A. Lagendijk, and A. P. Mosk,"Demixing light paths inside disordered metamaterials", Opt. Express **16**(1), 67–80 (2008).
3. C. Maurer, A. Jesacher, S. Fürhapter, S. Bernet and M. Ritsch-Marte, "Tailoring of arbitrary optical vector beams", New J. Phys. **9**(78), 1367–2630 (2007).
4. B. Chang, L.Chou, Y. Chang and S. Chiang,"Isotropic image in structured illumination microscopy patterned with a spatial light modulator," Opt. Express **17**(17), 14710–14721 (2009).
5. M.G.L. Gustafsson. "Surpassing the lateral resolution limit by a factor of two using structured illumination microscopy," J. Microsc. **198**, 82–87 (2000).
6. M. A. A. Neil, R. Juskaitis, and T. Wilson, "Method of obtaining optical sectioning by using structured light in a conventional microscope," Opt. Lett. **22**(24), 1905–1907 (1997).
7. S. W. Hell, & J. Wichmann, "Breaking the diffraction resolution limit by stimulated emission: stimulated-emission-depletion fluorescence microscopy," Opt. Lett. **19**, 780–782 (1994).
8. C. Kuang, S. Li, W. Liu, X. Hao, Z. Gu, Y. Wang, J. Ge, H. Li & X. Liu,"Breaking the Diffraction Barrier Using Fluorescence Emission Difference Microscopy," Sci. Rep. **3**, 1441 (2013).
9. T. Čižmár & K. Dholakia,"Shaping the light transmission through a multimode optical fibre: complex transformation analysis and applications in biophotonics," Opt. Expres, **19**(20), 18871–18884 (2011).
10. T. Čižmár, M. Mazilu and K. Dholakia,"In situ wavefront correction and its application to micromanipulation," Nat. Photon. **4**, 388–394 (2010).
11. S. Bianchia and R.Di Leonardo, "A multi-mode fiber probe for holographic micromanipulation and microscopy," Lab Chip **12**, 635–639 (2012).
12. S. Popoff, G. Lerosey, M. Fink, A. C. Boccara & S. Gigan,"Image transmission through an opaque material," Nat. Commun. **1** 81 (2010).
13. I.M.Vellekoop, "Feedback-based wavefront shaping," Opt. Express **23**(9), 12189–12206 (2015).
14. G. Ghielmetti and C.M. Aegerter,"Scattered light fluorescence microscopy in three dimensions," Opt. Express **20**(4), 3744–3752 (2012).
15. I. M. Vellekoop, A. Lagendijk, and A. P. Mosk,"Exploiting disorder for perfect focusing," Nat. Photon. **4**, 320–322 (2010).
16. T. Chaigne, J. Gateau, O. Katz, E. Bossy, and S. Gigan, "Light focusing and two-dimensional imaging through scattering media using the photoacoustic transmission matrix with an ultrasound array," Opt. Lett. **39**(9), 2664–2667 (2014).
17. I.M. Vellekoop & A.P. Mosk, "Phase control algorithms for focusing light through turbid media," Opt. Commun. **281**, 3071–3080 (2008).
18. G. Ghielmetti and C. M. Aegerter,"Direct imaging of fluorescent structures behind turbid layers," Opt. Express **22**(2), 1981–1989 (2014).
19. I.M.Vellekoop, Doctoral dissertation "Controlling the propagation of Light in Disordered Scattering Media".
20. D. Engström, A. Frank, J. Backsten, M. Goksör, and J. Bengtsson, "Grid-free 3D multiple spot generation with an efficient single-plane FFT-based algorithm," Opt. Express **17**(12), 9989–10000 (2009).

#272460 http://dx.doi.org/10.1364/OE.24.023018
Journal © 2016 Received 3 Aug 2016; revised 16 Sep 2016; accepted 18 Sep 2016; published 26 Sep 2016

Research Article | Vol. 24, No. 20 | 3 Oct 2016 | OPTICS EXPRESS 23019
Optics EXPRESS

21. J. W. Goodman, *Statistical Optics* (Wiley, 2000).
22. I. Freund, M. Rosenbluh, and S. Feng, "Memory Effects in Propagation of Optical Waves through Disordered Media," Phys. Rev. Lett. **61**, 2328–2331 (1988).

1. Introduction

Wavefront shaping is gaining much attention in the field of light microscopy to control the propagation of light in multiply scattering materials [1, 2]. It is one of the ways to counter the effects of scattering when imaging through materials of biological interest. Wavefront shaping has also been used to structure the illumination pattern in light microscopy. Interference between multiple orders of diffraction from a grating forms a sinusoidally varying light field. First order Bessel modes or other higher order vector modes can be generated using Spatial Light Modulators (SLM) [3, 4]. Such synthetic illumination patterns are known to enhance resolution in imaging beyond the diffraction limit [4–6] and Bessel or donut beams have been used for excitation-deexcitation beam configurations in STED microscopy [7, 8]. However, when transmitting these illumination patterns through turbid media, light gets multiply scattered and the pattern is quickly lost. Hence, structured illumination approach is able to work with optically thin or transparent sections, which is often limited to superficial layers of samples.

Using SLMs, the wavefront of incoming light can be modulated in phase and amplitude in order to control the scattered light field. In adaptive optics, feedback based algorithms are used to correct for abberations from optical setups and to map the transmission matrix of abberated systems such as optical fibers [9]. This approach has been widely used for trapping and micromanipulation of particles [10, 11]. But mapping such a transmission matrix can be time consuming when many configurations of output fields are to be realised [12]. It is however now possible to focus light through a multiply scattering medium using feedback based algorithms [13] and scan this focus in 3D [14]. In the present article we extend this technique to obtain multiple focal spots behind a multiply scattering medium.

The working principle of our technique as demonstrated by Fig. 1 is that a diffraction limited focus can be generated using a feedback based technique using an iterative algorithm [15–17] and such a focus can then be transformed into a user defined configuration of multiple focal spots. After the optimization process, the scattering medium acts as a turbid lens that focuses the spatially modulated optimum wavefront. By adding a desired phase mask to this wavefront, multiple focal spots can be generated by virtue of convolution theorem. As this technique does not depend on the type of feedback mechanism used to create the initial focus it can be beneficial especially when a direct access to the focal plane is not available [18]. The theory concerning this technique is decribed in section 2. The computation of such phase masks, also called Computer Generated Holograms (CGHs) is described in section 3 followed by the experimental results in section 4. Multiple foci can also be generated without the use of these CGHs- by directly

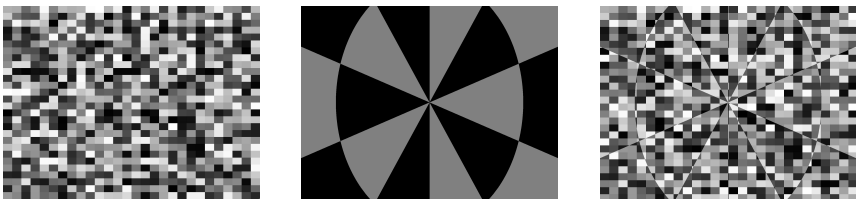

a) Optimum Wavefront b) Computed CGH c)Final SLM phase

Fig. 1. To the optimum wavefront a) leading to a focus behind the turbid medium, when a CGH such as b) is added, the resulting phase would look like c).

Research Article | Vol. 24, No. 20 | 3 Oct 2016 | OPTICS EXPRESS 23020
Optics EXPRESS

optimizing on multiple targets as previously described in [19]. In section 5 of this article we further describe and compare these methods.

2. Theoretical background

As shown in the experimental setup Fig. 2, the SLM plane and sample form conjugate planes such that an image of the SLM screen is formed on the sample. When a phase modulation scheme is used [17], the computer algorithm iteratively alters the phase of the pixels on the SLM to form an interferometric focus at the focal plane.

After focusing, the combination of SLM and the scattering medium acts as a lens. If the beam coming into the SLM is tilted, the focal spot moves. This tilting effect can also be implemented by just adding a suitable phase to the modulated wavefront at the SLM. The same works if we add a phase pattern that, like a grating, results in multiple beams. To this combination resulting in a lens, by adding the phase pattern of a grating, we bring the far field of the grating onto the focal plane, resulting in multiple spots.

If $\mathcal{E}_i = \mathcal{E}_0 \exp^{i\phi}$ is the electric field of the wavefront with phase ϕ modulated by the SLM to obtain a focus, the field at the focal plane on the CCD is given by [14],

$$\mathcal{E}_f = \iint_S \mathcal{E}_i \, t_{i\,s} \, g(r_f - r_s) \, d^2 r_s \tag{1}$$

integrated over the scattering plane of the sample. Here, $t_{i\,s}$ is the coefficient of the optical setup for transmitting light from each segment of the SLM to the output plane of the sample and the light propagaion from this plane to the CCD is described by the free space Green function $g(r_f - r_s)$ [15]. It has been shown experimentally [15] that the shape of this interferometric focus is same as the speckle correlation function [21].

Transformation of this focus into multiple foci can be understood using the convolution theorem. It states that,

if $\mathcal{F}\{\mathcal{E}_f(y,z)\} = E(k_y,k_z)$ and $\mathcal{F}\{f(y,z)\} = F(k_y,k_z)$, then

$$\begin{aligned} \mathcal{F}\{\mathcal{E}_f * f\} &= \mathcal{F}\{\int_{-\infty}^{+\infty}\!\!\iint \mathcal{E}_f(y,z)\, f(Y-y, Z-z)\, dy\, dz\} \\ &= \mathcal{F}\{\mathcal{E}_f(y,z)\}\ \mathcal{F}\{f(y,z)\} \\ &= E(k_y,k_z)\ F(k_y,k_z) \end{aligned} \tag{2}$$

i.e if $\mathcal{E}_f(y,z)$ represents the field distribution of the interferometric focus and $f(y,z)$ represents Dirac delta functions with their peaks located where the focal spots are desired,

$$f(y,z) = \sum_i \exp^{i\,\phi_i}\, \delta(y - y_i)\delta(z - z_i) \tag{3}$$

the convolution between the two leads to a multiple focal pattern in the image plane. Furthermore, the phase that needs to be added on the SLM plane in order to obtain this multiple focal pattern can be extracted by noticing that,

$$E(k_y,k_z) = \mathcal{E}_i \, t_{i\,s} \, g(r_f - r_s) \tag{4}$$

and as $t_{i\,s}$ and $g(r_f - r_s)$ are unaffected, $\mathcal{F}\{\mathcal{E}_f * f\} = \mathcal{E}_i \, F(k_y,k_z)$

Since we make use of phase only modulation scheme, the intensity contribution to the focal plane from different regions of sample is not the same, leading to fluctuations in intensity when focal spots move. However this could be rectified if both phase and amplitude modulation scheme were used in the optimization process.

Research Article Vol. 24, No. 20 | 3 Oct 2016 | OPTICS EXPRESS 23021
Optics EXPRESS

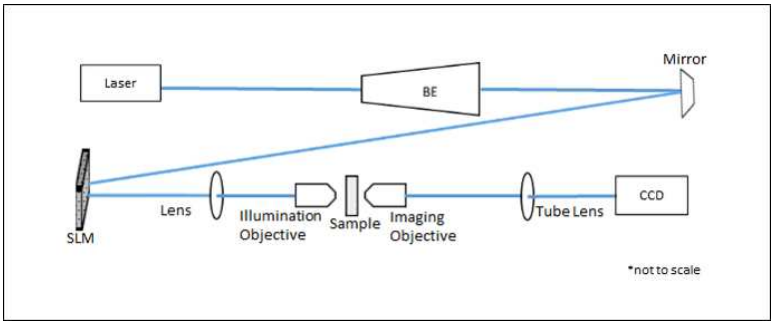

Fig. 2. Experimental Setup.

3. Experimental setup

The experimental setup is as shown in Fig. 2. Light from a Cyan laser (Newport Spectra-Physics) at 488nm is expanded with a beam expander setup (BE) to fill the screen of the SLM (HOLOEYE HEO 1080P). The SLM plane is imaged onto the sample using a lens and a 40x illumination objective, such that the SLM and the sample make a pair of conjugate planes. The back surface of the sample is imaged with a 50X objective and a CCD. We made use of opaque samples of microscope slide coated with TiO_2 with thicknesses ranging from 3-15μm. Light transmitted through such a sample is multiply scattered and forms a speckle pattern on the CCD. Using stepwise sequential algorithm [17], the SLM modulates the phase of the input wavefront while monitoring the intensity enhancement at a small target region (typically about the size of a single speckle) on the CCD. The input intensity before optimisation is kept low enough to avoid saturation on the CCD. After iterating over the whole SLM, an interferometric focus is formed at the target. Once this initial focus is formed, the CGHs can be loaded onto the optimized wavefront on the SLM plane and the resulting multiple foci can be visualised on the CCD. Using linear or parabolic phase gradients at the SLM, the focal spots can be translated on the CCD. For the experiments involving movement of the foci, a grit polished diffuser glass was used as a sample.

4. Phase mask generation

The generation of CGHs is a crucial step of these experiments. Depending on the complexity of the desired configuration of focal spots, one can choose from different methods to generate the CGH [3, 20]. As the Fourier transformation operation is reversible [22], the phase modulation by $F(k_y, k_z)$, as described in Eq. (2-3), in the scattering plane of the sample should lead to a 2D grid of Dirac delta functions in the image plane, as described in the previous section. To get a planar grid of equally spaced focal spots, we generated grayscale images such as shown in Fig. 3(a). The phase modulation is achieved using 8-bit bitmap images, whose grayscale values between 0-255 correspond to a phase modulation between 0-2π. These images constitute a combination of binary gratings of multiple periods extending in 2 dimensions. Furthermore, we computed the Fourier transform of the phase values of these images to verify that the intensity peaks in the image plane appear at the spatial frequencies defined by the periodicity of the gratings. These peaks in the Fourier transform correspond to the positions of the focal spots that would be formed on the image plane Fig. 3(b). The grayscale values and/or the period of the gratings in the images were altered to change the configuration and position of the spots in the Fourier plane. The smaller the period is, the farther away the spots move in Fourier space Fig. 4. In this manner

Research Article Vol. 24, No. 20 | 3 Oct 2016 | OPTICS EXPRESS 23022
Optics EXPRESS

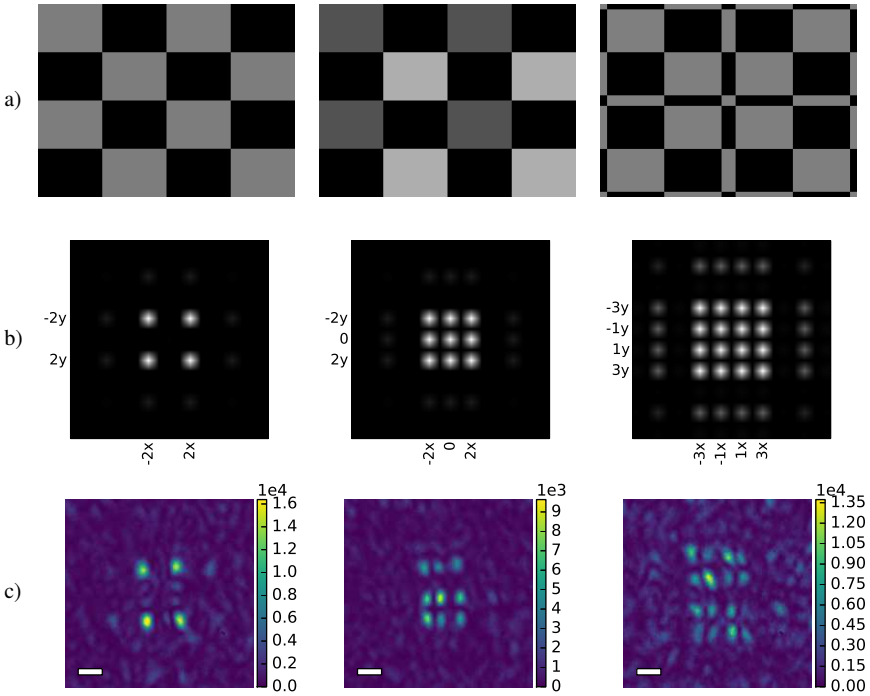

Fig. 3. a) Phase masks loaded onto the SLM for obtaining multiple focal spots through a layer of TiO_2 b) computed Fourier Transforms of (a). c) resulting pattern on the CCD for respective images in (a). Scalebar corresponds to 5μm.

we are able to generate different configurations of focal spots with rectangular as well as radial symmetry Fig. 5.

We have also used two algorithms that try to generate optimal phase masks. These algorithms simulate an SLM plane where the field is modulated such that when Fourier Transformed, the intensity is enhanced at certain predefined locations. The first approach is a genetic algorithm that optimizes the phase of the rectangular regions of the SLM. It works with a population of phasemasks, where each phasemask has phase values for each rectangular region. Through mutations and inheritance, the population evolves towards an optimal solution. For the second approach, we set the phase mask to $\phi(\mathrm{y},\mathrm{z}) = \arg(\mathrm{ifft}(\mathrm{F}))$ where F is zero everywhere except at the target spots and ifft corresponds to inverse Fourier transform operation. If we calculate F from $\phi(y, z)$ as described in section 2, then the central spots will have a much lower intensity than those at the edges Fig. 6. This is caused by taking the argument of the ifft which drops all intensity information of our spectrum. We can regain uniformity by optimizing the phase of the spots in F using stochastic optimization. Both algorithms result in multiple focal spots being formed on the image plane as shown in Fig. 6.

Research Article Vol. 24, No. 20 | 3 Oct 2016 | OPTICS EXPRESS 23023
Optics EXPRESS

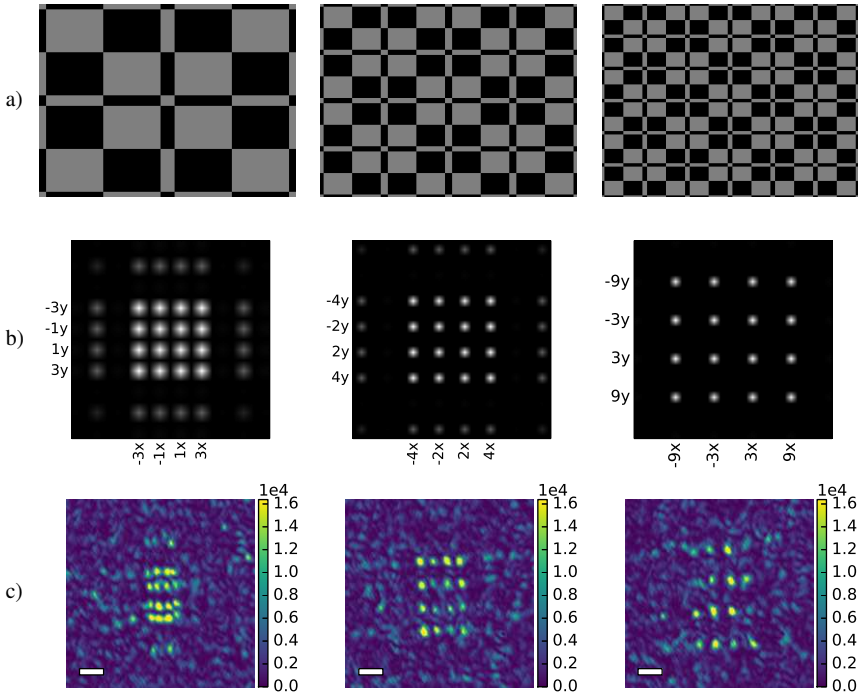

Fig. 4. Moving the focal spots in k-space: a) the SLM masks. b) computed Fourier Transforms c) resulting CCD images for diffuser glass used as sample. Scalebar corresponds to 5μm.

5. Results and discussion

The CGHs such as those described in the previous section can be generated independently of the real time experiments beforehand. In the real time experiments, once the interferometric focus is obtained, these CGHs can be added to the SLM and the resulting multiple foci can be visualised on the CCD. We demonstrate some sample configuration of focal spots which are formed by the respective CGHs as shown in Fig. 3 through 7.

Thus created multiple focal spots can be in turn used to illuminate–for example–flourescent targets in biological samples and image them. The ability to realise any configuration of focal spots can make it easier to acquire sample information from multiple locations parallely. It could also be possible to optically trap and micro manipulate targets hidden within turbid media, which would otherwise be inaccessible. The simplicity of the approach of Fourier transformation makes it easier to translate and rotate the focal spots. By adding a linear phase shift to the phase masks in the SLM plane, we are able to translate the spots. Similarly, a parabolic phase shift would move the spots in the forward direction out of the plane [4]. Also, when the coordinate axes of the images are rotated, the focal spots follow the drift and rotate in the image plane. (see Visualization 1). This freedom of moving the focal spots can accelerate image acquision process compared to raster scanning a single focal spot.

Translating the foci however depends on the range of memory effect [22], defined as the extent to which the transmitted light preserves the information about the input phase and amplitude

Research Article Vol. 24, No. 20 | 3 Oct 2016 | OPTICS EXPRESS 23024
Optics EXPRESS

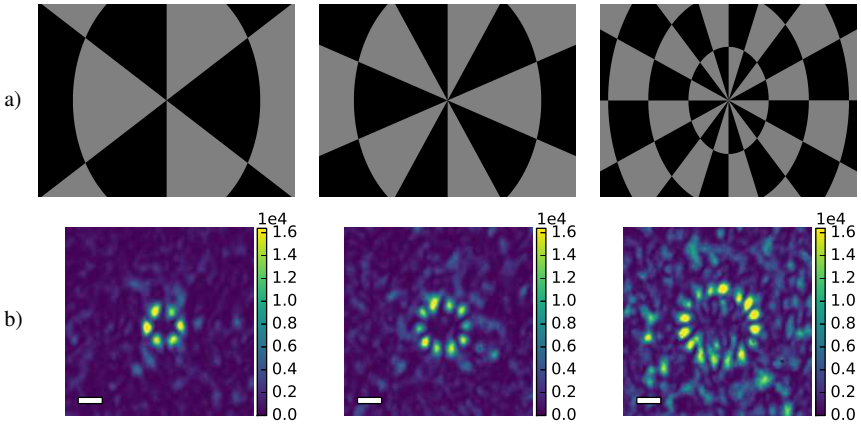

Fig. 5. a) Phase masks loaded onto the SLM to obtain focal spots with radial symmetry. b) Resulting patterns on the CCD respectively. Scalebar corresponds to 5μm.

variation. The memory effect range falls as the inverse of the thickness of the medium. For a thick 15μm layer of TiO_2, it is about 3μm and the pattern of multiple foci is lost when translated further than this range. This is also the case when the distance between the focal spots is more than the range of memory effect. Hence such experiments can only be perfomed on optically thin samples. Figure 4 shows the possibility of movement of focal spots through a diffuser for which memory effect range is theoretically unlimited [22]].

Although, the size and shape of the initial focus is retained in the multiple foci, their intensities are lower than the initial focus. Due to this, the input intensity was increased to make the focal spots visible, and thus rescaling the range of transmitted intensity on the CCD. This reduction is attributed to the intensity enhancement of initial focus with respect to the background- that gets redistributed among the multiple foci. Hence there exists a tradeoff between the contrast and the number of foci, which in turn are limited by the achievable intensity enhancement. Multiply scattering TiO_2 samples also cause this contrast to be lost quickly compared to less scattering diffuser glass. Fig. 7 demonstrates the limiting case for our signal to background ratio; where 36 focal spots are created through a diffuser, which was not possible with TiO_2 samples. Beyond this, the focal spots were indistinguishable from the background speckles in any sample.

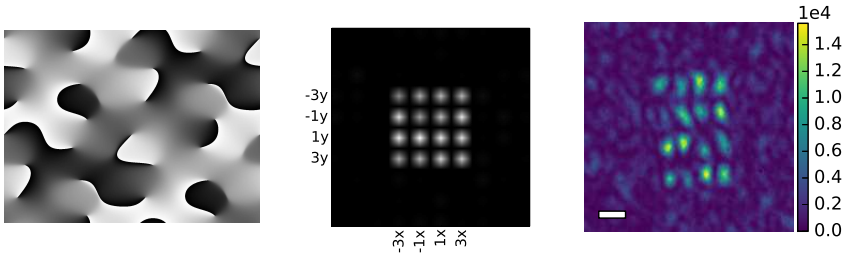

Fig. 6. CGH generated using Stochastic algorithm, computed Fourier Transform and resulting focal spots on CCD plane. Scalebar corresponds to 5μm.

Research Article Vol. 24, No. 20 | 3 Oct 2016 | OPTICS EXPRESS 23025
Optics EXPRESS

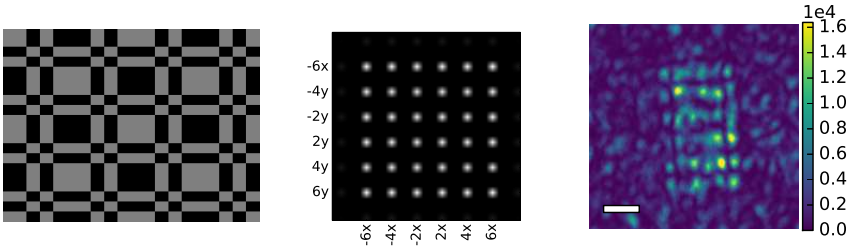

Fig. 7. Limiting case of number of foci demonstrated for diffuser glass: SLM mask,computed Fourier Transform and resulting CCD image. Scalebar corresponds to 10μm.

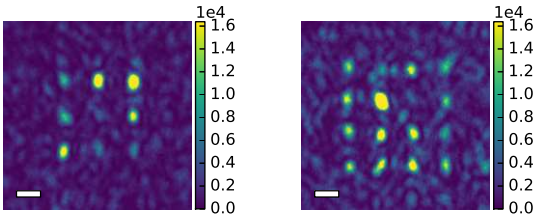

Fig. 8. Direct optimization on multiple configurations of a target. Scalebar corresponds to 5μm.

As a comparitive study to that noted previously in [19] we also perfomed the experiments by directly optimizing on multiple targets in the focal plane. We defined multiple configurations of a target Fig. 8 at the back of the sample and saw that the algorithm manages to optimize on all the targets well as long as the number of targets is small. For a large number of targets, the intensity distribution grows to be more non-uniform. This may not be desirable for applications where intensity destributions play a role. In addition, this technique by construction requires optical access to multiple locations of the focal plane and would not work well when such an access is not available.

6. Conclusion

In this article we have described a technique to obtain multiple focal spots behind a turbid medium. Computer generated phase masks can be used to transform an interferometric focus obtained behind a turbid medium into a desired configuration of multiple focal spots. With the ability of further manipulating these phase masks, the focal spots can be freely translated and rotated. This technique can find potential applications in the field of bioimaging such as structured illumination microscopy behind turbid media or optical control and micromanipulation of particles hidden in turbid environments.

Funding

Swiss National Science Foundation (Award Number 501100001711).

Research Article | Vol. 24, No. 20 | 3 Oct 2016 | OPTICS EXPRESS 23026
Optics EXPRESS

Acknowledgments

We would like to thank Dr. Jale Schneider for her contributions to the phase mask generation techniques using Genetic Algorithm.